Integration of mm-Wave Antenna Systems in 5G Mobile Terminals

Rodriguez Cano, Rocio

Publication date:
2020

Document Version
Publisher's PDF, also known as Version of record

INTEGRATION OF MM-WAVE ANTENNA SYSTEMS IN 5G MOBILE TERMINALS

BY
ROCÍO RODRÍGUEZ CANO

DISSERTATION SUBMITTED 2020

AALBORG UNIVERSITY
DENMARK

Aalborg University

Department of Electronic Systems,
Antennas, Propagation and Millimeter-Wave Systems Section

Ph.D. Thesis

Integration of mm-Wave Antenna Systems in 5G Mobile Terminals

Rocío Rodríguez Cano

Aalborg, 2020

AALBORG UNIVERSITY
DENMARK

Dissertation submitted: October 30, 2020

PhD supervisor: Prof. Gert Frølund Pedersen
Department of Electronic Systems
Aalborg University

Ph.D. Co-Supervisor: Assoc. Prof. Shuai Zhang
Department of Electronic Systems
Aalborg University

PhD committee: Associate Professor Carles Navarro Manchón (chair)
Aalborg University

Professor Luc Martens
Ghent University

Senior Lecturer Tim Brown
University of Surrey

PhD Series: Technical Faculty of IT and Design, Aalborg University

Department: Department of Electronic Systems

ISSN (online): 2246-1302
ISBN (online): 978-87-7210-835-3

Published by:
Aalborg University Press
Kroghstræde 3
DK – 9220 Aalborg Ø
Phone: +45 99407140
aauf@forlag.aau.dk
forlag.aau.dk

Printed in Denmark by Rosendahls, 2020

Contents

Abstract

The fifth generation of mobile communication (5G) has led to a redesign of the RF front-end, due to the inclusion of the new mm-wave bands in wireless communications. The use of smaller wavelengths makes communications more sensitive to objects and environmental factors. The higher propagation losses are compensated by having antenna systems with larger gains, but the effect from other components when the antenna is integrated into the phone, requires further consideration.

A component that has a strong impact on the radiation pattern of the mm-wave antennas is the display glass. A transparent structure printed on top of the glass is proposed to reduce the surface waves effects. The results show that the ripples in the radiation pattern are considerably reduced, which increments the maximum gain.

Different methods to cope with the obstruction provoked by the metallic phone chassis to the endfire radiation of mm-wave antennas are also discussed in this thesis. The proposed methods are for a metallic frame since it is the most adverse material for the antenna radiation. It has been shown that the detrimental effect mainly occurs for antennas with horizontal polarization. The three different solutions proposed have been tested with particular mm-wave antenna arrays. However, these methods are not restricted to a certain kind of antenna topology, but they can be applied to any antenna design and phone form factor.

Resumé

Den femte generation af mobilnetværket (5G) har gjort et redesign af RF frontenden nødvendig, på grund af introduktionen af de nye mm-frekvenser. Brugen af signaler med kortere bølgelængder gør kommunikationen mere sårbar over for genstande placeret i umiddelbar nærhed af antennen. Det resulterende og større radioudbredelsestab kompenseres for ved at have antennesystemer med højere gain. Men når antennen er integreret i telefonen påvirkes den af de øvrige komponenter, hvilket kræver yderligere overvejelser.

En komponent, der har en stærk indflydelse på udstrålingsdiagrammet for mm-bølge antennerne, er skærmglasset. En transparent struktur, der er trykt på toppen af glasset, foreslås for at reducere overfladebølgens effekter. Resultaterne viser, at variationerne i udstrålingsdiagrammet er betydeligt reduceret, hvilket øger det maksimale gain.

Forskellige metoder er også præsenteret i denne afhandling til at overkomme de udfordringer, der kommer som følge af metalschassiset i telefonen, og dettes påvirkning af mm-bølgeantenners udstråling. Den metalliske ramme har størst negativ indflydelse på udstrålingen, og forskellige metoder til håndtering af dette foreslås. Det er blevet vist, at den største negative indflydelse på udstrålingen kommer for antenner med vandret polarisering. I afhandlingen præsenteres tre forskellige løsninger, der alle er testet i forbindelse med specifikke mm-bølge-antennearray designs. De præsenterede metoder er dog ikke begrænset til en bestemt form for antennetopologi, men de kan anvendes til ethvert antennedesign og vilkårlige telefonformfaktorer.

Preface

To begin with, I would like to express my sincere gratitude to Prof. Gert Pedersen, who gave me the opportunity of pursuing my research. My appreciation also extends to Associate Prof. Shuai Zhang, whose mentoring and early insights launched this dissertation. To Dr. Kun Zhao, I am extremely grateful for his guidance and feedback throughout my Ph.D. The writing of this dissertation would not have been possible without his help and advice.

I would also like to thank Prof. Richard W. Ziolkowski, who welcomed me to the University of Technology Sydney (UTS). His enthusiasm kept me constantly engaged with my research, and his insightful remarks helped improve the quality of my publications.

This work is a part of the Reconfigurable Arrays for Next Generation Efficiency (RANGE) project, funded by the Innovation Fund Denmark in collaboration with AAC, WiSpry and Sony Mobile. I would like to mention Dr. Arthur Morris, Dr. Zhinong Ying and Mr. Thomas Bolin, whose suggestions have inspired further improvements and ideas.

My sincere gratitude to our laboratory engineers: Ben Krøyer, Peter Jensen, Jesper Meyer, Kim Olesen and Kristian Bank, for their assistance in the fabrication and measurement of the antenna prototypes. I would also like to express my appreciation to Jan Mikkelsen for his guidance.

I have to thank all my colleagues of the Antennas Propagation and Millimetre-Wave Systems (APMS) section, for all the advice, help and fun through the last three years.

And last but not least, many thanks to my family and my partner for all the comfort and support during hard times, and for showing me that hard work always pays off.

Rocío Rodríguez Cano

Aalborg University, October, 2020

Thesis Details

Thesis Title:	Integration of mm-Wave Antenna Systems in 5G Mobile Terminals
Ph.D. Candidate:	Rocío Rodríguez Cano
Supervisors:	Prof. Gert Frølund Pedersen - Aalborg University Assoc. Prof. Shuai Zhang - Aalborg University

This thesis is submitted as part of the requirements for the degree of Doctor of Philosophy (Ph.D.) from Aalborg University, Denmark. The thesis is compiled as a collection of papers, resulting in a short introduction and the main part of the thesis being scientific papers published in, or submitted to, peer-reviewed journals and conferences. The work presented in the thesis is the result of three years of research, in the period November 2017 – October 2020, as a Ph.D. fellow in the Section of Antennas, Propagation and Millimetre-Wave Systems, Department of Electronic Systems, Aalborg University.

The Ph.D. stipend (nr. 8-17073) has been funded as a part of the RANGE project. The Innovation Fund Denmark, together with Aalborg University and industry partners: AAC, Wispry, and Sony, have financed this project.

The main body of this thesis consists of the following papers:

A. R. Rodríguez-Cano, S. Zhang and G. F. Pedersen, "Transparent mm-Wave Array on a Glass Substrate with Surface Wave Reduction", *2020 14th European Conference on Antennas and Propagation (EuCAP)*, Copenhagen, Denmark, 2020, pp. 1-4, doi: 10.23919/EuCAP48036.2020.9136095.

B. R. Rodríguez-Cano, S. Zhang, K. Zhao and G. F. Pedersen, "Reduction of Main Beam-Blockage in an Integrated 5G Array With a Metal-Frame Antenna", *IEEE Transactions on Antennas and Propagation*, vol. 67, no. 5, pp. 3161-3170, May 2019, doi: 10.1109/TAP.2019.2900407.

C. R. Rodríguez-Cano, S. Zhang, K. Zhao and G. F. Pedersen, "mm-Wave

Beam-Steerable Endfire Array Embedded in a Slotted Metal-Frame LTE Antenna", *IEEE Transactions on Antennas and Propagation*, vol. 68, no. 5, pp. 3685-3694, May 2020, doi: 10.1109/TAP.2020.2963915.

D. R. Rodríguez-Cano, K. Zhao, S. Zhang and G. F. Pedersen, "Handset Frame Blockage Reduction of 5G mm-Wave Phased Arrays Using Hard Surface Inspired Structure", *IEEE Transactions on Vehicular Technology*, vol. 69, no. 8, pp. 8132-8139, Aug. 2020, doi: 10.1109/TVT.2020.2996360.

According to the Ministerial Order no. 1039 of August 27, 2013, regarding the Ph.D. Degree § 12, article 4, statements from each co-author about the Ph.D. students contribution to the above-listed papers have been provided to the Ph.D. school for approval prior to the submission of this thesis. These co-author statements have also been presented to the Ph.D. committee and included as a part of their assessment.

In addition to the listed papers as the main content of this thesis, the following papers were also either authored or co-authored during the Ph.D. studies. As these papers are not a part of the main body of this thesis they have not been included in the print. The reader is therefore kindly referred to the respective publishing channels as listed hereafter.

Journals:

1. R. Rodríguez-Cano, R.W. Ziolkowski, "Flexible, Single-Layered, Unidirectional, Broadside-Radiating Planar Antenna for 5G IoT Applications", *IEEE Transactions on Antennas and Propagation*, Submitted, 2020.

Conference papers:

1. R. Rodríguez-Cano, S. Zhang and G. F. Pedersen, "Beam-steerable multiband mm-wave bow-tie antenna array for mobile terminals", *12th European Conference on Antennas and Propagation (EuCAP 2018)*, London, 2018, pp. 1-4, doi: 10.1049/cp.2018.0418.

2. R. Rodríguez-Cano, S. Zhang and G. F. Pedersen, "Radiation Pattern Reconfigurable mm-Wave Bow-Tie Array Integrated with PIFA Antenna", *2019 IEEE 90th Vehicular Technology Conference (VTC2019-Fall)*, Honolulu, HI, USA, 2019, pp. 1-3, doi: 10.1109/VTCFall.2019.8891496.

3. R. Rodríguez-Cano, S. Zhang, K. Zhao and G. F. Pedersen, "User Body Interaction of 5G Switchable Antenna System for Mobile Terminals at 28 GHz", *2019 13th European Conference on Antennas and Propagation (EuCAP)*, Krakow, Poland, 2019, pp. 1-4.

4. R. Rodríguez-Cano, K. Zhao, S. Zhang and G. F. Pedersen, "Wideband Reduction of the Metal-Frame Blockage to mm-Wave Antennas", *2021 15th European Conference on Antennas and Propagation (EuCAP)*, Submitted, 2020.

Patents:

1. R. Rodríguez-Cano, S. Zhang and G. F. Pedersen, "Integrated end-fire mm-wave antenna array with low frequency metal-framed antenna", US Patent App. 16/557, 543, 2020.
2. R. Rodríguez-Cano, S. Zhang and G. F. Pedersen, "Corner antenna array devices, systems, and methods", US Patent App. 16/240, 260, 2019.

In the next section, the main contributions of the papers included in the thesis in Part II are presented, together with brief summaries of the motivation, work, and findings.

Contributions

The main objective of this Ph.D. project is to provide solutions for the problems arising when the new mm-wave antenna designs are integrated into the phone chassis. One problem emerging from the phone integration is the propagation of surface waves on dielectric substrates. The surface waves that propagate in glass covers can be detrimental to the radiation pattern of mm-wave antennas, since they reduce the realized gain and cause ripples. Paper A deals with the reduction of surface waves generated on the glass display by the mm-wave antennas.

The metallic frame can also be detrimental to the radiation pattern of mm-wave antennas, which are commonly located at the edges of the handset. Three different methods to reduce the metal-frame blockage have been proposed in Papers B, C and D. Even though specific mm-wave array designs have been employed to prove the concept, the proposed solutions can be applied to other arrays, frame widths and phone form factors.

Paper A

Transparent mm-Wave Array on a Glass Substrate with Surface Wave Reduction

R. Rodríguez-Cano, S. Zhang and G. F. Pedersen

Published in *2020 14th European Conference on Antennas and Propagation (EuCAP)*, Copenhagen, Denmark, 2020, pp. 1-4,
doi: 10.23919/EuCAP48036.2020.9136095.

Motivation

The phone display is made of different layers, glass being one of them. The glass allows the propagation of surface waves, which can be detrimental to the radiation pattern of the mm-wave antennas, generating ripples and sidelobes, which decrease the gain in the desired direction. The target of this contribution was to reduce the surface waves with a parasitic structure printed on the glass.

Paper content

Several rows of transparent strips were placed in front of the mm-wave array, in order to reduce the surface waves. Both the antenna and the strips were transparent, and were placed on top of the glass. They were made by diamond grid cells that provide 86 % transparency. The simulation results presented in Fig. 1 compare the 3D realized gain patterns of the mm-wave array with and without the rows of strips. The corresponding surface currents for both cases are also shown in the paper.

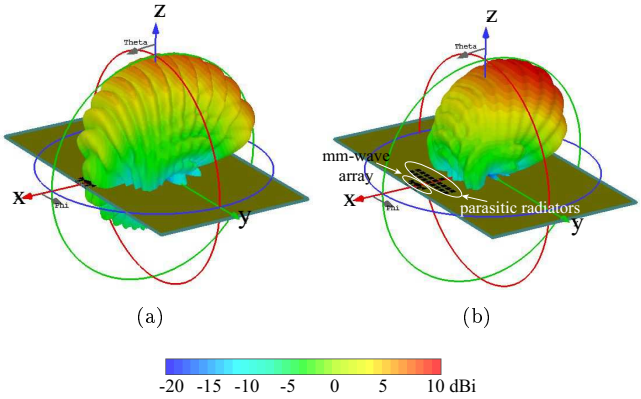

Fig. 1: 3D realized gain radiation pattern. (a) Antenna array without strips. (b) Antenna array with patch structure to reduce the surface waves.

Main results

The placement of the strip rows yields a reduction of the ripples in the realized gain patterns and of the back-lobe level. The radiation pattern becomes smoother and the maximum gain is increased by 3 dBi. The array achieves a

peak gain value higher than 8 dBi in the operational frequency band with an efficiency greater than 70 %. In contrast, the efficiency of the solutions reported in the literature is below 53 %.

Paper B

Reduction of Main Beam-Blockage in an Integrated 5G Array With a Metal-Frame Antenna

R. Rodríguez-Cano, S. Zhang, K. Zhao and G. F. Pedersen.

Published in *IEEE Transactions on Antennas and Propagation*, vol. 67, no. 5, pp. 3161-3170, May 2019, doi: 10.1109/TAP.2019.2900407.

Motivation

Planar antenna arrays with endfire radiation are common proposals to cover the new mm-wave bands. These arrays are located at the edges of the handset, to avoid extra losses due to the influence of other components. However, the majority of the designs, do not take into account the effect of the phone metallic frame on the radiation pattern of the antenna. Just a 3-mm width piece of metal in front of the antenna, can cause full or partial blockage of the main beam. The aim of this paper was to provide some parasitic structures to be included in the frame design and reduce the blockage effects of the metallic frame to endfire antennas.

Paper content

The paper proposed two tilted parasitic layers to be placed at both sides of the frame, to re-direct the energy radiated from a vivaldi array into the endfire direction, as shown in Fig. 2(c). The metallic frame was also employed as a sub-7 GHz antenna. The measured and simulated results, of both antennas, were presented and discussed.

Main results

The impact of the metallic frame occurs mainly in horizontally-polarized endfire antennas, while the radiation patterns of the antennas with vertical polarization are barely affected. The operating principle consists of coupling the energy yielded by the driven mm-wave antenna, from the metallic frame to the parasitic layers. This method allows reducing the energy reflected back to the antenna, to a minimum. The design parameters that affect the gain of the antenna array, the most, are the length and gap of the strips that form the parasitic layers and the antenna-frame distance. The measured results confirm that the parasitic layers can successfully re-radiate the energy to the endfire direction. The gain

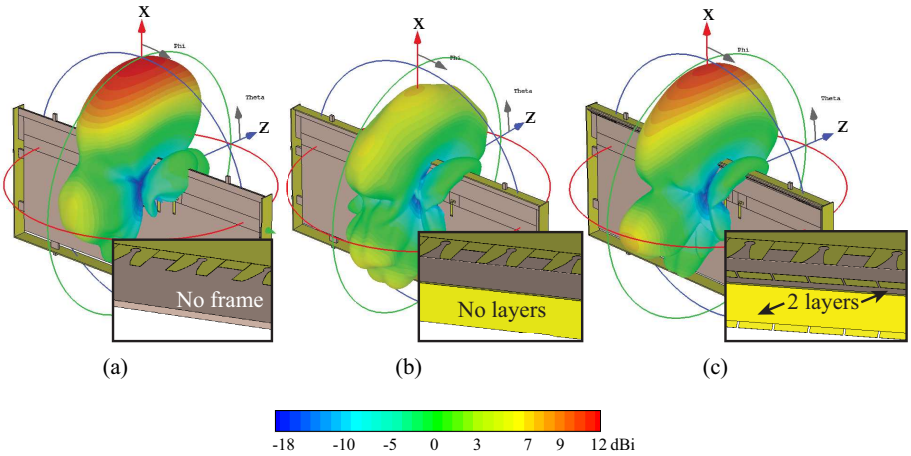

Fig. 2: 3D realized gain radiation patterns at 24.25 GHz. (a) No frame. (b) Normal frame with no layers. (c) Proposed design with two layers.

in the endfire direction of the proposed solution is around 2 dBi higher than the antenna integrated with a normal frame, and approximately 1 dBi below the free space solution.

Paper C

mm-Wave Beam-Steerable Endfire Array Embedded in a Slotted Metal-Frame LTE Antenna

R. Rodríguez-Cano, S. Zhang, K. Zhao and G. F. Pedersen

Published in *IEEE Transactions on Antennas and Propagation*, vol. 68, no. 5, pp. 3685-3694, May 2020, doi: 10.1109/TAP.2020.2963915.

Motivation

The desired narrow clearances for mm-wave antennas in mobile phones have motivated the co-design of mm-wave and sub-7 GHz antennas. Since the frame antenna is one of the most common low-frequency (sub-7 GHz) antennas, the goal of this paper is to make small cuts in the metallic frame to allow the radiation emitted by endfire mm-wave antennas not to be disturbed by the frame.

Paper content

The analysis of the surface currents generated on the frame by the mm-wave array, helps determine the optimal orientation of the slots to maximize the gain.

Several slot shapes were investigated as possible cuts off the frame, in order to obtain the maximum gain in the operating frequency band. The number of slots, the separation between them and the antenna-frame distance were also assessed to achieve the best performance. Together with the mm-wave antenna, a low-frequency metallic frame antenna was designed and evaluated. The realized gain radiation patterns of the proposed solution are presented in Fig. 3. These patterns point to the same direction as those of the original mm-wave array in free space.

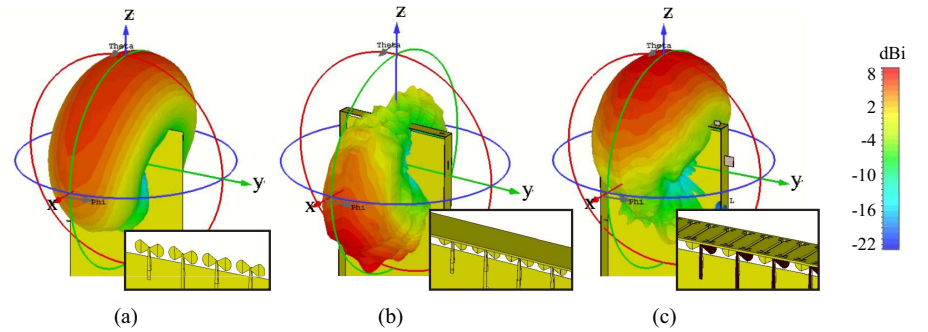

Fig. 3: 3D realized gain radiation patterns at 26 GHz. (a) No frame. (b) Normal frame. (c) Proposed design with the slotted frame.

Main results

The slotted-frame design not only allows the radiation in the desired endfire direction, but also enhances the realized gain of the mm-wave antenna array by 2 dBi in comparison to the free space array. This method also allows reducing the size of the antenna-frame distance to 0.5 mm, compared to the solution proposed in Paper B (7 mm). The number of slots etched must be slightly larger than the array aperture, to ensure the beam-steering behavior. The separation between the slots that provides the best impedance matching and higher gain corresponds to half the separation distance between the antenna elements.

Paper D

Handset Frame Blockage Reduction of 5G mm-Wave Phased Arrays Using Hard Surface Inspired Structure

R. Rodríguez-Cano, K. Zhao, S. Zhang and G. F. Pedersen

Published in *IEEE Transactions on Vehicular Technology*, vol. 69, no. 8, pp. 8132-8139, Aug. 2020, doi: 10.1109/TVT.2020.2996360.

Motivation

Periodic structures are used to control the propagation characteristics of electromagnetic fields. Particularly, hard surfaces allow the wave propagation along the surface. A hard surface can be obtained with corrugations etched longitudinally on a metallic surface in the direction of propagation, filled with a dielectric material. The aim of this paper was to allow the beams radiated by the mm-wave endfire antennas to propagate freely away from the front of the handset metallic frame by etching some appropriately designed corrugations on its edges, which reduce the radiation reflected back to the antennas.

Paper content

To verify the behavior of the metallic frame with corrugations as a hard surface, a 10 mm-thick corrugated metal was placed in front of the mm-wave antenna, confirming the expected endfire radiation. Since a normal frame is not as thick as 10 mm, 0.6 mm was chosen in this paper, and therefore, the proposed structure is not considered a hard surface, but inspired by it. The effect of the corrugated frame was studied alone when a planar wave was impinging on it. Several parametric studies were carried out to determine the best design of the grooves. A prototype was built and measured. The realized gain radiation patterns of the mm-wave array in free space, with a normal frame and with the developed solution, are presented in Fig. 4. The main beam of the proposed solution points to the desired direction.

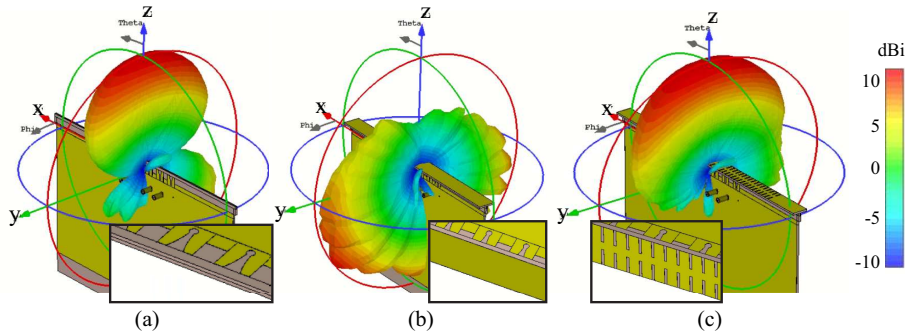

Fig. 4: 3D realized gain radiation patterns at 26 GHz. (a) No frame. (b) Normal frame. (c) Proposed design with hard surface inspired corrugations.

Main results

This paper proposed another method of reducing the metallic frame blockage of the fields radiated by mm-wave endfire antennas. The frame was composed of a metallic layer and a dielectric substrate. Increasing the substrate permittivity

can reduce the size of the grooves etched on the metal, making the structure more robust and less noticeable to the user. The length of the grooves is the most critical parameter. The mm-wave array is placed 1 mm away from the frame in the final prototype. The measured results confirmed the simulations. The gain of the array in the endfire direction of the proposed solution is very similar to the free space scenario, and around 9 dBi higher than the array in the presence of a normal frame.

Part I

Introductory Chapters

Chapter 1. Introduction

Wireless communication has become a key part of our daily lives. The continuous demand for higher capacity, lower latency and more robustness, has prompted the evolution of five generations of cellular communication systems, so far. Each one of them was enabled by major technological advances that resulted in significant performance improvement and new use cases. The first generation of mobile communication (1G) was born in the late 1970's, which consisted of a basic analog system design for voice communication [1]. In the 1990's, the specification of the global system for mobile communication (GSM) appeared, laying the foundation for the second-generation mobile network (2G), with the introduction of the digitalization of the transmission technology. The 2G network provided efficient voice transmission, but the service on the data transmission had very limited speed. For that reason, the third generation cellular network (3G) emerged, in 2000, to provide high-speed internet access. Multi-service capabilities, including e-mail, web browsing and multimedia transmission were thereby supported. As an evolution from the previous generations, the fourth generation mobile network (4G) appeared in 2009. Multiple-input multiple-output (MIMO) antenna technology was commercially implemented in 4G networks, supporting higher data rates and improved transmission robustness, by exploring the spatial multiplexing of wireless channels [2].

Though multiple technologies have been developed to improve the network throughput during the evolution of mobile networks, the bandwidth has always been a bottleneck for further increasing the channel capacity according to Shannon's law. Due to the spectrum saturation in the sub-7 GHz, the exponential growth in bandwidth demand has motivated the adoption of the mm-wave spectrum in the latest fifth generation of mobile communication (5G) [3–5]. According to the 3GPP specification [6], this new generation includes several frequency bands in the millimeter-wave (mm-wave) spectrum, as represented in blue in Fig. 1.1. It can be seen that much more spectrum than ever can be utilized for cellular communication.

However, the use of mm-wave bands also contributed to the manifestation of

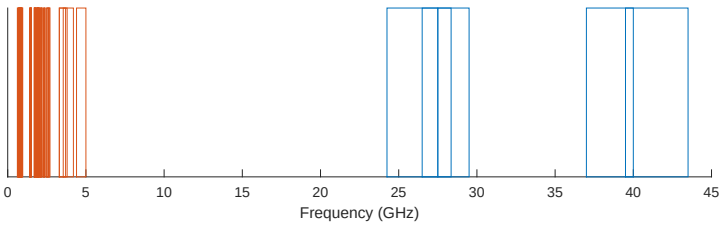

Fig. 1.1: 3GPP Release 16 spectrum bands for 5G/NR. The orange bands correspond to frequency range 1 (FR1) and are also employed in 4G/LTE. The blue bands compose frequency range 2 (FR2), also referred to as the mm-wave bands [6].

new issues to be dealt with. Among them, the dramatic changes of the wireless propagation environment in comparison to the conventional sub-7 GHz bands is one of the most critical challenges that must be tackled, and it requires novel antenna designs for both base station and user equipment (UE) [7]. Throughout the next two sections, the properties of the wireless channel propagation in mm-wave bands will be illustrated, and the corresponding antennas technologies in the 5G mm-wave bands will be discussed.

1.1 Millimeter-wave propagation

The introduction of 5G mm-wave mobile communication prompted the appearance of new challenges to be solved since the propagation environment affects the radiated fields differently at higher frequencies. This section includes some major challenges, from the propagation aspect, to operate a wireless network in the mm-wave band, such as path loss, penetration and other losses [8].

1.1.1 Path loss

Free-space path loss (FSPL) is one of the most critical factors to determine the coverage of wireless networks. It is derived from the Friis transmission formula, which expresses the power received by one antenna, P_r, at the distance d from another antenna, that is transmitting the power P_t at a certain wavelength λ. Assuming the antenna apertures of the transmitting and receiving antennas are A_t and A_r, respectively, the ratio between received and transmitted power can be expressed [9]:

$$P_r/P_t = \frac{A_t A_r}{(\lambda d)^2}. \tag{1.1}$$

If the effective antenna aperture, A_e, is expressed as

$$A_e = \frac{G\lambda^2}{4\pi}, \tag{1.2}$$

equation (1.1) can be rewritten as

$$P_r/P_t = G_t G_r \left(\frac{\lambda}{4\pi d}\right)^2. \tag{1.3}$$

From equation (1.3), the free-space path loss (FSPL) can be expressed as

$$FSPL = \left(\frac{4\pi d}{\lambda}\right)^2 = \left(\frac{4\pi df}{c}\right)^2 \tag{1.4}$$

with c representing the speed of light in vacuum and f the frequency.

The mm-wave bands in 5G employ higher frequencies than the conventional communications, which according to equation (1.3) results in a decreasing received power, if all the remaining parameters including antenna gain in transmission and reception are assumed to be constant through the frequency, as plotted in curve (a) of Fig. 1.2. Conversely, if the antenna aperture of either

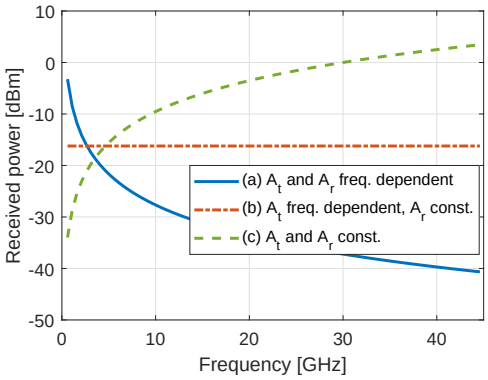

Fig. 1.2: Received power as a function of the frequency. The distance between the antennas is set to 100 m and the transmitted power to 10 W. (a) Constant antenna gain over frequency, with G_t= 30 dBi and G_r= 10 dBi. Both antenna apertures are frequency dependent. (b) G_t= 30 dBi (A_t frequency dependent), A_r= 0.01 m^2 constant with the frequency. (c) Constant antenna aperture over frequency, with A_t= 0.01 m^2 and A_r= 0.01 m^2.

transmitter or receiver antennas is fixed, curve (b) shows that the received power is constant with the frequency. The last scenario (c) consists of having both antenna apertures constant with the frequency. In this case, the received power increases with the frequency.

However, equation (1.3) assumes that both antennas are in line of sight (LoS), and in a real mobile communication channel, the path can be partially

obstructed by the objects, and other losses including penetration and shadowing loss need to be taken into account.

1.1.2 Penetration and other losses

In addition to the higher FSPL, millimeter-wave signals do not penetrate easily through buildings and windows. For instance, the attenuation of concrete to radio signals is 17.7 dB at frequencies below 3 GHz, while it becomes 175 dB at 40 GHz [10]. Therefore, the outdoor to indoor coverage becomes extremely challenging in mm-wave bands.

Foliage losses are also significant at mm-wave frequencies. The loss is given in [11], as

$$L = 0.2 f^{0.3} R^{0.6} \ (dB), \tag{1.5}$$

where f is the frequency in MHz, R is the depth of foliage transversed. The expression is only valid for a foliage depth less than 400 m.

Due to the shorter wavelength in the mm-wave band, the radio waves are less likely diffracted. The propagation of signals is more subject to the line of sight and the reflections from objects [11].

The attenuation due to atmospheric gases is usually less than 2 dB per kilometer in the mm-wave band (30-300 GHz), except for the water vapor and oxygen absorption peaks at 24 and 60 GHz, respectively, in which the attenuation is higher. Precipitation can also produce scattering in the mm-wave communications, since the raindrops have sizes comparable to the radio wavelengths.

As a summary, wireless signals transmitted in the mm-wave spectrum face a much more harsh propagation environment, with higher propagation losses. High gain antenna systems are therefore needed on both base stations and user equipments, to compensate for the less favorable propagation environment. For this reason, mm-wave antenna arrays are introduced in mobile terminals for 5G communication. Moreover, to cope with the highly random mobile channel in terms of angle of departure and arrival for wireless signals, a large beam steering angle is also required for antenna arrays in a 5G mobile terminal.

1.2 Antenna systems in mobile phones

As discussed, the inclusion of mm-wave bands has required novel antenna systems (e.g., antenna arrays) for mobile phones. Moreover, these mm-wave antennas need to coexist with the existing antenna systems for sub-7 GHz in an

already cramped space. In this section, the evolution of handset antennas is reviewed, with a specific focus on the new criteria of mm-wave antenna designs.

1.2.1 Evolution of mobile phone antennas

In the early commercial handheld devices, the antennas were external to the main printed circuit board (PCB) [12]. The sleeve dipole antenna, presented in Fig. 1.3(a), was the chosen geometry for one of the first devices. To reduce the size of the external antenna, the retractable monopole whip antenna was introduced (Fig. 1.3(b)). The antenna could operate as either a helix stubby antenna or a whip antenna, depending on whether it was retracted or extended.

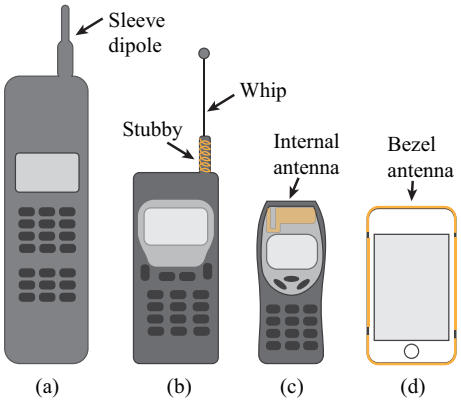

Fig. 1.3: Evolution of mobile phone antennas. (a) Sleeve dipole antenna. (b) Whip and stubby antenna. (c) Internal antenna. (d) Frame antenna.

Right before the beginning of the new millennium, the internal antenna emerged on the market (Fig. 1.3(c)). The most common types of internal antennas were the monopole, loop antenna, inverted-F antenna (IFA) and planar IFA (PIFA), which are presented in Fig. 1.4.

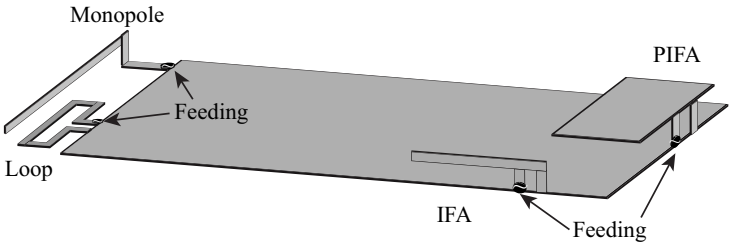

Fig. 1.4: Internal antennas for mobile phones.

Using the metallic frame of the mobile phone to allocate antennas has be-

come the dominant trend in recent years. This approach can provide mechanical robustness and aesthetics quality. In order to allocate multiple antennas, several slits are usually required to separate the frame into multiple sections (Fig. 1.3(d)). On the other hand, fully closed metallic frame structures have also been shown in academic publications [13] and commercial phones in recent years, to minimize the user body effect on the frame antennas, due to the strong electric fields around the slits.

To address the high losses in the mm-wave channel propagation for 5G communication, antenna arrays have been implemented in mobile handsets. The latest commercial 5G handsets, that are capable of tapping the mm-wave spectrum, usually include multiple mm-wave antenna array modules with four antenna elements each. An example of the array modules of a commercial 5G mm-wave-enabled phone is shown in Fig. 1.5. In this case, three mm-wave

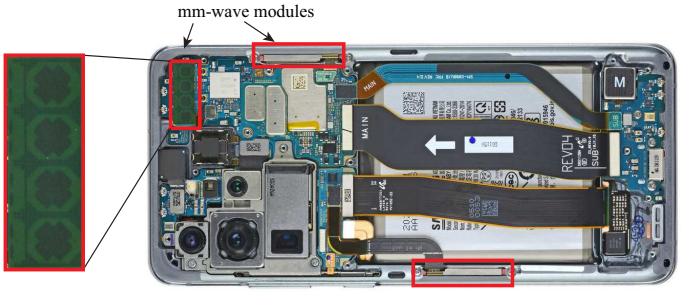

Fig. 1.5: mm-wave modules in the 5G-enabled phone Samsung Galaxy S20 Ultra. Source: ifixit.

antenna modules are contained. The mm-wave module on the top part of the phone includes four cross-shaped patches and four dipoles in the border of the module. To fully explore the advantage of the mm-wave spectrum, the antennas are also required to cover broad bandwidths (several GHz). Moreover, the antenna system is also recommended to be dual polarized, in order to improve the robustness to the polarization mismatch and support higher rank transmissions. These reasons have prompted the appearance of novel antenna designs and array systems for 5G mm-wave mobile terminals.

1.2.2 Millimeter-wave antenna topologies

For the convenience of antenna packaging and integration, planar antenna structures are more often preferred in mobile handsets. In this section, some typical planar antenna designs (see Fig. 1.6) will be reviewed and their advantage/disadvantages in terms of 5G mm-wave applications will also be discussed.

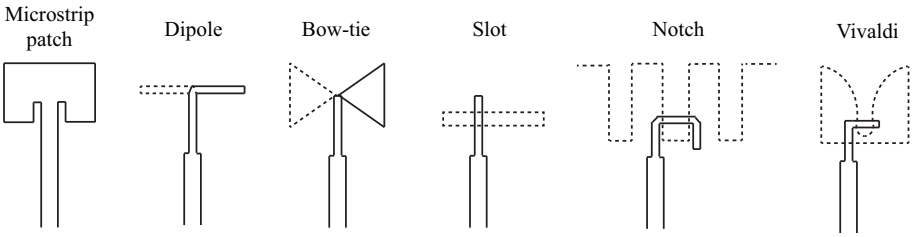

Fig. 1.6: Some typical planar antennas for mm-wave applications.

Microstrip patch. Its low-profile, planar shape and the ease of achieving dual-polarization makes it a good candidate for mm-wave mobile antennas. The boresight direction of the radiation pattern is normal to the patch.

The main drawback of patch antennas is their limited bandwidth, with typical values between 2 % to 5 % [14]. The dielectric constant selection and the thickness of the antenna substrate have an impact on the bandwidth, with larger bandwidths obtained when the permittivity is lower and the substrate is thicker [15]. Stacked-patch designs [16,17] and cavity-backed patch designs [18,19] are commonly employed techniques to increase the bandwidth.

Dipole antenna. A dipole antenna consists of two metallic branches split in the center and fed by a balanced transmission line so that the flowing currents in the feed line have equal magnitude and different signs. Typically, the total length of the dipole is chosen to be about 5 % shorter than half-wavelength, where the reactance is zero [20]. The radiation pattern of this kind of antenna is omnidirectional, with a null along the dipole axis. This antenna design presents a moderate bandwidth. An advantage of the printed dipole, with respect to the microstrip patch antenna, is that it employs less substrate area [21].

Bow-tie antenna. The bow-tie antenna is proposed to increase the bandwidth of dipole antennas, with a simple bow-tie shaped design [22,23]. The characteristic impedance of a bow-tie antenna can be obtained from

$$Z_c = 120 \ln \left(\cot \left(\frac{\alpha}{4} \right) \right), \tag{1.6}$$

with α the opening angle of each side. To obtain wideband performance and a compact structure, the angle usually ranges from 60° to 90°. For better lower frequency performance, the length of the bow-tie element should be longer [24].

A bow-tie antenna yields a broadside radiation pattern and it is difficult to make it dual-polarized.

Slot antenna. A slot is a narrow-width aperture, cut in a metallic layer. The length of the antenna is set to half-wavelength. This kind of antenna presents a moderate bandwidth, which is dependent on the antenna width [14]. It yields a front and rear broadside radiation pattern, when it is etched in a finite ground plane. This can be unattractive for some applications, where the rear beam points towards the user head.

Another disadvantage is that the slot antenna excites strong currents on the ground plane, where the antenna performance can be highly affected by the substrate and other components connected to the phone chassis. [25,26].

Notch antenna. It is formed by a half-slot cut in the ground plane. The slot is fed with a bent microstrip line [27]. The input impedance of a notch antenna is usually lower than 50 Ω. The realized gain of the notch antenna is higher than the normal half-wavelength slot, since the fields are more confined [28]. This antenna yields radiation in half-sphere. The bandwidth of this antenna is also moderate and it is difficult to make it dual-polarized.

Vivaldi antenna. It presents a simple and low-cost design, where an exponentially tapered slot is etched from a metallic layer. The antenna radiates through the aperture created by the tapered slot between the antenna arms [29,30]. This aperture width determines the lower operational frequency, while the narrowest width of the tapered slot determines the higher operational frequency. The aperture of the structure has a strong influence on the antenna gain, with larger dimensions providing higher gain values [31]. The antenna provides a large bandwidth with an end-fire radiation pattern. Even though this antenna structure has become quite popular for mm-wave applications [32–34], it is difficult to make it dual-polarized.

1.2.3 Beamforming architectures

Single antenna element designs have been reviewed above. However, as mentioned in Section 1.1, the antenna systems in 5G mm-wave communications are required to have high gain to compensate for the more pronounced propagation loss. Since it is hard to reach the desired gain with single-element antennas, arrays are needed in mobile phones. Furthermore, the broad angular coverage required for mobile communications and the high gain antenna systems that yield narrow beams have made it necessary to steer the beam of the arrays in different directions. Beamforming consists of sending the same data symbol over each element antenna, with a different complex weight in all of them. The weight choice for every element can be selected based on an algorithm that

intends to optimize a certain parameter, e.g. the signal-to-interference ratio (SIR) [35].

From an implementation point of view, there are several beamforming architectures that can be potentially used for 5G mm-wave communication, which are described below:

1. Analog beamforming

   In the analog beamforming, the complex weights are added on the analog domain with a single data stream fed into the array. Analog beamforming can be implemented by radio frequency (RF) switches, phase shifters or lens antennas connected to the antenna elements of the mm-wave array [36,37]. These elements provide the appropriate time delay or phase shifting. The scheme is presented in Fig. 1.7 (a). Even though it is a simple and cost-effective method, it has less flexibility than the digital beamforming.

2. Digital beamforming

   Instead of placing the phase shifters in the RF domain, a full digital beamforming carries out the precoding and combining of signals in the digital baseband. An individual RF chain is required for each antenna element, as shown in Fig. 1.7 (b). Digital beamforming offers better flexibility than analog beamforming, but also requires a more complex architecture and more power consumption.

3. Hybrid beamforming

   Hybrid beamforming intends to combine the advantages from both analog beamforming and digital beamforming. It uses low RF chains as the required data streams, with the beamforming performed in the analog domain. Hybrid beamforming is designed to reach optimal performance with less hardware expense and lower power consumption [35]. These features make it currently to be the more feasible architecture for 5G mm-wave antenna array. The scheme is plotted in Fig. 1.7 (c).

1.3 Performance metrics

The addition of the mm-wave frequency bands (FR2) in 5G has not only triggered the novel antenna designs, but also required the development of new figures of merit and test methods to evaluate the performance of antenna systems. In the case of the 5G new radio (NR) user equipment (UE) in FR2, over-the-air (OTA) testing methods are defined by 3GPP TR 38.810 [39]. One

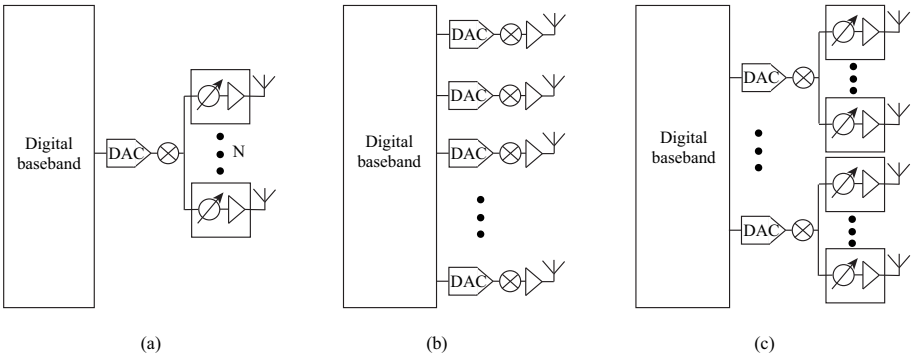

Fig. 1.7: Beamforming architectures reproduced from [38]. (a) Analog beamforming. (b) Digital beamforming. (c) Hybrid beamforming.

of the reasons to have OTA tests instead of conductive tests is that mm-wave antennas are integrated into the RF front-end and therefore, the antenna connectors cannot be accessed and tested. Thus, the OTA tests become necessary.

Conventional performance metrics to evaluate the antenna systems, e.g. antenna total efficiency, total isotropic sensitivity (TIS), and total radiated power (TRP) are not sufficient anymore since they are omnidirectional parameters, which cannot perform the proper evaluation on a beam-steering antenna array. Therefore, some novel metrics have been proposed in the academic research and the standardization body in the past few years to examine the performance of mm-wave antenna arrays for mobile applications:

- Total scan pattern (TSP)

  As discussed earlier, to cope with a highly random propagation environment for mobile communications, mm-wave antenna arrays for mobile handsets need to achieve large beam-steering angles. In [27], the concept of total scan pattern is presented to provide an overall picture of how large solid angles a mm-wave antenna array can cover with beamsteering.

  The total scan pattern represents the maximum achievable gain at every angular point of the sphere, with all the possible beams of the array, which can be written as

  $$G_{tot}(\Omega) = max[G_1(\Omega), G_2(\Omega), ..., G_n(\Omega)], \tag{1.7}$$

  where n represents the beam index and Ω stands for solid angle (θ, Φ).

  As an example, the total scan pattern of two different microstrip patch arrays has been presented in Fig. 1.8. The effect of the PCB can be observed in the total scan pattern of the parallel array, which blocks the radiation towards the lower hemisphere, and reduces considerably the

value of the realized gain. On the other hand, the perpendicular array shows a better omnidirectional coverage as a result of the smaller size of the ground plane behind the antenna elements.

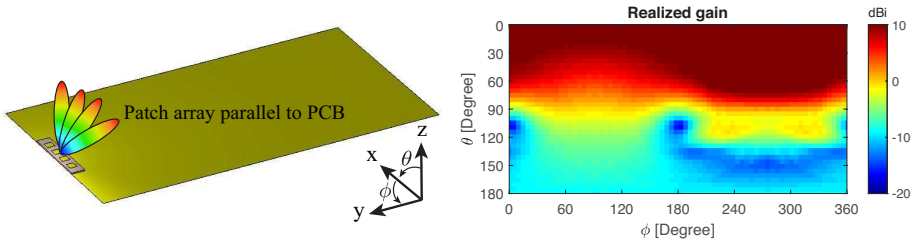

(a)

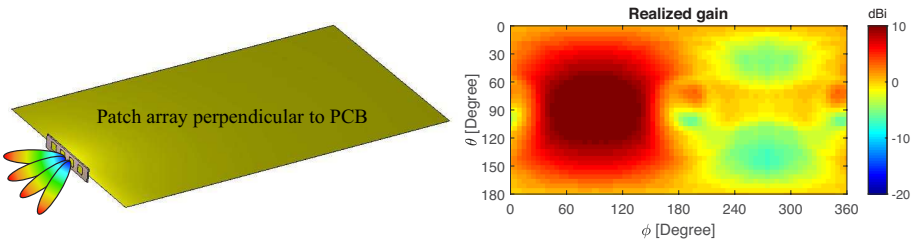

(b)

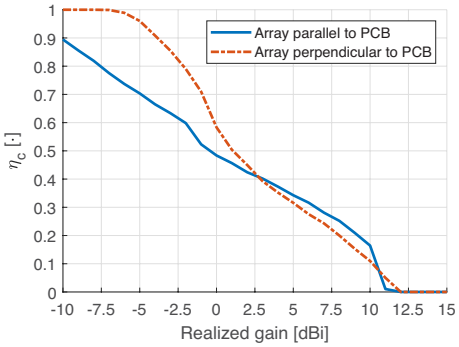

(c)

Fig. 1.8: (a) TSP at 28.5 GHz of the patch array parallel to PCB. (b) TSP at 28.5 GHz of the patch array perpendicular to PCB. (c) Coverage efficiency comparison.

- Coverage efficiency

  While the TSP can provide an intuitive picture of the spatial coverage of a beam-steerable array, the coverage efficiency is defined to quantify its spatial coverage. It can be calculated from its total scan pattern for the

minimum antenna gain that ensures that the link is established

$$\eta_c = \frac{Covered\ solid\ angle}{Maximum\ solid\ angle}, \tag{1.8}$$

with the covered solid angle defined as the summation of all the solid angles in the total scan pattern, that have a gain higher than a certain threshold value. The maximum solid angle can be chosen as the total sphere, i.e. 4π steradians, to take into consideration the arbitrary angle of arrival of the incoming signal [27].

Considering the previous example of the two arrays, one parallel and the other perpendicular to the PCB, their coverage efficiency has been plotted in Fig. 1.8(c). The perpendicular array can yield isotropic coverage with a gain of -7.5 dBi, while the parallel array would only cover 80 % of the sphere for the same threshold value. On the other hand, if the gain range is required to be above 2.5, the parallel array has better coverage in general, even though the array with higher peak realized gain is the perpendicular one.

- Spherical coverage

  In the 3GPP Technical Specification 38.101-2 [6], a spherical coverage requirement is defined by the effective isotropic radiated power (EIRP) and effective isotropic sensitivity (EIS) values at certain percentile on the cumulative distribution function (CDF) curve, for uplink and downlink, respectively, where the percentile depends on the power class (i.e., UE type). The CDF is the probability, P, that a random variable, X, will take a value less than or equal to x

  $$CDF(x) = P(X \leq x). \tag{1.9}$$

  Taking the uplink spherical coverage as an example, the EIRP is defined as the power that a theoretical isotropic antenna should radiate to produce the same radiation intensity in the direction of maximum gain of an antenna. The EIRP includes the losses in the transmission line and connectors and includes the antenna gain

  $$EIRP(dB) = P_t - L_c + G, \tag{1.10}$$

  where P_t represents the transmitter power, L_c cable losses and G the antenna gain expressed in dBi.

  The CDF curve is obtained by measuring the achievable EIRP on test directions over the whole sphere. The spherical coverage requirement assures that the UE can transmit EIRP no lower than the defined EIRP limit over the required percentile [40].

The minimum requirement of peak EIRP by 3GPP for power class 3 UE corresponds to CDF=100 % and it is listed in Table 1.1. Power class 3 UE is defined for handheld devices, e.g. mobile phones.

Table 1.1: UE minimum peak EIRP (at the 100 %-tile CDF) and spherical coverage (at the 50 %-tile CDF) for power class 3 [6].

Operating band	Min. peak EIRP (dBm) at 100 %-tile CDF	Min. spherical coverage EIRP (dBm) at 50 %-tile CDF
n257 (26.50-29.50 GHz)	22.4	11.5
n258 (24.25-27.50 GHz)	22.4	11.5
n259 (39.50-43.50 GHz)	18.7	5.8
n260 (37.00-40.00 GHz)	20.6	8
n261 (27.50-28.35 GHz)	22.4	11.5

Limiting the definition of the power class to minimum peak EIRP at the 100%-tile does not provide a complete picture of the beam-steerable antenna array performance and, therefore, in 3GPP, the spherical coverage required for power class 3 is defined as the minimum EIRP at the 50%-tile of the distribution. The minimum EIRP at the 50%-tile CDF is also listed in Table 1.1.

Going back to the example of the parallel and perpendicular arrays, the minimum EIRP at the 50%-tile CDF in the band covering 28.5 GHz (n257) is 11.5 dBm. Fig. 1.9 represents the CDF as a function of the EIRP, for an assumed 11 dBm value of TRP. As it can be seen from the figure, the EIRP values for a $\eta_c = 50$ % are 11 dBm and 12 dBm, for the parallel and perpendicular array respectively. In this example, the parallel array fails to meet the requirement for the TRP assumed and higher input power to the antenna array would thus, be required.

1.4 Implementation of the mm-wave arrays in mobile phones

Even though advances in antenna arrays have been developed over decades, some practical implementation issues of mm-wave antenna systems for mobile handsets have just emerged recently with the launch of 5G mm-wave handsets. Antenna systems for mobile terminals typically suffer a performance deterioration after the integration, which becomes even more critical at mm-wave frequency bands due to the shorter wavelength. In addition, the user effects on the mobile antenna system need to be considered. In this section, some

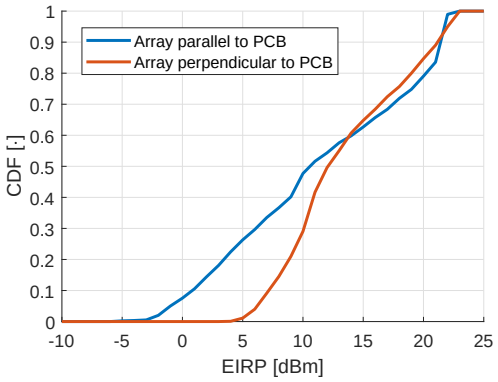

Fig. 1.9: CDF of EIRP of the two examples of Fig. 1.8.

practical implementation issues will be briefly discussed.

1.4.1 Antenna array placement

The limited space available in phones requires the arrays to occupy as small areas as possible, challenging thus the mm-wave array design. Moreover, the array is more sensitive to the presence of other electronic components and device housing. Therefore, it is important to select a proper placement that maximizes the array performance.

In [41], two different UE designs are studied to evaluate the spherical coverage. The *face* design (Fig. 1.10(a)) consists of two antenna modules on the front and back corners of the handset display and rear case placed diagonally. The *edge* design considers three antenna modules placed on three different faces of the frame.

The presence of the display in the *face* design can incur manufacturing increased costs and mounting problems for the mm-wave antennas. The signal attenuation of glass covers is larger than plastic covers due to the higher scattering [41]. In order to provide the same EIRP in the desired direction, more power is needed to be transmitted through the glass material. Moreover, for an acceptable spherical coverage in the *face* design, two modules are required, one in the front and one in the back. The front module exposes the user head to more radiation. Due to the aforementioned reasons, the *edge* modules provide the best overall advantages, such as low cost and power consumption, implementation ease and minimized exposure-related challenges.

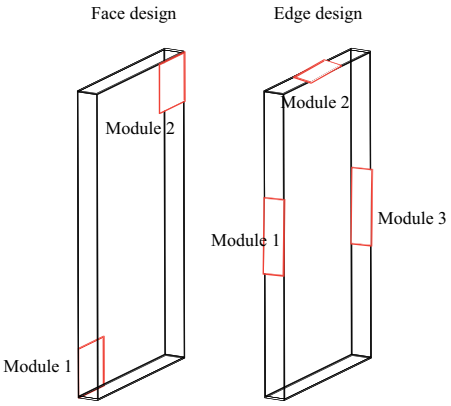

Fig. 1.10: Re-plotted collocation models from Paper [41].

1.4.2 Influence of the phone housing

Apart from the array placement, the varied material for the phone housing can impact the mm-wave antenna array radiation differently. The study from [42] evaluated the influence of a simplified phone housing on the antenna array performance. It was shown that the effect of the back cover of the phone does not only depend on the cover material, but also on the steering angle of the radiation pattern. The radiation pattern is more robust to changes in the back cover material when the beam is pointing in the boresight direction, but becomes more sensitive when the incident angle is tilted. The radiation pattern pointing 60° away from the boresight direction for different rear cover materials has been plotted in Fig. 1.11. The sidelobes contribution is more prominent with the glass cover.

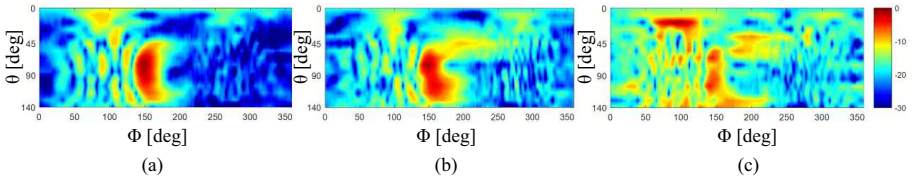

Fig. 1.11: Re-plotted normalized radiation pattern pointing 60° away from the boresight direction from Paper [42]. (a) Without phone housing. (b) With plastic back cover. (c) With glass back cover.

1.4.3 User body effect

Antenna systems in mobile handsets usually operate nearby user's body. The proximity of the human body can influence the antenna performance in terms

of impedance match, radiation efficiency, antenna gain and distortion in the radiation pattern.

In the sub-7 GHz frequency bands, the user body effects mainly contribute to a loss in the antenna total efficiency, which can be further broken down to the absorption loss and impedance mismatch loss. Ascending to mm-wave frequency bands, the reduction of the wavelength is such that the user body is unlikely to be in the reactive near field of the antenna and the penetration depth of electromagnetic waves is smaller. Therefore, the corresponding impedance mismatch loss and absorption loss are typically reduced in comparison to sub-7 GHz bands [43–45]. On the other hand, the shadowing loss and the body blockage have become the predominant effects. They show an impact on the spherical coverage of the mm-wave mobile terminal that cannot be disregarded [46–48].

To evaluate the user effect on a mm-wave antenna system in a mobile handset, a finger covering the boresight direction of the antenna has been simulated as a part of this work. The antenna consists of a dual-band dual-fed patch antenna, with port 1 yielding the vertical polarization and port 2, the horizontal. The antenna is placed 1 mm away from the plastic frame. The front cover is made of glass ($\epsilon_r = 6.84$) and the rear case is made of plastic ($\epsilon_r = 3$).

A comparison of the reflection coefficient and radiation efficiency of both covered and uncovered models is presented in Fig. 1.12. As can be observed,

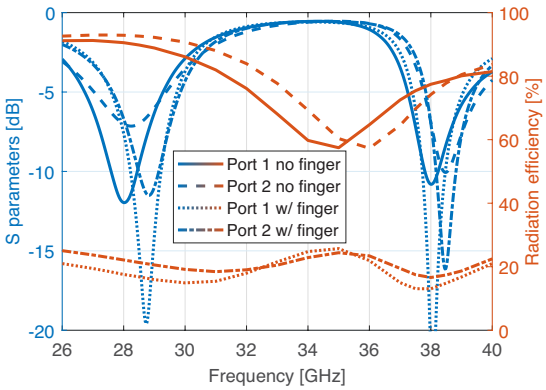

Fig. 1.12: Reflection coefficient and radiation efficiency comparison with and without finger.

the impedance match of the antenna is only minor affected by the presence of the finger, while the radiation efficiency has decreased around 70 % at both resonances. This example presents an extreme case, where the finger is located right above the antenna. The obstruction of the finger in the radiation patterns can be clearly observed, which causes the radiation of the mm-wave antenna to propagate in other directions. The peak gain levels of the antenna in Fig.

1.13(c-d) are around −1.6 dBi, while the uncovered antenna yields 5.8 dBi and 4.3 dBi for port 1 and 2, respectively.

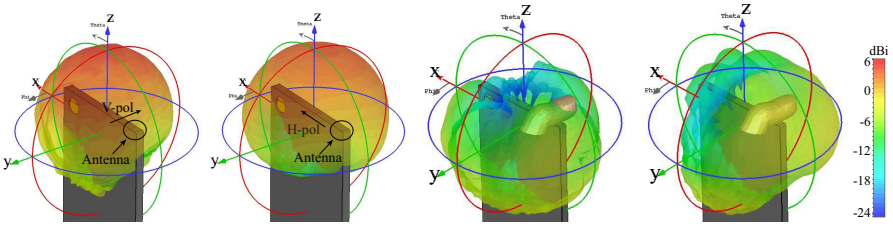

(a) (b) (c) (d)

Fig. 1.13: Realized gain radiation pattern comparison. (a) Port 1 uncovered. (b) Port 2 uncovered. (c) Port 1 covered with finger. (d) Port 2 covered with finger.

In [49], a 5 dB degradation in the 50 %-tile of the CDF is shown when a finger is covering the antenna. The EIRP of the user holding the handset is also presented, and there is a $25-30$ dB loss due to the body shadow. The blockage loss degrades the spherical coverage dramatically. In [50], a comparison of the antenna in free space and with the hand and head phantoms is shown. The radiation pattern becomes more directive with strong ripples and the spherical coverage decreases due to the effects from the hand and head. In [51], an antenna array is moved along the chassis edges to evaluate the best antenna array placement to reduce the user impact. The results show that the corners are the best placements to suppress the user shadowing effects in terms of coverage efficiency.

1.4.4 Electromagnetic field exposure of handsets

The previous section studied the impact of the user's body on the antenna performance, but the user, on the other hand, is also exposed to the electromagnetic fields (EMF) radiated from mobile handsets. All the commercial handsets must comply with the regulated EMF limits on personal exposure issued by the International Commission of Non-Ionizing Radiation Protection (ICNIRP), the U.S Federal Communications Commission (FCC), or the Institute of Electrical and Electronics Engineers (IEEE).

The exposure of the human body can be described by the specific energy absorption rate (SAR), measured in W/kg,

$$SAR = \frac{\sigma |E|^2}{\rho}, \tag{1.11}$$

where σ is the conductivity, E is the root means square of the internal electric-

field and ρ is the density of the tissue. This metric on EMF exposure compliance test is used below 6 GHz for mobile handsets [52]. For public exposure of cellular telephones, the FCC limit is a SAR level of 1.6 W/kg averaged over 1 g of tissue mass, while the ICNIRP limit is 2 W/kg averaged over 10 g tissue for the head.

On the other hand, above 6 GHz, the absorption of EMFs is more superficial, so the exposure is described in terms of the time averaged incident power density (PD) over an averaging area (W/m^2) [52],

$$S_{ab} = \frac{1}{A} \iint_A Re[E \times H^*] ds, \tag{1.12}$$

where ds is the integral variable vector normal to the averaging area, A. The PD limit defined by the FCC [53] is 10 W/m^2 averaged over 4 cm^2 of area in the frequency range 6-100 GHz. Conversely, the limitation by ICNIRP [52] and IEEE [54] is frequency-dependent, $55f^{-0.177}$ (W/m^2), applicable in the range 6-300 GHz. The averaging area is 4 cm^2 for IEEE in the whole interval, while, for ICNIRP, it is only valid from 6 to 30 GHz. For the rest of the frequency range, ICNIRP adopts a 1 cm^2 averaging area.

Several studies of electromagnetic field exposure can be found in the literature. In [55], the RF EMF exposure is measured in 28 realistic scenarios for frequencies below 2.5 GHz. The higher exposure was obtained in trains and buses, where the changing conditions required higher transmitted signals for mobile phones. The main concern regarding exposure is an increase in body temperature [56]. The investigation in [57], shows that at the transition frequency from SAR to PD, the temperature variation decreases three and four times for the FCC and ICNIRP limits, respectively. For a 5G mm-wave device to comply with the maximum permitted exposure level, its output power and EIRP level are, therefore, limited. The maximum allowed transmitted power and EIRP levels to meet the exposure limitations, for various array configurations in 5G mm-wave handsets, are reported in [58]. The results show, that the 3GPP 5G NR specification of the minimum peak EIRP, can be generally met (without significant power back-off) when complying with the proposed ICNIRP, IEEE and FCC exposure limits at 28 GHz and 39 GHz.

1.5 Aims of the thesis

With the challenges of the new generation of mobile communication described above, this dissertation focuses on resolving the issues regarding the integration of mm-wave antenna arrays in mobile handsets. The term *integration* in this thesis is not only used in the sense of locating the mm-wave arrays inside the

phone chassis, but also to refer to the placement of mm-wave arrays in a shared volume with the sub-7 GHz antennas.

The transmission of electromagnetic waves through the handset rear cover depends on the material chosen, which can be plastic for low-end devices and glass or metal for top-tier phones. Chapter 2 evaluates the performance of a mm-wave antenna with the rear cover on top of it for different materials, with both fundamental theory and full-wave simulations, which are discussed in Sections 2.1 and 2.2, respectively. In Section 2.3, different solutions have also been studied to reduce the effect of the rear cover on the mm-wave antenna radiation, including the restriction of the induced surface current. The limited space in mobile phones has also prompted the appearance of antennas-on-display. A method to improve the performance of antennas-on-display by controlling the propagation of surface waves, has also been proposed in the same section.

Moreover, the thesis has also largely focused on reducing the metallic frame obstruction to the radiation of mm-wave arrays, which is discussed in Chapter 3. The impact of different frame materials on the mm-wave antenna performance has been investigated first in Section 3.1. Metallic frames reflect back all the radiation impinging on them and prevent the enclosed antenna radiation to propagate towards the desired direction. Three different methods are then described to solve this issue, and their advantages and disadvantages are assessed in Section 3.2. The mm-wave antenna array, in the proposed methods, is embedded within the metallic frame, which acts as a sub-7 GHz antenna. This arrangement ensures that the proposed solutions are feasible for some practical scenarios.

References

[1] N. Chandran and M. C. Valenti, "Three generations of cellular wireless systems," *IEEE Potentials*, vol. 20, no. 1, pp. 32–35, 2001.

[2] H. Viswanathan and M. Weldon, "The past, present, and future of mobile communications," *Bell Labs Technical Journal*, vol. 19, pp. 8–21, 2014.

[3] T. S. Rappaport, S. Sun, R. Mayzus, H. Zhao, Y. Azar, K. Wang, G. N. Wong, J. K. Schulz, M. Samimi, and F. Gutierrez, "Millimeter wave mobile communications for 5G cellular: It will work!" *IEEE Access*, vol. 1, pp. 335–349, 2013.

[4] J. G. Andrews, S. Buzzi, W. Choi, S. V. Hanly, A. Lozano, A. C. Soong, and J. C. Zhang, "What will 5G be?" *IEEE Journal on selected areas in communications*, vol. 32, no. 6, pp. 1065–1082, 2014.

[5] A. Gupta and R. K. Jha, "A survey of 5G network: Architecture and emerging technologies," *IEEE access*, vol. 3, pp. 1206–1232, 2015.

[6] "User Equipment (UE) radio transmission and reception; Part 2: Range 2 Standalone (3GPP TS 38.101-2 version 16.4.0 Release 16)," 3rd Generation Partnership Project (3GPP), Technical Specification (TS) 38.101-2, 07 2020, version 16.4.0.

[7] Y. Huo, X. Dong, and W. Xu, "5G cellular user equipment: From theory to practical hardware design," *IEEE Access*, vol. 5, pp. 13 992–14 010, 2017.

[8] Y. Li, D. Jin, L. Su, and A. V. Vasilakos, "A survey of millimeter wave (mmWave) communications for 5G: Opportunities and challenges," *pp1-20, April*, 2015.

[9] H. T. Friis, "A note on a simple transmission formula," *Proceedings of the IRE*, vol. 34, no. 5, pp. 254–256, 1946.

[10] Z. Pi and F. Khan, "An introduction to millimeter-wave mobile broadband systems," *IEEE Communications Magazine*, vol. 49, no. 6, pp. 101–107, 2011.

[11] M. Marcus and B. Pattan, "Millimeter wave propagation: spectrum management implications," *IEEE Microwave Magazine*, vol. 6, no. 2, pp. 54–62, 2005.

[12] Z. Zhang, *Antenna design for mobile devices*. John Wiley & Sons, 2017.

[13] K. Zhao, S. Zhang, K. Ishimiya, Z. Ying, and S. He, "Body-insensitive multimode MIMO terminal antenna of double-ring structure," *IEEE Transactions on Antennas and Propagation*, vol. 63, no. 5, pp. 1925–1936, 2015.

[14] C. A. Balanis, *Antenna theory: analysis and design*. John wiley & sons, 2016.

[15] D. M. Pozar, "Microstrip antennas," *Proceedings of the IEEE*, vol. 80, no. 1, pp. 79–91, 1992.

[16] S. Long and M. Walton, "A dual-frequency stacked circular-disc antenna," *IEEE Transactions on Antennas and Propagation*, vol. 27, no. 2, pp. 270–273, 1979.

[17] A. Sabban, "A new broadband stacked two-layer microstrip antenna," in *1983 Antennas and Propagation Society International Symposium*, vol. 21. IEEE, 1983, pp. 63–66.

[18] J. T. Aberle and F. Zavosh, "Analysis of probe-fed circular microstrip patches backed by circular cavities," *Electromagnetics*, vol. 14, no. 2, pp. 239–258, 1994.

[19] R. Mailloux, "On the use of metallized cavities in printed slot arrays with dielectric substrates," *IEEE Transactions on Antennas and Propagation*, vol. 35, no. 5, pp. 477–487, 1987.

[20] T. A. Milligan, *Modern antenna design*. John Wiley & Sons, 2005.

[21] D. Pozar, "Considerations for millimeter wave printed antennas," *IEEE Transactions on Antennas and Propagation*, vol. 31, no. 5, pp. 740–747, 1983.

[22] K. Loi, S. Uysal, and M. Leong, "Design of a wideband microstrip bowtie patch antenna," *IEE Proceedings-Microwaves, Antennas and Propagation*, vol. 145, no. 2, pp. 137–140, 1998.

[23] Y.-D. Lin and S.-N. Tsai, "Analysis and design of broadside-coupled striplines-fed bow-tie antennas," *IEEE Transactions on Antennas and Propagation*, vol. 46, no. 3, pp. 459–460, 1998.

[24] Guo Chen and R. C. Liu, "A 900 MHz shielded bow-tie antenna system for ground penetrating radar," in *Proceedings of the XIII Internarional Conference on Ground Penetrating Radar*, 2010, pp. 1–6.

[25] B. Xu, K. Zhao, Z. Ying, S. He, and J. Hu, "Investigation of surface waves suppression on 5G handset devices at 15 GHz," in *2016 10th European Conference on Antennas and Propagation (EuCAP)*. IEEE, 2016, pp. 1–4.

[26] S. Zhang, X. Chen, I. Syrytsin, and G. F. Pedersen, "A planar switchable 3-D-coverage phased array antenna and its user effects for 28-GHz mobile terminal applications," *IEEE Transactions on Antennas and Propagation*, vol. 65, no. 12, pp. 6413–6421, 2017.

[27] J. Helander, K. Zhao, Z. Ying, and D. Sjöberg, "Performance analysis of millimeter-wave phased array antennas in cellular handsets," *IEEE Antennas and Wireless Propagation Letters*, vol. 15, pp. 504–507, 2016.

[28] M. Aboualalaa, A. B. Abdel-Rahman, A. Allam, R. K. Pokharel, K. Yoshitomi, and H. Elsadek, "Compact 24 GHz half-slot antenna for energy combining," in *2018 International Applied Computational Electromagnetics Society Symposium (ACES)*, 2018, pp. 1–2.

[29] R. Janaswamy and D. Schaubert, "Analysis of the tapered slot antenna," *IEEE Transactions on Antennas and Propagation*, vol. 35, no. 9, pp. 1058–1065, 1987.

[30] D. Schaubert, E. Kollberg, T. Korzeniowski, T. Thungren, J. Johansson, and K. Yngvesson, "Endfire tapered slot antennas on dielectric substrates," *IEEE Transactions on antennas and propagation*, vol. 33, no. 12, pp. 1392–1400, 1985.

[31] P. Gibson, "The vivaldi aerial," in *1979 9th European Microwave Conference*. IEEE, 1979, pp. 101–105.

[32] R. Rodriguez-Cano, S. Zhang, K. Zhao, and G. F. Pedersen, "Reduction of main beam-blockage in an integrated 5G array with a metal-frame antenna," *IEEE Transactions on Antennas and Propagation*, vol. 67, no. 5, pp. 3161–3170, 2019.

[33] R. Rodriguez-Cano, K. Zhao, S. Zhang, and G. F. Pedersen, "Handset frame blockage reduction of 5G mm-wave phased arrays using hard surface inspired structure," *IEEE Transactions on Vehicular Technology*, vol. 69, no. 8, pp. 8132–8139, 2020.

[34] J. Kurvinen, H. Kähkönen, A. Lehtovuori, J. Ala-Laurinaho, and V. Viikari, "Co-designed mm-wave and LTE handset antennas," *IEEE Transactions on Antennas and Propagation*, vol. 67, no. 3, pp. 1545–1553, 2019.

[35] I. Ahmed, H. Khammari, A. Shahid, A. Musa, K. S. Kim, E. De Poorter, and I. Moerman, "A survey on hybrid beamforming techniques in 5G: Architecture and system model perspectives," *IEEE Communications Surveys Tutorials*, vol. 20, no. 4, pp. 3060–3097, 2018.

[36] W. Hong, Z. H. Jiang, C. Yu, J. Zhou, P. Chen, Z. Yu, H. Zhang, B. Yang, X. Pang, M. Jiang *et al.*, "Multibeam antenna technologies for 5G wireless communications," *IEEE Transactions on Antennas and Propagation*, vol. 65, no. 12, pp. 6231–6249, 2017.

[37] P. Hall and S. Vetterlein, "Review of radio frequency beamforming techniques for scanned and multiple beam antennas," in *IEE Proceedings H (Microwaves, Antennas and Propagation)*, vol. 137, no. 5. IET, 1990, pp. 293–303.

[38] T. Cameron, "Bits to beams: Rf technology evolution for 5G millimeter wave radios," *Tech. Art., Analog Devices Inc*, 2018.

[39] "Technical Specification Group Radio Access Network; NR; Study on test methods (Release 16)," 3rd Generation Partnership Project (3GPP), Technical Report (TR) 38.810, 12 2019, version 16.5.0.

[40] "Technical Specification Group Radio Access Network; General aspects for User Equipment (UE) Radio Frequency (RF) for NR (Release 15)," 3rd Generation Partnership Project (3GPP), Technical Report (TR) 38.817-01, 03 2019, version 15.3.0.

[41] V. Raghavan, M. Chi, M. A. Tassoudji, O. H. Koymen, and J. Li, "Antenna placement and performance tradeoffs with hand blockage in millimeter wave systems," *IEEE Transactions on Communications*, vol. 67, no. 4, pp. 3082–3096, 2019.

[42] K. Zhao, S. Zhang, Z. Ho, O. Zander, T. Bolin, Z. Ying, and G. F. Pedersen, "Spherical coverage characterization of 5G millimeter wave user equipment with 3GPP specifications," *IEEE Access*, vol. 7, pp. 4442–4452, 2019.

[43] M. Heino, C. Icheln, and K. Haneda, "Finger effect on 60 GHz user device antennas," in *2016 10th European Conference on Antennas and Propagation (EuCAP)*, 2016, pp. 1–5.

[44] C. Buey, F. Ferrero, L. Lizzi, P. Ratajczak, Y. Benoit, and L. Brochier, "Investigation of hand effect on a handheld terminal at 11 GHz," in *2016 10th European Conference on Antennas and Propagation (EuCAP)*, 2016, pp. 1–5.

[45] T. Wu, T. S. Rappaport, and C. M. Collins, "Safe for generations to come: Considerations of safety for millimeter waves in wireless communications," *IEEE Microwave Magazine*, vol. 16, no. 2, pp. 65–84, 2015.

[46] I. Syrytsin, S. Zhang, G. F. Pedersen, K. Zhao, T. Bolin, and Z. Ying, "Statistical investigation of the user effects on mobile terminal antennas for 5G applications," *IEEE Transactions on Antennas and Propagation*, vol. 65, no. 12, pp. 6596–6605, 2017.

[47] K. Zhao, J. Helander, D. Sjöberg, S. He, T. Bolin, and Z. Ying, "User body effect on phased array in user equipment for the 5G mmwave communication system," *IEEE Antennas and Wireless Propagation Letters*, vol. 16, pp. 864–867, 2017.

[48] K. Zhao, C. Gustafson, Q. Liao, S. Zhang, T. Bolin, Z. Ying, and S. He, "Channel characteristics and user body effects in an outdoor urban scenario at 15 and 28 GHz," *IEEE Transactions on Antennas and Propagation*, vol. 65, no. 12, pp. 6534–6548, 2017.

[49] K. Zhao, Z. Ying, S. Zhang, and G. Pedersen, "User body effects on mobile antennas and wireless systems of 5G communication," in *2020 14th European Conference on Antennas and Propagation (EuCAP)*, 2020, pp. 1–5.

[50] R. Rodríguez-Cano, S. Zhang, K. Zhao, and G. F. Pedersen, "User body interaction of 5G switchable antenna system for mobile terminals at 28 GHz," in *2019 13th European Conference on Antennas and Propagation (EuCAP)*, 2019, pp. 1–4.

[51] I. Syrytsin, S. Zhang, G. F. Pedersen, and A. S. Morris, "User-shadowing suppression for 5G mm-wave mobile terminal antennas," *IEEE Transactions on Antennas and Propagation*, vol. 67, no. 6, pp. 4162–4172, 2019.

[52] I. C. on Non-Ionizing Radiation Protection *et al.*, "Guidelines for limiting exposure to electromagnetic fields (100 kHz to 300 GHz)," *Health Physics*, vol. 118, no. 5, pp. 483–524, 2020.

[53] FCC, "Fcc 15-138," *Notice of proposed rulemaking*, 2015. [Online]. Available: https://docs.fcc.gov/public/attachments/FCC-15-138A1.pdf

[54] "IEEE standard for safety levels with respect to human exposure to electric, magnetic, and electromagnetic fields, 0 hz to 300 GHz," *IEEE Std C95.1-2019 (Revision of IEEE Std C95.1-2005/ Incorporates IEEE Std C95.1-2019/Cor 1-2019)*, pp. 1–312, 2019.

[55] W. Joseph, G. Vermeeren, L. Verloock, M. M. Heredia, and L. Martens, "Characterization of personal RF electromagnetic field exposure and actual absorption for the general public," *Health physics*, vol. 95, no. 3, pp. 317–330, 2008.

[56] M. A. Jamshed, F. Heliot, and T. W. Brown, "A survey on electromagnetic risk assessment and evaluation mechanism for future wireless communication systems," *IEEE Journal of Electromagnetics, RF and Microwaves in Medicine and Biology*, vol. 4, no. 1, pp. 24–36, 2019.

[57] K. Foster and D. Colombi, "Thermal response of tissue to RF exposure from canonical dipoles at frequencies for future mobile communication systems," *Electronics Letters*, vol. 53, no. 5, pp. 360–362, 2017.

[58] B. Xu, K. Zhao, Z. Ying, D. Sjöberg, W. He, and S. He, "Analysis of impacts of expected RF EMF exposure restrictions on peak EIRP of 5G user equipment at 28 GHz and 39 GHz bands," *Ieee Access*, vol. 7, pp. 20 996–21 005, 2019.

Chapter 2. Impact of the cover

The antenna systems for mobile handsets usually face a complicated electromagnetic environment within the phone housing. Such an issue becomes even more critical when the operating frequency shifts up to the mm-wave band, so the impact of high permittivity and metallic materials used for the phone cover on the mm-wave antenna radiation, cannot be disregarded. Therefore, the impact of the integration into the phone has to be evaluated and optimized for mobile antenna systems.

In this chapter, some basic theory about the electromagnetic wave propagation through a dielectric layer will be firstly reviewed, and then the impact from different material of phone covers on the propagation of mm-wave antennas will be evaluated. In the end, solutions to mitigate the phone cover impact will be presented.

2.1 Transmission through back cover

Nowadays, a handset rear cover can be made of a variety of materials, such as plastic, glass, or metal. The distinct electromagnetic properties of each material affect the impinging waves differently. For that reason, in order to operate in mm-wave bands, the impact of different materials on the wave propagation needs to be studied.

An electromagnetic wave impinging upon another medium with different electrical properties is partially reflected and partially transmitted. The Fresnel reflection coefficient (Γ) provides the relation between the reflected and incident waves. It depends on the material properties, wave polarization and angle of incidence.

2.1.1 Reflection and transmission from dielectrics

For lossy dielectric materials, part of the power will be absorbed and its dielectric constant can be written as

$$\epsilon = \epsilon_0 \epsilon_r - j\epsilon'', \tag{2.1}$$

where $\epsilon_0 = 8.85 \times 10^{-12}$ and

$$\epsilon'' = \frac{\sigma}{2\pi f}, \tag{2.2}$$

with σ (Siemens/m) the conductivity of the material. If the material is a good conductor $\left(f < \frac{\sigma}{\epsilon_0 \epsilon_r}\right)$, the terms ϵ_r and σ are insensitive to the operating frequency.

Depending on the polarization of the impinging field (see Fig. 2.1), the reflection coefficients at the boundary of two dielectrics are given by [1]

$$\Gamma_{\parallel} = \frac{E_r}{E_i} = \frac{\eta_2 \sin\theta_t - \eta_1 \sin\theta_i}{\eta_2 \sin\theta_t + \eta_1 \sin\theta_i} \quad \text{(E-field parallel to plane of incidence)} \tag{2.3}$$

$$\Gamma_{\perp} = \frac{E_r}{E_i} = \frac{\eta_2 \sin\theta_i - \eta_1 \sin\theta_t}{\eta_2 \sin\theta_i + \eta_1 \sin\theta_t} \text{ (E-field perpendicular to plane of incidence)}, \tag{2.4}$$

with η_j the intrinsic impedance of each medium, which is given by $\sqrt{\mu_j/\epsilon_j}$. The subscripts i, r, t refer to the incident, reflected and transmitted fields, respectively.

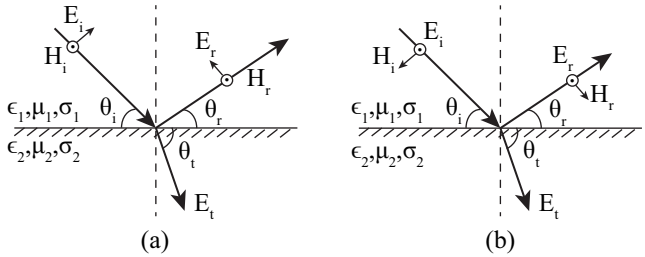

Fig. 2.1: Geometry to calculate the reflection coefficients between two dielectrics, re-plotted from [1]. (a) E-field parallel to the plane of incidence. (b) E-field perpendicular to the plane of incidence.

The Brewster angle (θ_B) is the angle of incidence at which the field is perfectly transmitted through a dielectric surface, i.e. there is no reflection. It can be obtained from

$$\sin\theta_B = \sqrt{\frac{\epsilon_1}{\epsilon_1 + \epsilon_2}}. \tag{2.5}$$

It is important to note that the Brewster angle only occurs for the E-field that is parallel to the plane of incidence.

Assuming that an electromagnetic wave is impinging from the air into a dielectric with relative permittivity ϵ_r, the reflection coefficients of different values of ϵ_r are presented in Fig. 2.2 according to the angle of incidence, with air as the first medium and $\mu_1 = \mu_2$. When $\Gamma = 0$, there is no reflected wave, which means that the power will be fully transmitted. The reflection coefficient in the parallel polarization case is similar for relatively small incident angles. However, a significantly reduced reflection coefficient can be obtained once the incident angle is above the Brewster angle for the lower permittivities. On the other hand, lower permittivity values always provide less reflection for the perpendicular polarization case, and the difference in the reflection between different permittivities is also enlarged when the angle of incidence increases. Among the common choices of the phone back cover materials (e.g. plastic, glass, ceramic, etc.), a plastic-based phone cover typically shows a relatively lower permittivity. Therefore, the transmission of mm-wave signals is expected to be better for the plastic-based rear cover than others.

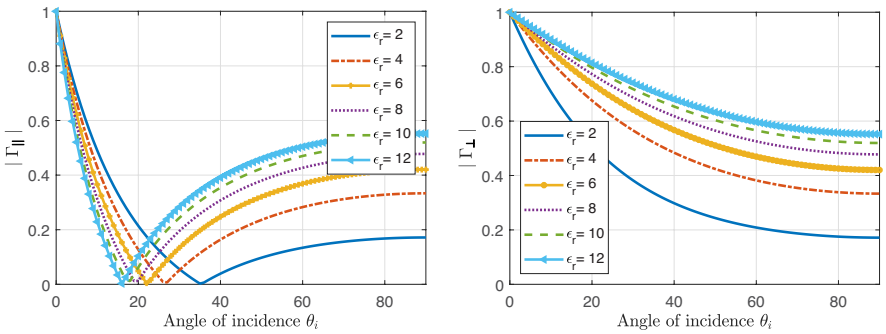

Fig. 2.2: Magnitude of the reflection coefficients as a function of the angle of incidence. (a) Parallel polarization. (b) Perpendicular polarization.

2.2 Evaluation of the cover impact from full wave simulation

The analytical Fresnel reflection coefficient can provide an intuitive picture on how different materials of the phone back cover can impact the transmission of mm-wave signals. However, to quantify the impact of the cover in a more realistic environment, full-wave simulations with an antenna inside the phone

chassis have been carried out as part of this dissertation.

In the simulation model depicted in Fig. 2.3, the mm-wave antenna has been placed in the top right corner, 1 mm away from the rear cover of the handset. The mm-wave antenna corresponds to two stacked dual-fed microstrip patch antennas, designed to cover the bands at 28 GHz and at 38 GHz. The reason for studying a dual-fed antenna is to evaluate if there is a difference in the behavior of two diferent polarizations. For the purpose of illustrating the impact of a rear cover on the mm-wave antenna radiation, only a single antenna element is considered here instead of an antenna array. Several components have been included, e.g., the display, the PCB, a frame and the battery, as presented in Fig. 2.3.

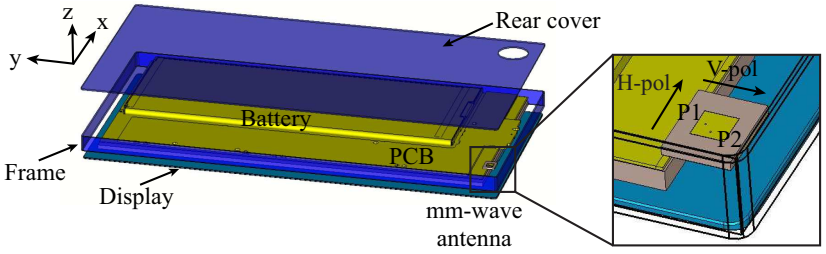

Fig. 2.3: Simulated model for the rear cover study. The left part of the figure is exploded in the z axis, while the zoomed view corresponds to the normal, non-exploded view. The distance between the antenna and the rear cover is 1 mm.

In this study, different rear cover materials have been simulated, i.e., plastic, glass and metal. The thickness of the rear cover is set to be 0.5 mm for all the models. For the plastic and metallic rear covers, a plastic frame is also included. The chosen plastic has a relative permittivity of 3 and $\tan\delta = 0.005$. The chosen metal is copper, with an electrical conductivity of 5.96×10^7 S/m. In the case of the glass rear cover, it incorporates a glass frame. The chosen glass type has $\epsilon_r = 6.84$, with loss tangent 0.0297. A reference case without a rear cover or frame is also provided.

Fig. 2.4 presents the reflection coefficient and radiation efficiency of the antenna with the different rear covers. In the reference case, where no rear cover or frame are included, the mm-wave patch antenna is matched from 28.04 GHz to 29.09 GHz and $36.23 - 37$ GHz for both polarizations with the -10 dB reflection coefficient criterion. The impedance match is slightly detuned when the antenna is covered by plastic, but the resonance frequency is barely shifted and the impedance bandwidth remains almost unmodified. In contrast, the glass back cover significantly influences the lower resonance of the antenna, decreasing the resonance frequency and increasing the mismatch to the port. On the other hand, the impact from the glass back cover on the higher resonance

is relatively low, which can be explained by the fact that the gap between the antenna and back cover is enlarged in terms of the wavelength. For the metallic cover, the antenna is matched at both resonances, but the lowest resonance has been shifted upwards in frequency, since it becomes more dependent on the gap between the antenna and the cover, rather than the antenna itself. In terms

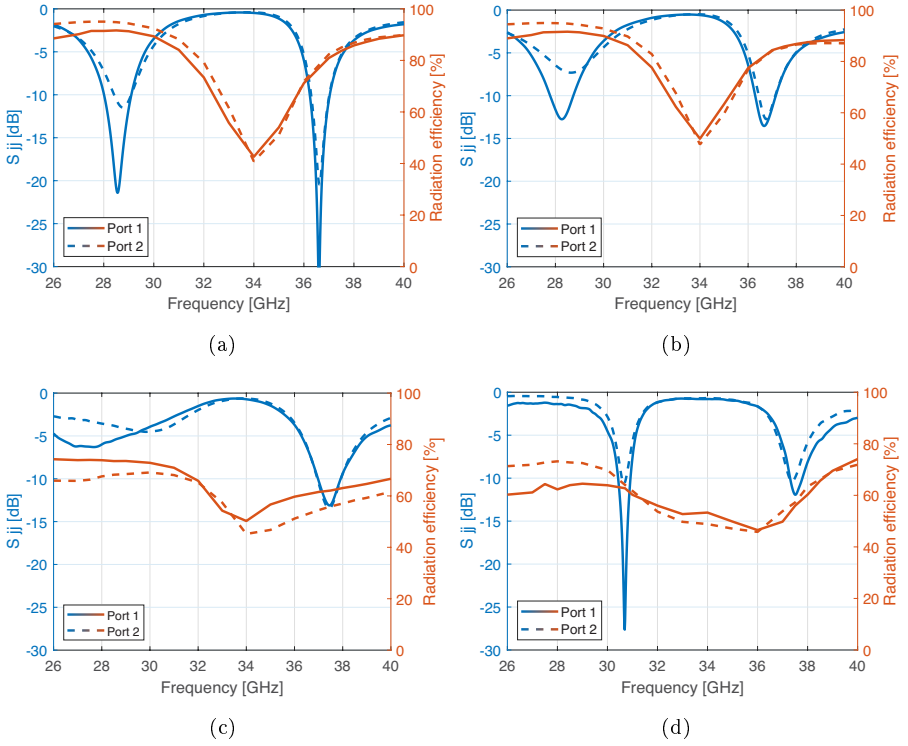

Fig. 2.4: Reflection coefficient and radiation efficiency comparison. (a) Uncovered. (b) Plastic rear cover. (c) Glass rear cover. (d) Metallic rear cover.

of radiation efficiency, which does not include the mismatch to the source, the results for the uncovered case and plastic cover are quite similar, with a value close to 90 % in both resonances, thanks to the low loss tangent in plastic. The radiation efficiency is slightly lower for the glass cover, reaching a value of almost 70 % in both resonances. The radiation efficiency levels of the metallic cover are similar to the glass cover.

In order to obtain a good spherical coverage, the gain and radiation pattern of a mm-wave antenna are critical as well. Therefore, the realized gain patterns at the first resonance of port 1, which correspond to the vertical polarization of the mm-wave antenna, are plotted and compared in Fig. 2.5. Once more,

thanks to the low tangent loss and permittivity of the plastic, the peak realized gain in the boresight direction and the shape of the radiation pattern are similar for the uncovered and the plastic cover cases. The gain of the glass rear cover is around 3 dB lower, as a consequence of the lower radiation efficiency and mismatch produced by surface waves on the glass. A stronger back lobe radiation shows that the reflection on the glass back cover is stronger than in the plastic cover. In addition, the ripples in the radiation pattern are more pronounced in the glass cover case compared to the plastic one. Finally, the metallic cover does not allow the antenna to radiate through, and the main lobe of the radiation pattern points towards the display of the phone model.

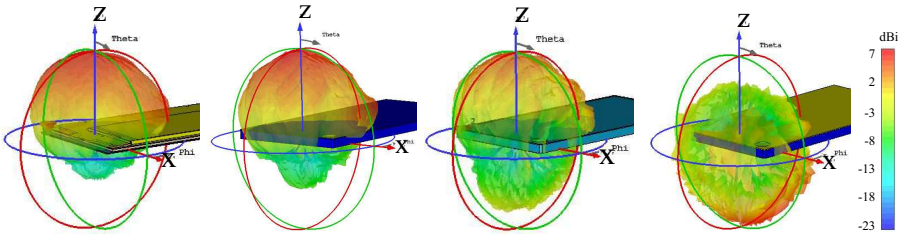

(a) f= 28.5 GHz (b) f= 28 GHz (c) f= 27 GHz (d) f= 30.7 GHz

Fig. 2.5: Realized gain port 1 (vertical polarization) comparison in the first resonance. (a) Uncovered. (b) Plastic rear cover. (c) Glass rear cover. (d) Metal rear cover.

The corresponding radiation patterns for the horizontal polarization are depicted in Fig. 2.6. The results are quite similar to the ones obtained with the vertical polarization, but with slightly less ripples. Therefore, the effect

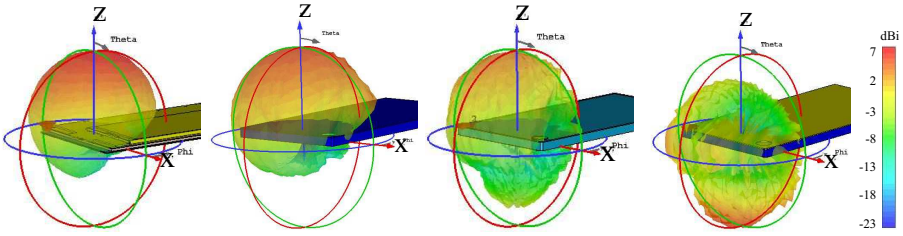

(a) f= 28.5 GHz (b) f= 28.5 GHz (c) f= 30 GHz (d) f= 30.7 GHz

Fig. 2.6: Realized gain port 2 (horizontal polarization) comparison in the first resonance. (a) Uncovered. (b) Plastic rear cover. (c) Glass rear cover. (d) Metal rear cover.

of the polarization is not significant when the cover is placed on top of the antenna. For the rest of this chapter, the focus will be only set in the horizontal polarization.

Surface waves are a source of ripples in the radiation pattern, resulting from the internal reflection of electromagnetic waves at the interface of two media with different dielectric constants. The intensity of surface waves decays as $1/\sqrt{r}$, since they have cylindrical wavefronts, unlike the radiated spherical waves that decay as $1/r$. Once a surface wave is launched by an antenna element on a large substrate, it reduces the radiation efficiency of the antenna. In an antenna array, the surface waves can also create undesired coupling between the antenna elements. If the substrate has a finite size, there will be diffractions from the substrate edges, that can increase the sidelobes and the cross-polarization levels and change the beam shape [2].

For any grounded dielectric sheet, with dielectric constant higher than 1 and thickness larger than 0 mm, at least one surface wave always exists. The TM_0 surface wave mode can always propagate since it has zero cutoff frequency. The cutoff frequency for higher order TM_n modes can be written as

$$f_c = \frac{nc}{2h\sqrt{\epsilon_r - 1}}, \quad n = 0, 1, 2... \tag{2.6}$$

where c is the speed of light and h the thickness of the substrate. For TE_n modes

$$f_c = \frac{(2n-1)c}{4h\sqrt{\epsilon_r - 1}}, \quad n = 1, 2, 3, ... \tag{2.7}$$

As the equation shows, the cutoff frequency for the higher order modes is inversely proportional to the permittivity and thickness of the substrate [3].

The electric field of the structures with dielectric cover has also been plotted in Fig. 2.7. It is possible to see how the surface wave propagates further in the glass cover, due to the higher relative permittivity, which distorts the radiation pattern more.

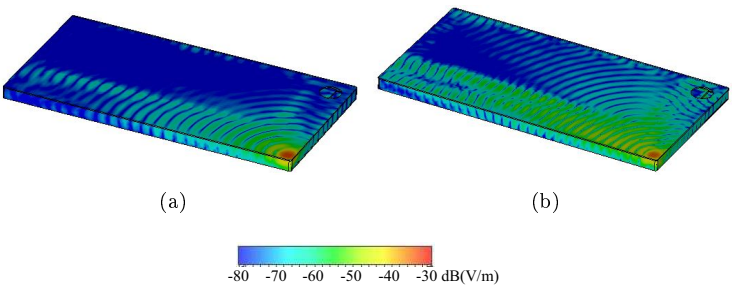

Fig. 2.7: Electric field comparison for the horizontal polarization with different dielectric materials. (a) Plastic rear cover. (b) Glass rear cover.

2.2.1 Influence of the antenna separation from the rear cover

The prior results showed a loss in the gain of around 3 dBi when the glass rear cover was employed. The separation of the antenna from the cover was 1 mm. In practice, the gap between the mm-wave antenna and rear cover can vary according to the industrial design of the phone housing. The impact of the separation of the antenna and cover is shown in Fig. 2.8 for different materials. Since the impact of rear cover on the two antenna ports is similar, as shown in the previous section, only port 2 (horizontal polarization) is considered here. A separation of 0 mm represents when the antenna is touching the cover. As a

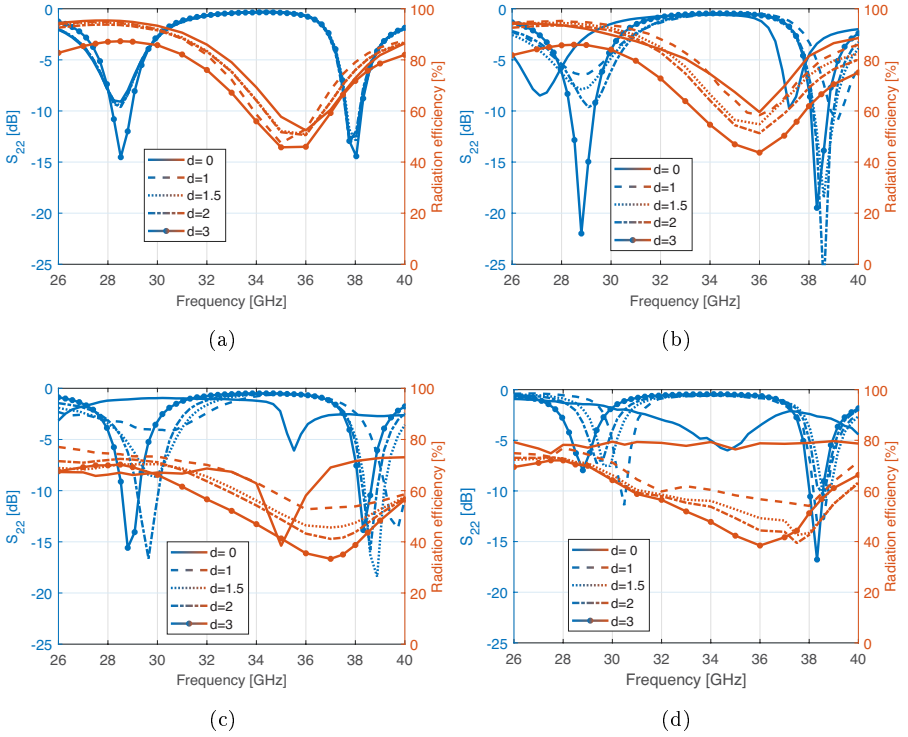

Fig. 2.8: Reflection coefficient and radiation efficiency in the desired direction comparison of port 2 (horizontal polarization) according to the distance to the rear cover. (a) No cover. (b) Plastic rear cover. (c) Glass rear cover. (d) Metal rear cover.

general observation, the closer the antenna is to the rear cover, the mismatch loss is more pronounced. This is particularly critical if the rear cover would be placed directly on the antenna surface ($d = 0$ mm). On the other hand, by separating the antenna from the cover by at least 1.5 mm (0.15λ in free

space at 30 GHz), the impact of rear cover on the antenna impedance match can be significantly reduced. The radiation efficiency curves show very similar performance of the antenna without a cover and the antenna with a plastic cover. For both the glass and metallic covers, the radiation efficiency has decreased around 20 %.

The $\Phi = 0°$ and $\Phi = 90°$ cuts of the radiation pattern for the horizontal polarization, have been plotted in Fig. 2.9 for two different antenna-cover separations. As a general observation, a larger separation to the rear cover provides results more similar to the free space scenario. Moreover, it is also worthy to point out that a larger gap between the rear cover and the mm-wave antenna does not necessarily lead to a higher antenna gain. For a given rear cover material, the achievable far-field radiation pattern is not only determined by the gap between the rear cover and the mm-wave antenna, but also the thickness of the rear cover. This behavior will be analyzed in the next section.

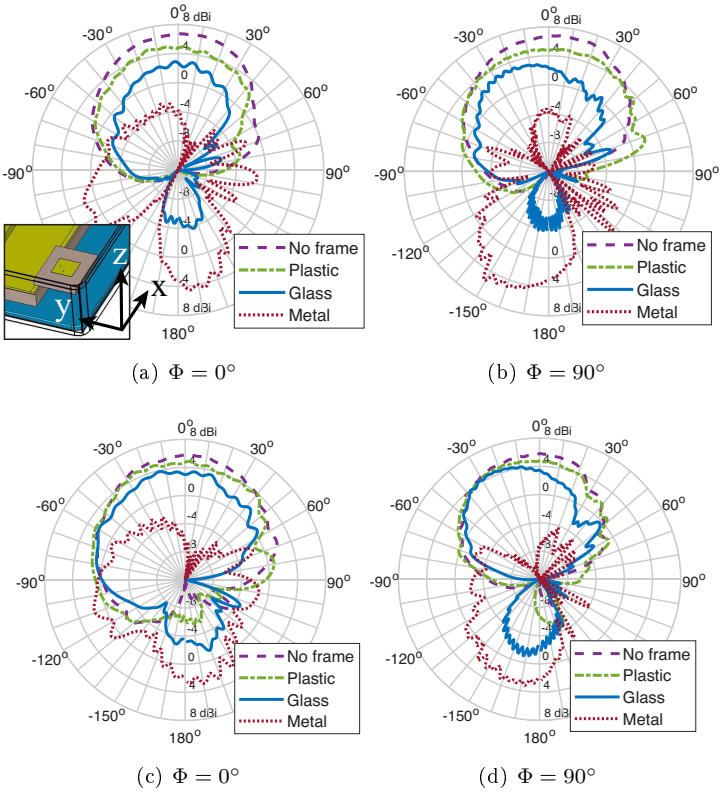

(a) $\Phi = 0°$ (b) $\Phi = 90°$

(c) $\Phi = 0°$ (d) $\Phi = 90°$

Fig. 2.9: Realized gain radiation patterns at the $\Phi = 0°$ and $\Phi = 90°$ cuts for the horizontal polarization, according to the distance to the rear cover. (a, b) d= 1 mm. (c, d) d= 3 mm.

2.2.2 Influence of the rear cover thickness

In addition to the antenna-rear cover separation distance, the cover thickness is also a critical factor that needs to be considered for an optimized mm-wave antenna performance. Assuming a glass rear cover is placed at a certain distance from the antenna, it can be considered as a dielectric slab between two media, where uniform plane waves impinge on the material interfaces. Consider the model shown in Fig. 2.10, where E_+ and E_- are the forward and backward propagating electric fields with respect to the interface. It is possible to obtain the reflection (Γ_1) from the overall transmission (T) responses into the last medium as a function of the slab thickness (h_1) [4]

$$\Gamma_1 = \frac{E_{1-}}{E_{1+}} = \frac{\rho_1 + \rho_2 e^{-2k_1 h_1}}{1 + \rho_1 \rho_2 e^{-2k_1 h_1}}, \tag{2.8}$$

$$T = \frac{E'_{2+}}{E_{1+}} = \frac{\tau_1 \tau_2 e^{-k_1 h_1}}{1 + \rho_1 \rho_2 e^{-2k_1 h_1}}, \tag{2.9}$$

where ρ_1, ρ_2 are the elementary reflection coefficients from the left sides of the two interfaces, and τ_1, τ_2 are the transmission coefficients. They are given by:

$$\rho_1 = \frac{\eta_1 - \eta_a}{\eta_1 + \eta_a}, \quad \rho_2 = \frac{\eta_b - \eta_1}{\eta_b + \eta_1}, \quad \tau_1 = 1 + \rho_1, \quad \tau_2 = 1 + \rho_2. \tag{2.10}$$

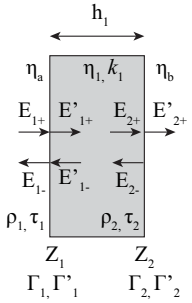

Fig. 2.10: Single dielectric slab between two media, re-plotted from [4]. The arrows indicate the direction of propagation, not the direction of the fields. The field vectors are perpendicular to the directions of propagation and parallel to the interface plane.

The above equations have been expanded in [4] to include oblique incidence. The transmission response has been plotted in Fig. 2.11 for different angles of incidence and thicknesses of the glass surface at 28.5 GHz. The parallel polarization has a better transmission for angles of incidence larger than 50°. For smaller angles, the transmission is quite similar for both polarizations. In addition, it can be observed that the transmission coefficient varies periodically with an increased thickness. Therefore, an optimized thickness of the rear cover

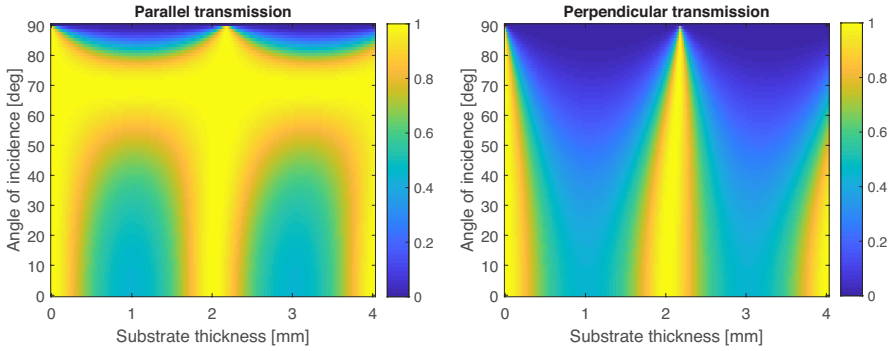

(a) (b)

Fig. 2.11: Transmission coefficient at 28.5 for a slab with $\epsilon_r = 6.84$. (a) Parallel polarization. (b) Perpendicular polarization.

can be found to obtain the best transmission performance for the integrated mm-wave antenna propagation.

The reflection coefficient Γ_1 into the medium with wave impedance η_a was given in equation (2.8). In order to obtain the maximum transmission, i.e., a slab with no reflection, $\rho_1 + \rho_2 e^{-2jk_1h_1}$ must be equal to zero. This requires

$$e^{2jk_1h_1} = -\frac{\rho_2}{\rho_1}. \tag{2.11}$$

This condition can be satisfied in two cases: $e^{2jk_1h_1} = \pm 1$. For the first case, $2jk_1h_1$ should be an integral multiple of 2π. This gives the half-wavelength condition $h_1 = n\lambda_1/2$, with n an integer and λ_1 the guided wavelength in the slab. Since the condition $\rho_2 = -\rho_1$ needs to be met as well, it is required that $\eta_a = \eta_b$. This means that the media at both sides of the slab need to be the same. The second case requires $2jk_1h_1$ to be an odd multiple of π, which gives $h_1 = (2n+1)\lambda_1/4$. Together with the second requirement, $\rho_2 = \rho_1$, the reflection zero will occur only if $\eta_1^2 = \eta_a\eta_b$. These results are also employed in the literature to obtain the optimum thickness of radomes [5].

Fig. 2.12 shows the reflection coefficient and radiation efficiency comparison of the antenna separated 1 mm from the glass cover, as a function of the glass thickness (h). As expected from the condition $h_1 = n\lambda_1/2$, a thickness of half-wavelength (2 mm at 28.5 GHz) is the one that provides the results most similar to the free space scenario. Thicknesses of 0.25 mm and below provide similar radiation efficiency to the antenna without a cover. Fig. 2.13 presents two cuts of the realized gain radiation patterns for different cover thicknesses. A 2 mm thickness cover provides the best transmission, with around 2 dBi higher gain than the 3 mm-thick solution.

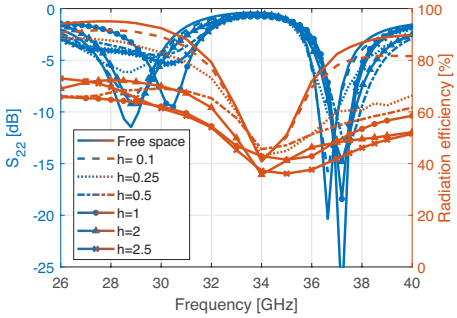

Fig. 2.12: Reflection coefficient and radiation efficiency comparison of port 2 according to the thickness of the glass rear cover. The antenna is separated 1 mm from the rear cover.

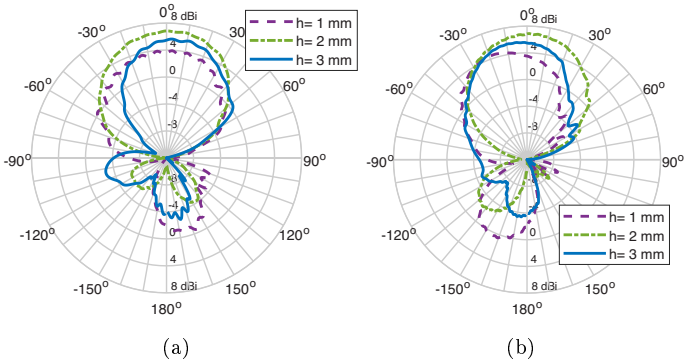

(a) (b)

Fig. 2.13: Realized gain radiation patterns of the horizontal polarization at the lower resonance according to the cover thickness. (a) $\Phi = 0°$ cut. (b) $\Phi = 90°$ cut.

To summarize the impact from the rear cover, it can be observed that the choice of back cover material shows a major impact on the antenna performance in the 5G mm-wave bands. For a dielectric rear cover, high permittivity and dielectric loss lead to a more significant antenna mismatch and radiation efficiency losses. Moreover, the surface waves on dielectric materials cause ripples in the radiation pattern, which are also more pronounced with a higher permittivity rear cover. Therefore, materials with low permittivity and low loss, e.g., plastic, offer an easier integration of the mm-wave antennas. On the other hand, a metallic back cover can change the mm-wave antenna radiation completely, since no electromagnetic wave can propagate through it. A more advanced design would be needed if a metal back cover would be used for mm-wave 5G mobile terminals.

For a given material, both the antenna separation to the rear cover and the thickness of the rear cover can affect the mm-wave antenna performance.

The impact of the antenna separation to the rear cover can be neglected as the distance increases. The optimum material thickness for maximum transmission is the one that corresponds to one half of the guided wavelength.

2.3 Methods to reduce the impact of the rear cover

As it can be observed from the study above, the glass rear cover can cause a significant degradation of the mm-wave antenna radiation due to its high permittivity and high loss. This can be detrimental especially for handsets that have both front and back covers made of glass. Moreover, it is important to find methods to reduce the impact of the glass covers even if just one of the covers (front or rear) is glass.

A method to reduce the impact of the rear cover consists of improving the transmission in the glass by printing metasurfaces on it of a certain area. In [6] a frequency selective surface (FSS) with a circular loop design is printed between two layers of glass with permittivity 9, which form the rear cover, to achieve a reflection lower than -10 dB for certain angles of incidence. The model is depicted in Fig. 2.14. The transmission of the glass alone has a value of -5.3 dB, which means that less than 30 % of the radiated power is transmitted through the glass, while the transmission for the structure with the FSS design is practically 0 dB at the frequency of design. The radiation pattern of the

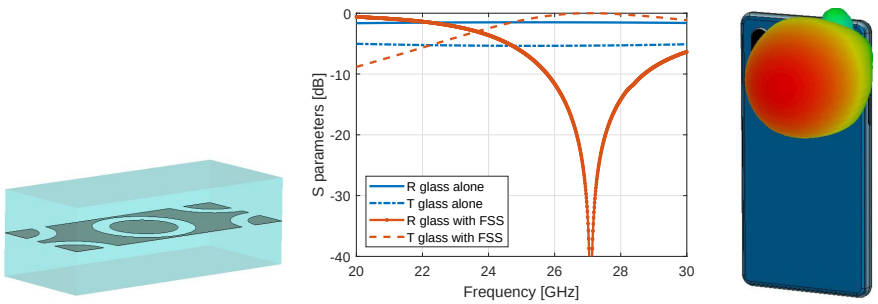

(a) (b) (c)

Fig. 2.14: (a) Simulated FSS unit cell model between two layers of glass reproduced from [6]. The substrate has $\epsilon_r = 9$. (b) Reflection (R) and transmission (T) comparison of the glass alone and the glass with the FSS design for an angle of incidence 30°. (c) Resulting radiation pattern of the FSS integrated in the phone from [6], using a region of 13×15 mm^2 made of unit cells in the rear cover.

mm-wave antenna with the FSS in the phone rear cover is presented in Fig.

2.14(c). No ripples can be visualized in the radiation pattern, due to the good transmission behaviour of the FSS.

In [6] a local lens is also proposed in the glass back cover (Fig. 2.15). The thickness of the lens covering the antenna aperture was chosen to be half-wavelength to provide the maximum transmission. Even though the antenna impedance match and efficiency are improved with a thicker glass, the radiation pattern is still distorted by ripples produced by the propagation of surface waves inside the dielectric cover.

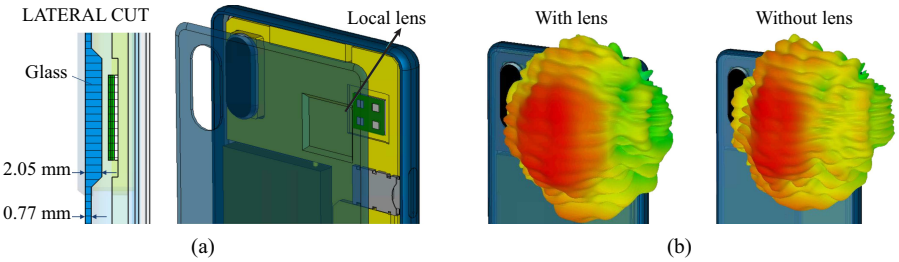

Fig. 2.15: (a) Model proposed in [6] of the local thickening of the glass rear cover. (b) Radiation patterns with and without lens from [6].

To suppress the propagation of surface waves induced by the glass back cover, metasurfaces, which can operate as a bandstop structure, can be adopted. These metasurfaces could be printed around the radiating aperture of the antenna. An example with split-ring resonators (SRRs) printed on top of the glass cover was developed in this thesis. The surface current of the design with and without SRR is shown in Fig. 2.16. The SRR is able to considerably reduce the propagation of surface waves. When the radiation pattern is plotted, the proposed design yields a single-beam radiation pattern (Fig. 2.17(b)), while the antenna without SRRs has several high-gain lobes. Moreover, the gain is increased 4 dB with respect to the model with only glass cover.

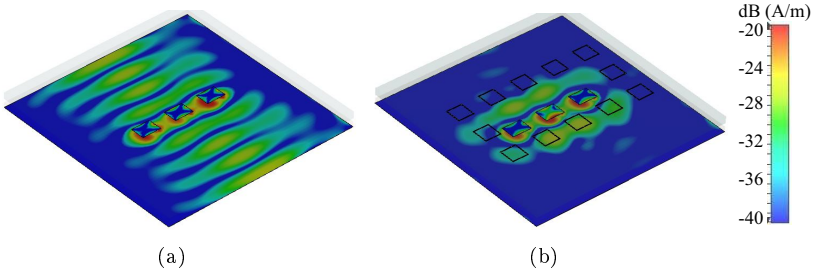

Fig. 2.16: Surface current of the mm-wave microstrip patch array covered by a glass layer. (a) Without SRR. (b) With SRR.

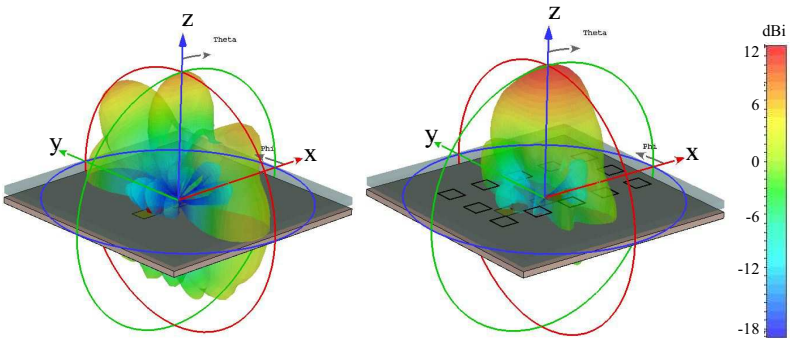

(a) (b)

Fig. 2.17: Realized gain radiation patterns of the microstrip patch array with glass cover. (a) Without SRR. (b) With SRR.

Though the glass covers can cause severe performance degradation for the integrated mm-wave antennas, it is possible to have more complicated electromagnetic designs on the glass with evolving processing technologies [7]. As an example, antennas-on-display are becoming more popular nowadays, due to the lack of available space in phones [8–11]. However, the surface waves not only are excited when the glass cover is on top of the antenna, but also when the antenna uses the glass as a substrate. Paper A [12] proposes to print two rows of parasitic radiators next to the mm-wave antenna-on-display to reduce the surface waves propagation. The operating principle is presented in Fig. 2.18. The radiation of the mm-wave array printed on a glass substrate, facilitates the propagation of evanescent fields in the substrate, causing ripples and sidelobes in the radiation pattern [13]. These effects are illustrated in Fig. 2.19(a) and Fig. 2.20(a). The parasitic radiators are fed by the surface waves and this energy is radiated. This emission reduces the ripples in the radiation pattern, as can be seen in Fig. 2.20(b).

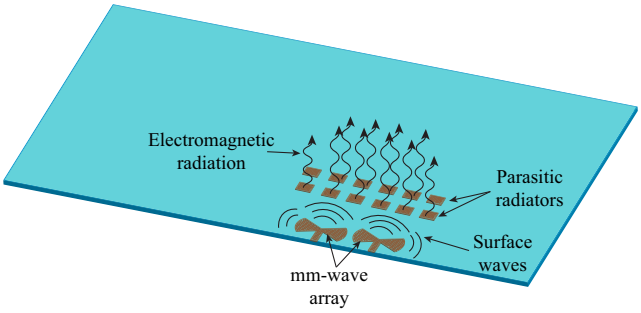

Fig. 2.18: Model proposed in Paper A [12] to reduce the surface waves propagation.

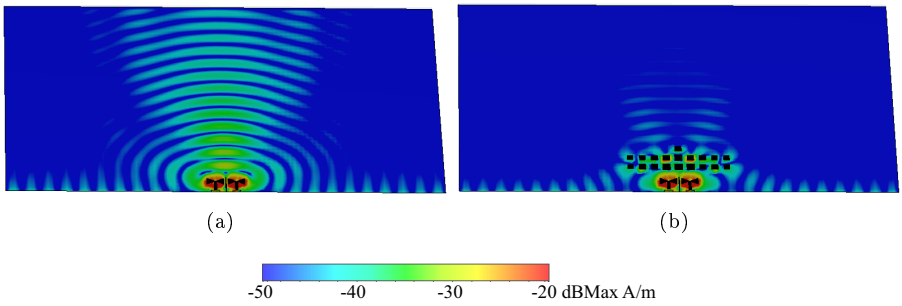

Fig. 2.19: Surface currents at 28 GHz from [12]. (a) Without parasitic radiators. (b) With parasitic radiators.

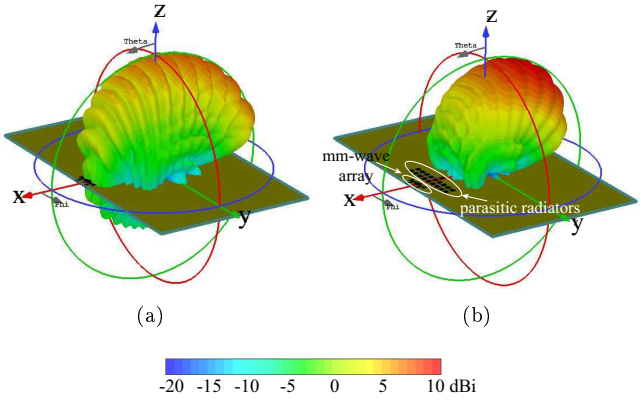

Fig. 2.20: 3D realized gain radiation pattern from [12]. (a) Antenna array without parasitic radiators. (b) Antenna array with the parasitic radiators to reduce the surface waves.

2.4 Summary

The impact from the phone rear cover on the surface-mounted mm-wave antennas has been studied in this chapter. In particular, dielectric back covers can be a feasible choice from the mm-wave antenna integration point of view, as it allows the antennas to radiate through the phone housing. However, the selected material for the dielectric back cover is still critical to the 5G mm-wave antenna system's performance. An increased permittivity and tangent loss of the back cover material can result in a more severe antenna impedance mismatch and efficiency drop. In addition, a high permittivity dielectric also sustains the propagation of the surface wave in mm-wave frequency bands, that distorts the antenna radiation pattern. Moreover, the characteristics of the back cover,

including the cover thickness and antenna to cover distance, also show an impact that cannot be disregarded, and thus, need to be optimized according to operating frequencies of the antennas.

Several methods to improve the transmission through glass covers have also been proposed. In order to improve the transmission of high-dielectric materials, it is necessary to print some structures in the dielectric to modify its electromagnetic behavior. In this chapter, a design with split-ring resonators that contains the surface waves and a design that radiates the energy from the surface waves are proposed.

References

[1] T. S. Rappaport *et al.*, *Wireless communications: principles and practice*. Prentice hall PTR New Jersey, 1996, vol. 2.

[2] D. Pozar, "Considerations for millimeter wave printed antennas," *IEEE Transactions on Antennas and Propagation*, vol. 31, no. 5, pp. 740–747, 1983.

[3] D. M. Pozar, *Microwave engineering*. John wiley & sons, 2009.

[4] S. J. Orfanidis, *Electromagnetic waves and antennas*, 2016.

[5] J. Volakis, R. Johnson, and H. Jasik, *Antenna Engineering Handbook, Fourth Edition*, ser. McGraw-Hill's AccessEngineering. McGraw-Hill Education, 2007.

[6] R. K. Enjiu and M. Rütschlin, "Design of 5G mm-wave compatible covers for high end mobile phones," in *Proceedings of NAFEMS World Congress 2019*, 2019.

[7] A. B. Shorey and R. Lu, "Progress and application of through glass via (TGV) technology," in *2016 Pan Pacific Microelectronics Symposium (Pan Pacific)*. IEEE, 2016, pp. 1–6.

[8] W. Hong, J. Choi, D. Park, M.-s. Kim, C. You, D. Jung, and J. Park, "mmWave 5G NR cellular handset prototype featuring optically invisible beamforming antenna-on-display," *IEEE Communications Magazine*, vol. 58, no. 8, pp. 54–60, 2020.

[9] J. Park, S. Y. Lee, Y. Kim, J. Lee, and W. Hong, "Hybrid antenna module concept for 28 GHz 5G beamsteering cellular devices," in *2018 IEEE MTT-S International Microwave Workshop Series on 5G Hardware and System Technologies (IMWS-5G)*, 2018, pp. 1–3.

[10] J. Park and W. Hong, "Antenna-on-display (AoD) for millimeter-wave 5G mobile devices," in *2019 IEEE International Symposium on Antennas and Propagation and USNC-URSI Radio Science Meeting*, 2019, pp. 603–604.

[11] J. Park, S. Y. Lee, J. Kim, D. Park, W. Choi, and W. Hong, "An optically invisible antenna-on-display concept for millimeter-wave 5G cellular devices," *IEEE Transactions on Antennas and Propagation*, vol. 67, no. 5, pp. 2942–2952, 2019.

[12] R. Rodríguez-Cano, S. Zhang, and G. F. Pedersen, "Transparent mm-wave array on a glass substrate with surface wave reduction," in *2020 14th European Conference on Antennas and Propagation (EuCAP)*, 2020, pp. 1–4.

[13] B. Xu, Z. Ying, L. Scialacqua, A. Scannavini, L. J. Foged, T. Bolin, K. Zhao, S. He, and M. Gustafsson, "Radiation performance analysis of 28 GHz antennas integrated in 5G mobile terminal housing," *IEEE Access*, vol. 6, pp. 48 088–48 101, 2018.

Chapter 3. Impact of the frame

The impact from the phone cover, especially the rear cover, has been analyzed in Chapter 2. As another important piece of a mobile phone today, the impact of different phone frames on the antenna performance will be assessed. The chapter is organized in a similar structure as the previous one: the impact of different frame materials on the mm-wave antenna performance will be studied first. The placement of the antenna array with respect to the frame and the effect of the frame width are also presented. Finally, different methods to reduce the metallic frame obstruction to the radiation of mm-wave antenna arrays are proposed.

3.1 Evaluation of the frame material

The use of endfire antennas is a popular choice in mm-wave mobile handset applications [1–12], since they can provide decent spherical coverage [13], as analyzed in Sections 1.3 and 1.4. However, this implies that the mm-wave antenna array will radiate towards the phone frame, and thus, the impact of the frame becomes critical to the mm-wave antenna performance. More importantly, the metallic frame has been predominant in the high-end smartphones today, but the electromagnetic waves cannot pierce through a good conductor. Therefore, understanding the behavior of endfire mm-wave radiation emitted towards the phone frame becomes crucial.

In order to assess the influence of the frame on the mm-wave antenna radiation, the same dual-polarized patch antenna from the previous chapter has been adopted for evaluation. The antenna plane was set parallel to the frame, and therefore, the antenna would radiate towards the frame. The simulation model is shown in Fig. 3.1. The antenna-frame separation distance is set to 1.5 mm and the frame width to 5.2 mm. The different cases that have been assessed are: no frame with plastic rear cover, plastic frame and rear cover, glass frame and rear cover, and finally, metallic frame and plastic rear cover. For convenience, the desired direction of radiation of the mm-wave antenna men-

tioned throughout this chapter is the $+z$ axis (the coordinates are depicted in Fig. 3.1).

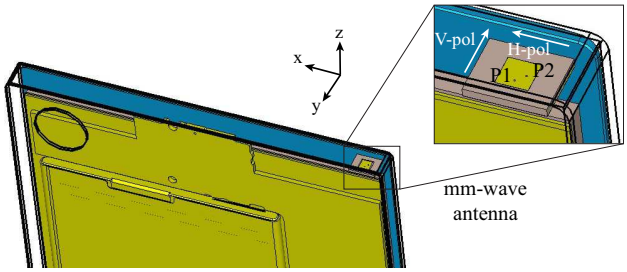

Fig. 3.1: Simulated model for the frame case study. The distance between the antenna and the frame is 1.5 mm. Port 1 excites the vertical polarization and port 2, the horizontal.

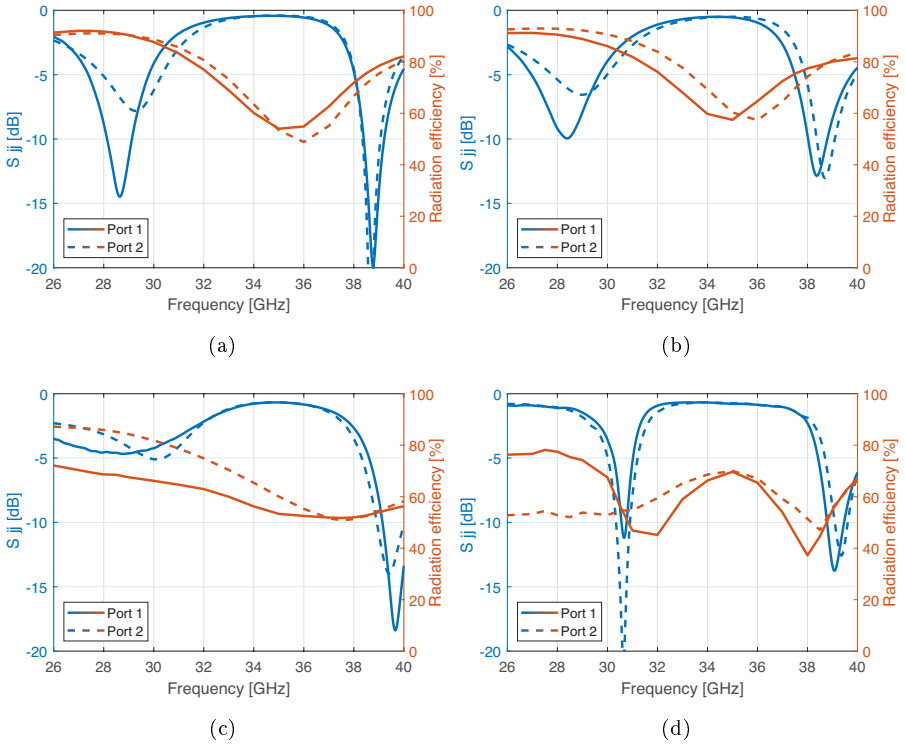

Fig. 3.2: Reflection coefficient and radiation efficiency comparison. (a) No frame with plastic rear cover. (b) Plastic frame and plastic rear cover. (c) Glass frame and glass rear cover. (d) Metallic frame and plastic rear cover.

The S parameters and radiation efficiency of the different frame materials are compared in Fig. 3.2. The reflection coefficient of the mm-wave antenna

without the frame is matched to the source for port 1 from $28.14 - 29.12$ GHz and $38.34 - 39.2$ GHz, while port 2 covers similar frequency bands but with slightly poorer impedance match at the lower resonance frequency. The radiation efficiency of the antenna without a frame at the first and second resonances is around 90 % and 80 %, respectively. Fig. 3.2 (b) shows that covering the antenna with a plastic frame does not change much the results. Similar to the impact from the plastic rear cover from Section 2.2, the plastic frame also shows a minimum impact on the antenna impedance match and radiation efficiency, while the glass frame severely changes the antenna impedance match and the radiation efficiency. On the other hand, a more significant difference can be seen between the two polarizations, which opposes the phone rear cover results. For the case of the metallic frame, the resonance frequency of the antenna is shifted to a higher frequency for the first resonance, and a significant difference between the radiation efficiency of the two antenna ports can be observed.

Fig. 3.3 presents the realized gain radiation patterns of port 1 (vertical polarization) of the different simulated models. It can be seen that the plastic frame provokes an insignificant impact on the antenna radiation, while the glass frame reduces the gain about 3 dB due to the lower antenna efficiency and also leads to more observable ripples on the radiation pattern. In both cases, the antenna can radiate towards the +z direction, which is the same as in the case without a frame. However, for the metallic frame case, the main beam is not pointing in the direction of the $+z$ axis, but to the lower hemisphere, and only a small portion of power can still radiate towards the desired direction ($+z$).

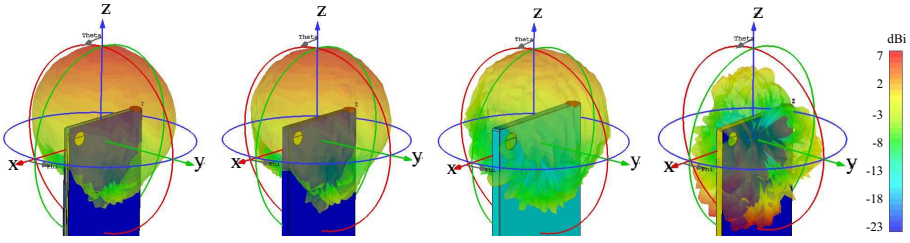

(a) f= 28.5 GHz (b) f= 28.5 GHz (c) f= 28.5 GHz (d) f= 30.5 GHz

Fig. 3.3: Realized gain port 1 (vertical polarization) comparison. (a) No frame with plastic rear cover. (b) Plastic frame and plastic rear cover. (c) Glass frame and glass rear cover. (d) Metallic frame and plastic rear cover.

The radiation patterns of port 2 (horizontal polarization) are depicted in Fig. 3.4. Comparing to the vertical polarization, the surface waves impact, in terms of ripples, in the radiation pattern on both plastic and glass frame is less noticeable. On the other hand, the blockage effect from the frame becomes even more pronounced, comparing to the case with the vertically-polarized port, for

the metallic frame. The antenna gain in the $+z$ direction is reduced from 0 dBi with the vertically-polarized wave to -6 dBi with the horizontally-polarized wave.

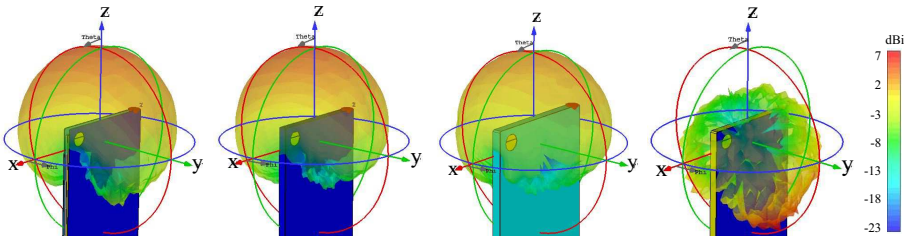

(a) f= 29 GHz (b) f= 29 GHz (c) f= 30 GHz (d) f= 30.5 GHz

Fig. 3.4: Realized gain port 2 (horizontal polarization) comparison. (a) No frame with plastic rear cover. (b) Plastic frame and plastic rear cover. (c) Glass frame and glass rear cover. (d) Metallic frame and plastic rear cover.

The average electric-field amplitude was also obtained for the frame solutions and it is shown in Fig. 3.5. As it happened with the rear cover, the plastic facilitates more emission of the electric field in the desired direction than in the glass case. Fig. 3.5(c) shows how the surface waves propagate further in the glass solution. In the case of the metallic frame, there is a null in the $+z$ direction and the energy is reflected by the metallic frame and propagates throught the front and rear cover into the free space.

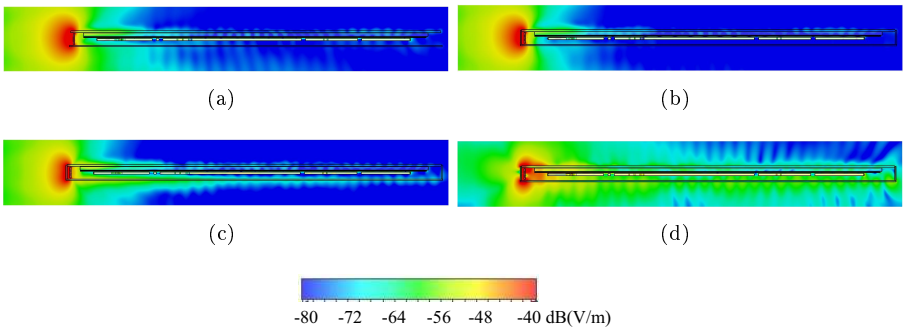

Fig. 3.5: Averaged electric field over one period of the horizontal polarization in the YZ cut. In this cut, the phone is sitting on its rear cover. (a) No frame with plastic rear cover. (b) Plastic frame and rear cover. (c) Glass frame and rear cover. (d) Metallic frame with plastic rear cover.

To achieve good spherical coverage in 5G mm-wave mobile devices, multiple mm-wave arrays that yield radiation patterns pointing towards different direc-

tions are needed. However, the results here have shown that the metallic frame alters the radiation direction of the mm-wave antennas, which will further impact on the device's spherical coverage. Therefore, an in-depth study on the effect of metallic frame on the radiation of mm-wave antennas, and solutions to reduce the corresponding effects, would be needed.

3.1.1 Influence of the antenna-metallic frame separation

The effect of metallic frame on the device integrated mm-wave antennas is further presented in this section with a parametric study of antenna-frame separation distance. The results of the antenna impedance match and radiation efficiency are shown in Fig. 3.6, where the antenna separation distance varies from 0.5 mm to 3 mm. The results without a frame have also been given as reference value. The horizontally-polarized antenna (port 2) is taken as an example to be studied here, as it affects the radiation more severely compared to vertically-polarized antenna port, according to the results above. It can be observed that a significant antenna impedance mismatch would be caused if the mm-wave antenna is placed 0.5 mm away from the metallic frame. The resonance frequency of the metallic frame depends also on the separation gap between the antenna and the metallic frame, with smaller separation distances providing higher resonance values. Moreover, the radiation efficiency has decreased around 30 % at the lower resonance.

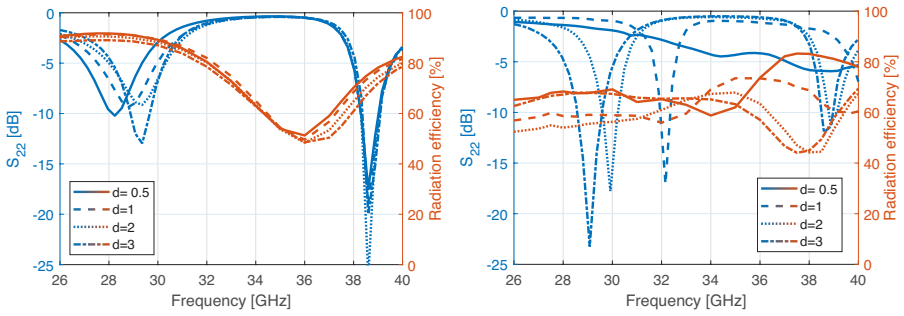

Fig. 3.6: Reflection coefficient and radiation efficiency of the horizontally-polarized antenna (port 2) according to the distance to the frame. (a) No frame and plastic rear cover. (b) Metallic frame with plastic rear cover.

The radiation pattern $\Phi = 0°$ and $\Phi = 90°$ cuts of the horizontal polarization are plotted in Fig. 3.7 for two different antenna-frame separations. It can be observed that enlarging the antenna-frame distance can marginally improve the antenna gain towards the desired direction ($+z$ axis), but the main beam

is still pointing towards the lower hemisphere.

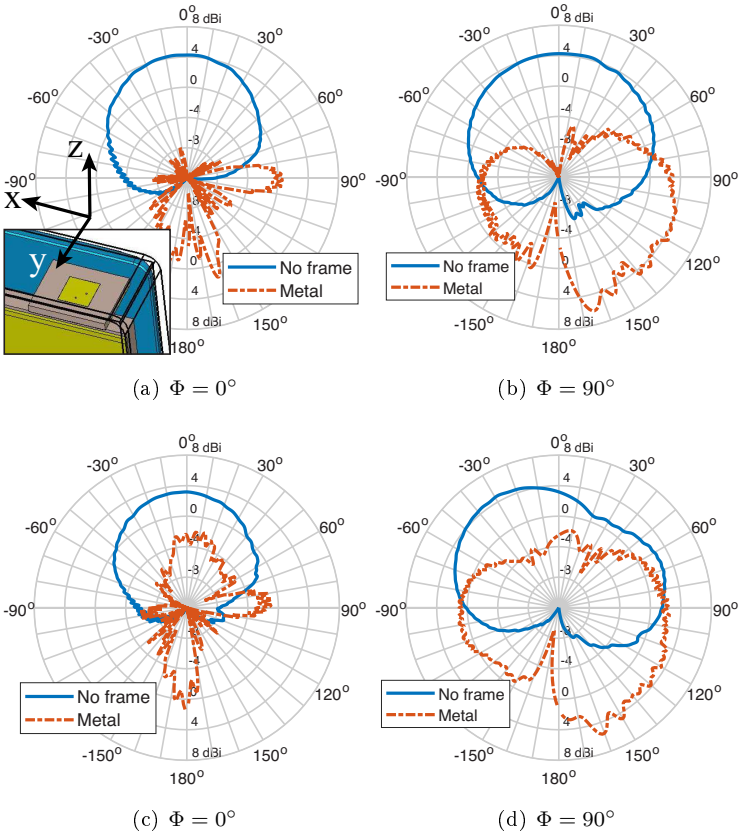

(a) $\Phi = 0°$ (b) $\Phi = 90°$

(c) $\Phi = 0°$ (d) $\Phi = 90°$

Fig. 3.7: Realized gain radiation patterns at the $\Phi = 0°$ and $\Phi = 90°$ cuts according to the distance to the frame for horizontal polarization. (a, b) d= 1 mm. (c, d) d= 3 mm.

3.1.2 Influence of the metallic frame width

In addition to the distance between the antenna and the frame, the width of the metallic frame has a strong impact on the radiation pattern of the antenna as well, and it is necessary to study the antenna performance with different frame widths. Unlike in the previous sections, the antenna in this model is not placed in the top corner of the phone, but in the top center to avoid any effects from the corners of the frame. The antenna-frame separation is set to 2 mm. Fig. 3.8 presents the realized gain radiation patterns for three different metallic frame widths, i.e., 3 mm, 5 mm and 7 mm, for both polarizations. A reference case without the top frame has also been included. It can be seen

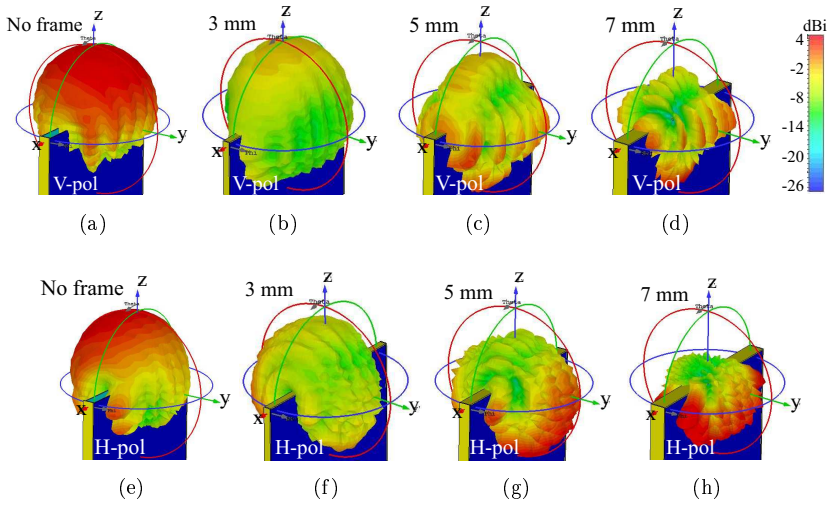

Fig. 3.8: Realized gain radiation patterns. The first row corresponds to vertical polarization, while the second, to horizontal polarization. The figures present different frame widths: (a, e) No top frame. (b, f) 3 mm. (c, g) 5 mm. (d, h) 7 mm.

that the radiation pattern, especially the radiation towards the $+z$ direction, is highly dependent on the polarization of the mm-wave antenna. An increment in the width value can be especially detrimental for the horizontal polarization. On the other hand, a frame width of below 5 mm still allows radiation in the broadside direction for vertical polarization, but the backlobe and sidelobes are considerably larger.

As a summary, the use of metal is much more detrimental than dielectric frames, since it changes the direction of the radiation. To obtain an optimized antenna performance, it is preferred to design the mm-wave antennas in the presence of the frame structure of the selected material. In order to avoid a large antenna impedance mismatch loss in the presence of a frame, it is necessary to place it at an acceptable distance away from the frame. In the case of a metallic frame, electromagnetic radiation cannot pierce through the frame, and significant changes in the antenna radiation pattern can be caused, especially by a wider frame width. It has also been observed that the impact of a metallic frame on the antenna radiation is polarization-dependent, where vertical polarization is less perceptive to the metallic frame than horizontal polarization. To obtain radiation in the desired direction, modifications or perforations need to be made in the frame. In the next section, several methods are proposed to diminish the obstruction of metallic frames to the radiation emitted by horizontally-polarized mm-wave antennas.

3.2 Methods to reduce the metallic frame blockage

As shown in the previous section, having a mm-wave antenna radiating towards a metallic frame requires the co-design of the antenna and the frame to obtain the desired radiation direction of the mm-wave antenna. As mentioned in Chapter 1, such a co-design would not only require an optimization in the mm-wave bands, but also taking into account the impact on the antenna system in sub-7 GHz, since the phone frame is typically employed as a sub-7 GHz antenna. Several solutions have been proposed in the literature where either a window is cut in the metallic frame (Fig. 3.9(a)) for the mm-wave module [14] or slots are etched on the frame [15–18]. Nevertheless, it would be interesting to be able to place the mm-wave antenna arrays in the vicinity of the frame, without cutting large windows or modifying the current distribution in the frame.

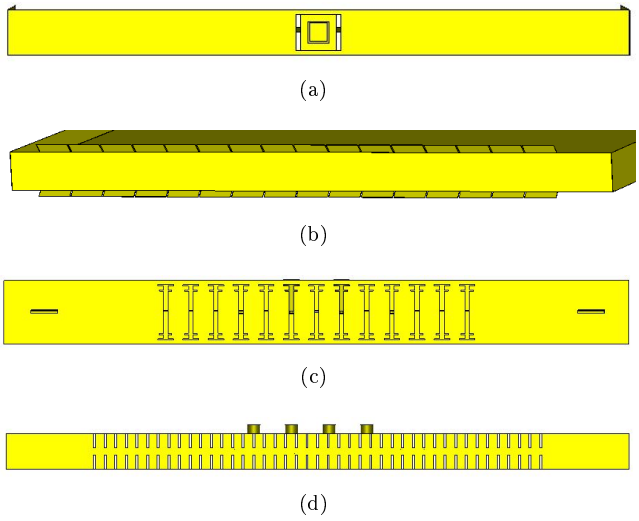

Fig. 3.9: Proposed methods. (a) Front view of the window etched in Kurvinen *et al.* [14]. (b) Front view of the parasitic layers from Paper B. (c) Front view of the slotted frame from Paper C. (d) Front view of the hard surface inspired frame from Paper D.

Papers B [10], C [11], and D [12], included in this dissertation, propose three different methods to ensure that the boresight direction of the mm-wave antenna with a metallic frame is the desired one ($+z$ direction). They are presented in Figs. 3.9(b-d). Moreover, the blockage from the frame is considerably reduced. A short comparison among them will be given in this section.

Paper B proposes two parasitic layers to be placed at both sides of the

frame, which help re-radiate the energy of the mm-wave antenna in the desired direction, as shown in Fig. 3.10.

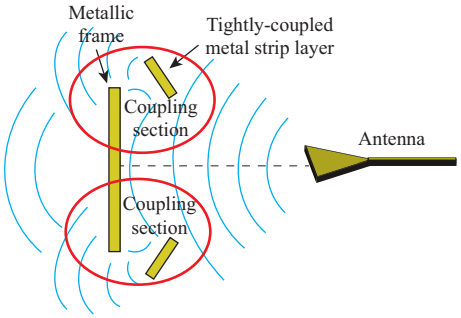

Fig. 3.10: Operating mechanism of paper B.

The parasitic layers are composed of numerous strips. For the design of the parasitic layers, there are several parameters to take into account. The tilting angle of the parasitic layers does not have a huge impact on the array gain, as long as the layers are not parallel to the frame. The gap between the strips and their length are sensitive parameters for the array gain. To achieve maximum gain, the parameter values must be $0.013\lambda_0$ and $0.2\lambda_0$ for the gap and length, respectively. The performance of the mm-wave array can improve if the array-frame separation is around $0.6\lambda_0$. The mm-wave array was co-designed together with a sub-7 GHz frame antenna. The strip layers did not change the performance of the frame antenna.

Paper C embeds a slot array on the frame, which can be understood as being fed by the integrated mm-wave antenna array through the coupling. This way, the radiation emitted by the mm-wave array passes through the frame, as shown in Fig. 3.11. Unlike the solution proposed in Paper B, the gain of the mm-wave

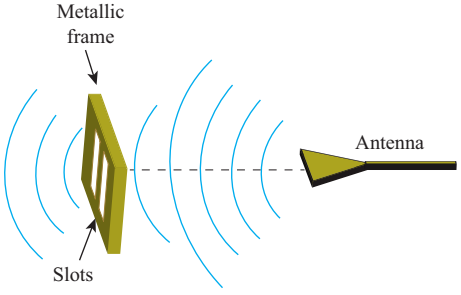

Fig. 3.11: Operating mechanism of paper C.

array improves after the embedding with the slotted-frame, compared to the free space scenario.

There are several design parameters that are critical to obtain an optimized performance. The number of slots etched on the frame should be as large as the mm-wave array aperture, considering the beam-steering behavior. The slot shape is important to maximize the antenna gain in the operating bandwidth. The optimal separation between the slots corresponds to $0.243\lambda_0$. This solution is valid for quite small antenna-frame distances, with $0.043\lambda_0$ the value chosen for the design.

In Paper D, inspired by the operation mechanism of hard surfaces, corrugations are etched on the edges of the frame to make it transparent to electromagnetic waves and allow the energy to go through. This method has been depicted in Fig. 3.12.

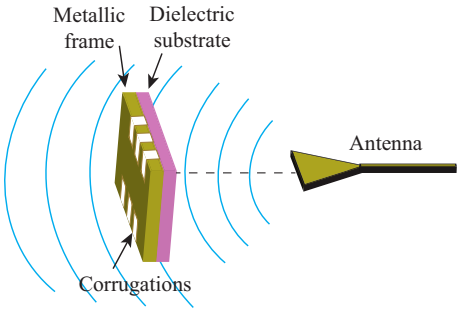

Fig. 3.12: Operating mechanism of paper D.

This solution can achieve almost the same gain as the antenna in a free space scenario within the operating bandwidth. The groove length is the most sensitive parameter of the design. Its value should be comprised between $\lambda_g/4$ and $\lambda_g/2$. A higher relative permittivity of the substrate placed behind the metallic frame in Paper D allows reducing the length of the corrugations, which would make the frame more robust and the grooves less visible to the human eye. The groove periodicity has to be smaller than $\lambda/2$. The width of the corrugations barely affects the gain of the mm-wave array.

An interested reader is kindly encouraged to read the three different solutions in the noted papers for more details. As a summary, the main design parameters of the papers are shown in Table 3.1. The column *gain compared to free space* represents the realized gain variation of the mm-wave antenna without the frame and with the proposed modified frame. The table shows that the separation distance between the mm-wave antenna and the frame is the smallest in the method presented in Paper C. Moreover, it employs the widest frame and the gain increment is between 1 and 1.5 dBi compared to the antenna in free space. Paper D also increases the gain in some parts of the operating bandwidth, and the antenna-frame distance is 1 mm.

Table 3.1: Design parameters comparison. Unit: mm.

Paper	Width frame	Thickness frame	Antenna-frame distance	Antenna type	Gain compared to free space
B	3	0.3	7	Vivaldi	$1-2$ dBi loss
C	7	0.3	0.5	Bow-tie	$1-1.5$ dBi gain
D	5	0.653	1	Vivaldi	$0-1$ dBi gain
[14]	7	0.8	2	Vivaldi	-

Nevertheless, to provide a comparison among the proposed solutions under the same conditions, an unified simulation model with the dual-fed dual-band patch located in the top center of the phone has been employed, with an antenna-frame distance of 5 mm and a frame width of 5 mm. Apart from the three different solutions proposed in the papers and the solution from Kurvinen *et al.* [14], the radiation patterns of the antenna without a frame and with a normal frame have been included as a reference. The results of the vertical and horizontal polarizations are presented in Fig. 3.13 and Fig. 3.14, respectively.

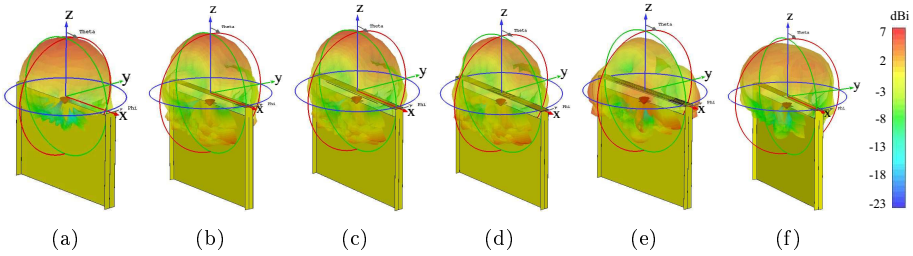

Fig. 3.13: Vertical polarization realized gain radiation pattern. (a) No frame. (b) Normal frame. (c) Parasitic layers from Paper B. (d) Slotted frame from Paper C. (e) Hard surface inspired frame from Paper D. (f) Window etched on the frame from Kurvinen *et al.* [14].

As observed, the vertical polarization is hardly affected by the presence of a metallic frame with the given dimension. Moreover, all the proposed methods can also allow the propagation of the vertical polarization towards the $+z$ direction. It is important to note that the proposed methods in this dissertation are designed for the horizontal polarization. However, since dual-polarized antenna systems are desirable in the mm-wave bands, it is essential not to affect negatively the radiation pattern of vertically-polarized antennas with these methods. In Fig. 3.13, the vertical polarization of the solutions in Papers B and C provide a very similar radiation pattern to the antenna with the normal frame. The solution in [14] has a similar pattern to the one in free space, while the proposal of Paper D provides a radiation pattern with a slightly different shape.

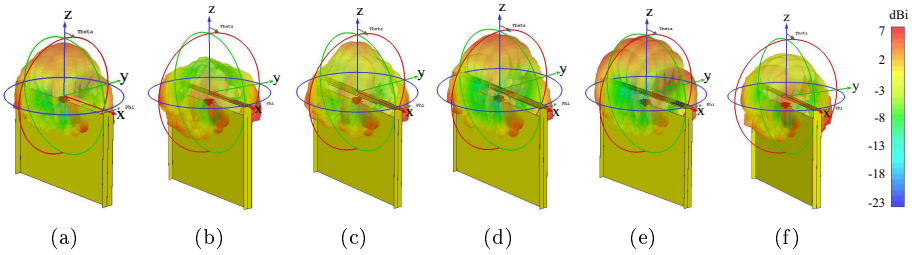

Fig. 3.14: Horizontal polarization realized gain radiation pattern. (a) No frame. (b) Normal frame. (c) Parasitic layers from Paper B. (d) Slotted frame from Paper C. (e) Hard surface inspired frame from Paper D. (f) Window etched on the frame from Kurvinen *et al.* [14].

For the results of horizontal polarization, it is more critical to adopt the proposed solutions for the 5G mm-wave devices since the radiation towards the desired $+z$ direction has been significantly blocked, and all the methods that are presented here can greatly improve the antenna gain on $+z$ direction. Comparing the different methods for the horizontal polarization, it is possible to see that the radiation patterns of Papers C and D (Fig. 3.14(d, e)) resemble more the radiation pattern in free space. The solution in Paper B provides a higher gain in the desired direction than the window cut off from the frame in [14].

3.3 Summary

The frame impact on the radiation of mm-wave arrays is presented in this chapter. When the frames are compared according to the material employed, i.e., plastic, glass and metal, the metallic frame is the one that provides the worse performance in the presence of the mm-wave antenna. The effect of a wider metallic frame is quite noticeable for both polarizations, even though the vertical polarization is less affected. For that reason, three methods to reduce the metallic frame obstruction of the radiation pattern have been proposed in this dissertation, based on Papers B-D. The methods have also been compared in equal conditions. The width of the frame especially affects the solution proposed in Paper B, due to the fact that the coupling in the parasitic layers becomes smaller for the horizontal polarization. The solutions in Papers C and D yield a very similar radiation pattern to the antenna without a frame, with the solution in C having the smallest antenna-frame separation distance. The proposed methods can be applied to different antenna typologies and form factors.

References

[1] R. Rodríguez-Cano, S. Zhang, and G. F. Pedersen, "Beam-steerable multi-band mm-wave bow-tie antenna array for mobile terminals," in *12th European Conference on Antennas and Propagation (EuCAP 2018)*, 2018, pp. 1–4.

[2] R. A. Alhalabi and G. M. Rebeiz, "Differentially-fed millimeter-wave yagi-uda antennas with folded dipole feed," *IEEE Transactions on Antennas and Propagation*, vol. 58, no. 3, pp. 966–969, 2009.

[3] X. Ruan and C. H. Chan, "An endfire circularly polarized complementary antenna array for 5G applications," *IEEE Transactions on Antennas and Propagation*, vol. 68, no. 1, pp. 266–274, 2019.

[4] R. M. Moreno, J. Ala-Laurinaho, A. Khripkov, J. Ilvonen, and V. Viikari, "Dual-polarized mm-wave endfire antenna for mobile devices," *IEEE Transactions on Antennas and Propagation*, vol. 68, no. 8, pp. 5924–5934, 2020.

[5] C. Di Paola, S. Zhang, K. Zhao, Z. Ying, T. Bolin, and G. F. Pedersen, "Wideband beam-switchable 28 GHz quasi-yagi array for mobile devices," *IEEE Transactions on Antennas and Propagation*, vol. 67, no. 11, pp. 6870–6882, 2019.

[6] J. Zhang, K. Zhao, L. Wang, S. Zhang, and G. F. Pedersen, "Dual-polarized phased array with end-fire radiation for 5G handset applications," *IEEE Transactions on Antennas and Propagation*, vol. 68, no. 4, pp. 3277–3282, 2019.

[7] J. Park, H. Seong, Y. N. Whang, and W. Hong, "Energy-efficient 5G phased arrays incorporating vertically polarized endfire planar folded slot antenna for mm-wave mobile terminals," *IEEE Transactions on Antennas and Propagation*, vol. 68, no. 1, pp. 230–241, 2019.

[8] Y.-W. Hsu, T.-C. Huang, H.-S. Lin, and Y.-C. Lin, "Dual-polarized quasi yagi–uda antennas with endfire radiation for millimeter-wave MIMO terminals," *IEEE Transactions on Antennas and Propagation*, vol. 65, no. 12, pp. 6282–6289, 2017.

[9] I.-J. Hwang, B. Ahn, S.-C. Chae, J.-W. Yu, and W.-W. Lee, "Quasi-yagi antenna array with modified folded dipole driver for mmwave 5G cellular devices," *IEEE Antennas and Wireless Propagation Letters*, vol. 18, no. 5, pp. 971–975, 2019.

[10] R. Rodriguez-Cano, S. Zhang, K. Zhao, and G. F. Pedersen, "Reduction of main beam-blockage in an integrated 5G array with a metal-frame antenna," *IEEE Transactions on Antennas and Propagation*, vol. 67, no. 5, pp. 3161–3170, 2019.

[11] R. Rodriguez-Cano, S. Zhang, K. Zhao, and G. F. Pedersen, "mm-wave beam-steerable endfire array embedded in a slotted metal-frame LTE antenna," *IEEE Transactions on Antennas and Propagation*, vol. 68, no. 5, pp. 3685–3694, 2020.

[12] R. Rodriguez-Cano, K. Zhao, S. Zhang, and G. F. Pedersen, "Handset frame blockage reduction of 5G mm-wave phased arrays using hard surface inspired structure," *IEEE Transactions on Vehicular Technology*, vol. 69, no. 8, pp. 8132–8139, 2020.

[13] J. Helander, K. Zhao, Z. Ying, and D. Sjöberg, "Performance analysis of millimeter-wave phased array antennas in cellular handsets," *IEEE Antennas and Wireless Propagation Letters*, vol. 15, pp. 504–507, 2016.

[14] J. Kurvinen, H. Kähkönen, A. Lehtovuori, J. Ala-Laurinaho, and V. Viikari, "Co-designed mm-wave and LTE handset antennas," *IEEE Transactions on Antennas and Propagation*, vol. 67, no. 3, pp. 1545–1553, 2019.

[15] J. Bang and J. Choi, "A SAR reduced mm-wave beam-steerable array antenna with dual-mode operation for fully metal-covered 5G cellular handsets," *IEEE Antennas and Wireless Propagation Letters*, vol. 17, no. 6, pp. 1118–1122, 2018.

[16] B. Yu, K. Yang, C. Sim, and G. Yang, "A novel 28 GHz beam steering array for 5G mobile device with metallic casing application," *IEEE Transactions on Antennas and Propagation*, vol. 66, no. 1, pp. 462–466, 2018.

[17] S. S. Kim, S. H. Kim, J. H. Bae, and Y. J. Yoon, "Switched folded slot phased array antenna for mm-wave 5G mobile in metal bezel design," in *2018 IEEE International Symposium on Antennas and Propagation. USNC/URSI National Radio Science Meeting*, 2018, pp. 239–240.

[18] Y. Wang, H. Huang, and X. Jian, "Novel design of a dual-band 5G mm-wave antenna array integrated with a metal frame of a cellular phone," in *2018 Asia-Pacific Microwave Conference (APMC)*, 2018, pp. 1582–1584.

Chapter 4. Conclusion

The inclusion of new frequency bands in the 5G mobile communication has required a re-evaluation of all the antenna design-related guidelines. Since the propagation characteristics in the new mm-wave bands are not as favorable as in the sub-7 GHz bands, a higher gain antenna system, with a specific spherical coverage, is required to compensate for the losses. The higher frequencies of operation can be translated to smaller wavelengths, which make the antennas more susceptible to all the objects around them. For that reason, not only new antenna topologies need to be employed, but the impact of the phone housing environment around the mm-wave antennas needs to be assessed. This thesis has focused on the latter.

The phone covers affect the behavior of the mm-wave antennas. The rear cover can be made of different materials, e.g., plastic, glass or metal. Dielectric covers with high relative permittivity, such as glass, disturb the radiation patterns of mm-wave antennas more, since they allow further propagation of the surface waves, while metallic covers do not allow the propagation of electromagnetic waves through them. A method to reduce the glass cover effect on the radiation of mm-wave antennas, that are located below the glass, was proposed in this dissertation. This method focused on stopping the propagation of the surface current and was realized with a planar structure, printed on the back cover. To further suppress the impact of the surface current for a mm-wave antenna-on-display design, another method was proposed, consisting of two transparent rows of parasitic radiators placed next to a mm-wave antenna-on-display. The parasitic radiators stop the propagation of surface current on the glass and reduce the ripples on the radiation patterns of antennas-on-display.

Currently, it is also a common choice to adopt metal to construct the phone frame, due to mechanical robustness and aesthetics. It is a known fact that the electromagnetic radiation does not propagate through metal. Therefore, the radiation of endfire antennas will be reflected back by the metal. In the smaller area that comprises the phone frame, the impact of the metallic frame on the radiation emitted by the mm-wave antenna is even more critical. Especially for the horizontal polarization, with the vertical polarization almost

undisturbed for narrow-width frames. Three different solutions were developed to diminish the obstruction, caused by the frame, to the radiation pattern of horizontally-polarized antennas. To prove the concept, endfire antennas have been employed. However, these methods can be applied to other topologies and phone form factors. The first solution consisted of placing two tilted parasitic layers, at both sides of the frame, that coupled the energy impinging on the frame and added it in-phase in the far-field. The second method consisted of slots etched on the metallic frame. These slots could be seen as a secondary array that was illuminated by the mm-wave array, and was able to increase the maximum gain. The last method was inspired by the wave propagation on hard surfaces, which are realized by dielectric-filled corrugations longitudinally oriented with respect to the direction of propagation. In the proposed method, the corrugations were etched at the edges of the frame and allowed the electromagnetic waves to propagate through them.

As has been shown in this dissertation, the performance of mm-wave antennas is highly dependent on the components that surround the antenna. Therefore, future mm-wave antenna designs need to consider the effect of the metallic frame or the high-permittivity dielectric cover placed on top of the module. Future research, that focus on making the components around the mm-wave antenna, e.g., front and rear cover with high permittivity, to be transparent to the propagation of electromagnetic waves and be robust to different antenna topologies, needs to be carried on. As an example, the latest developments on the process technologies on glass, allow designing a metallic structure, e.g., unit cell on the glass rear cover or front display panel, with a higher degree of freedom, while maintaining the optical invisibility. This would allow the designs that have been presented in Chapter 2 to achieve a better electromagnetic transparency. The improvement on transparent electromagnetic behavior should consider the different angles of incidence of the waves on the surfaces, due to the different beam-steering angles, as well as strive to cover a large bandwidth to meet the demand of mm-wave communications. From the aspect of reducing the effect of the metallic frame, the proposed methods in this thesis need further development, so that they can be employed in a more realistic phone environment and be robust to various design parameters. Expanding the proposed methods to support multiple bands of operation, is another important factor that needs to be considered, to incorporate multiband 5G mm-wave modules.

Part II

Papers

Paper A

Transparent mm-Wave Array on a Glass Substrate with Surface Wave Reduction

Rocío Rodríguez Cano, Shuai Zhang, Gert Frølund Pedersen

The paper has been published at the
2020 14th European Conference on Antennas and Propagation (EuCAP),
Copenhagen, Denmark, 2020, pp. 1-4, doi:
10.23919/EuCAP48036.2020.9136095.

Abstract

In this paper, a transparent dual-element millimeter-wave (mm-wave) array for handsets is proposed. The antenna is mounted on top of a glass display and it is made by diamond grid cells that provide a transparency of 86 %. In order to reduce the surface waves generated and make the radiation pattern more directive, several rows of meshed patches have been placed in front of the mm-wave bow-tie array. The antenna array operates from 26.5 to 29.5 GHz and has a total efficiency of more than 70 % in the operating bandwidth. The array is able to steer the beam 70° with a realized gain higher than 7 dBi.

I Introduction

New frequency bands have been introduced in the millimeter-wave (mm-wave) spectrum for the fifth generation of mobile communication (5G) [1]. For that reason, 5G-enabled handsets need to include antenna systems that cover the new bands. The limited available space in handsets has prompted the appearance of integrated low and high-frequency antennas [2–6] and new locations for the mm-wave antenna designs, where the antennas are printed on the active display region [7–10]. The glass display of the handset is employed as the substrate of the antenna. In [9], an optically invisible antenna is integrated within the OLED touch display of a smartwatch. In [10], a transparent Antenna-on-Display (AoD) solution are presented for handsets at 28 GHz. An optically invisible antenna and a transparent one are proposed in [7] for mm-wave frequencies. However, the total efficiency of the two antennas-on-display has low values: 29.83 % and 52.37 %, respectively.

One of the main challenges of planar antennas is the control of the surface waves. The appearance of surface waves is more noticeable with higher dielectric permittivity substrates, like glass [11]. There are several reasons why surface waves are detrimental to antennas: they distort the radiation pattern, increase the mutual coupling of the array and reduce the antenna efficiency. For those reasons, it is important to control the surface waves in the case of AoD.

One of the solutions proposed in literature to reduce the surface waves is to drill holes in the substrate to reduce the effective dielectric constant. However, since the mm-wave array is thought for antenna-on-display applications, the substrate cannot be perforated.

In this paper, a transparent array is presented to be placed on the handset display. Several layers of patches are located in front of the array to radiate the current coupled from the surface waves and thereby reduce their effect. The

array achieves high radiation efficiency.

II Antenna System Design

The handset is formed by a glass substrate and a metallic plane on the bottom. The transparent antenna system is printed on the top part of the display, as shown in Fig. A.1. Since the aim of this work is to show the surface wave reduction, the array is located in the longest edge of the terminal. This manner, the surface waves have more space to propagate without finding any edges. However, this solution can be employed in different locations and with different phone form factors.

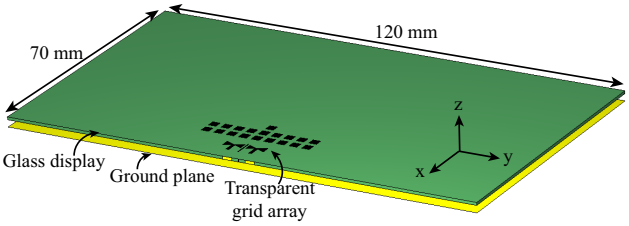

Fig. A.1: Exploded view of the transparent array mounted on the handset.

The antenna system configuration is detailed in Fig. A.2. The system is composed of 2 meshed bow-tie shaped monopoles. Since the bow-tie element provides high gain, only two antennas are needed so that the array gain is higher than 7 dBi in the frequency band. A strip is placed between the antenna elements to reduce the mutual coupling of the array. Since the aim is not to perforate the substrate, the strip is grounded on the edge of the glass. The structure proposed to reduce the surface waves consists of several row of meshed patches, as shown in Fig. A.2(a). The patches, which are fed by the surface waves, radiate most of the energy coupled from the monopoles, preventing it to propagate along the substrate. The size of the square patches is $a = 2.1$ mm, $b = 1.785$ mm and $c = 1.575$ mm. The display is made of a glass substrate of $\epsilon_r = 6$ and thickness of 0.7 mm. The unit cell that constitutes the grid has a thickness of 2000 Å and a width of 5 μm. For that mesh width, the optical transparency is 86 % [7] and the conductivity 2.675×10^6 S/m [12]. The dimensions of the grid are $w_{ver} = 100$ μm and $w_{hor} = 50$ μm (Fig. A.2(b)). The grid cells can be implemented with a photolithography process, as shown in [7].

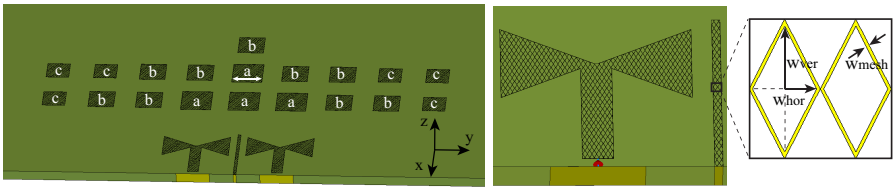

(a) (b)

Fig. A.2: Simulated models. (a) Antenna array with strip structure to reduce the surface waves. (b) Details of the mm-wave antenna and diamond grid.

III Surface Wave Reduction

The effect of surface waves in the radiation pattern can be detrimental in systems that require very directive antennas. The radiation patterns of the array and the proposed solution with radiating strips to reduce surface waves are represented in Fig. A.3. In the case of only the antenna array on the display, the main lobe gain is 7.6 dBi. The proposed array with strips can achieve 10.5 dBi.

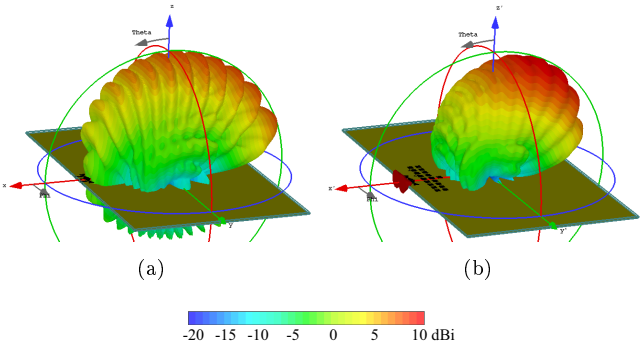

Fig. A.3: 3D realized gain radiation pattern. (a) Antenna array without strips. (b) Antenna array with patch structure to reduce the surface waves.

The polar radiation patterns of both structures are represented in Fig. A.4. As it can be seen in Fig. A.4(a), the propagation of the surface wave causes the appearance of ripples in the radiation pattern. The value of the realized gain in boresight (-30°) is 5 dB. On the other hand, when the patches are placed in front of the array, there is a gain enhancement of 5 dBi and the radiation pattern is smoother. Besides, the back lobes are reduced 5 dBi. The 3 dB angular width in the $\phi = 0°$ cut is 8.4° and 48.1° for the array without and with patches respectively. The deep ripples in the radiation pattern are

responsible for the large difference. The 3 dB angular width in the $\phi = 90°$ cut is 35.1° and 61.2°, respectively.

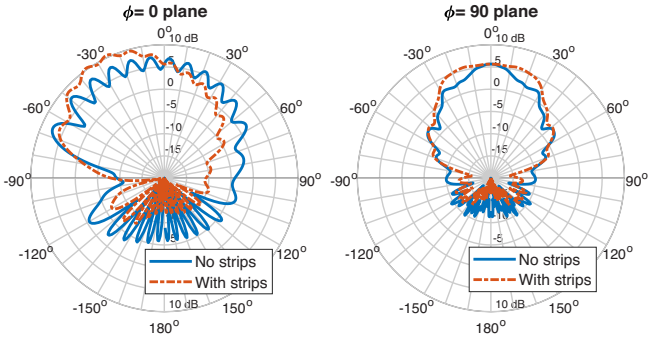

(a) (b)

Fig. A.4: In-phase realized gain radiation pattern at 28 GHz. (a) $\Phi = 0°$ plane. (b) $\Phi = 90°$ plane.

For a better comprehension of the mechanism to reduce the surfaces waves, the surface currents of the proposed mm-wave array have been represented in Fig. A.5 with and without the patches. When no patches are placed in front of the array (Fig. A.5(a)), it can be seen how the surface wave propagates in the glass. The surface wave is more noticeable in the direction of the center of the array (-x axis). With only one row of patches, the current is still larger in that direction. Adding two rows of patches redirects the surface current in more directions. The last patch added in a third row allows to reduce considerably the surface current in the original direction (-x axis). In conclusion, the presence of the patches decreases the surface currents up to 15 dB and as it can be seen in Fig. A.5(b) the surface waves are significantly reduced. This is due to the fact that the patches are fed by the surface currents. This allows the radiation of most of the energy.

IV Array Performance

The simulations results are carried out by CST Microwave Studio 2019. The S-parameters of the array are plotted in Fig. A.6. The reflection coefficient of the antenna is matched below -10 dB from 26.4 to 29.36 GHz. The transmission coefficient has been reduced with the presence of the grounded strip between the antennas, with a value lower than -13.2 dB in all the operating bandwidth. The total efficiency of the array is represented as well in Fig. A.6. The efficiency is higher than 70 % in all the bandwidth and it reaches a value of 83 % in the

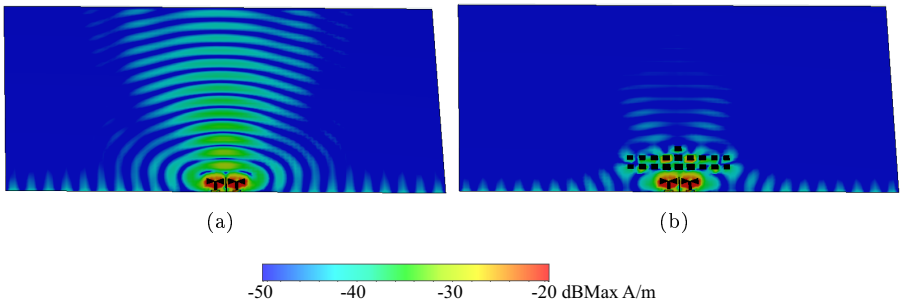

Fig. A.5: Surface currents at 28 GHz. (a) Without patches. (b) With patches.

frequency range 27.5-29 GHz.

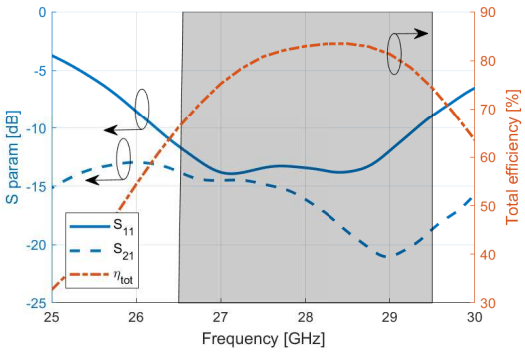

Fig. A.6: S parameters of the proposed design and total efficiency of the array (including mismatching losses).

The realized gain evolution as a function of the frequency in the boresight direction is plotted in Fig. A.7. The realized gain is higher than 9 dBi in the operating frequency band.

Since high gain antennas provide narrow beams, mm-wave arrays are required to steer the beam to provide wide coverage. One of the important figures of merit is the beam-steering envelope. It is calculated by selecting the beam that provides the maximum gain at every angle. The beam-steering envelope of 12 different beams is represented in Fig. A.8. Since the direction of the main beam is tilted with respect to the axes of Fig. A.2, the coordinate system has been rotated -25° (with the y axis fixed). The reason why the radiation pattern is tilted in the xz plane is due to the combination of structures with different radiation patterns. In other words, the bow-tie monopoles present an endfire radiation pattern, while the rows of patches have broadside radiation.

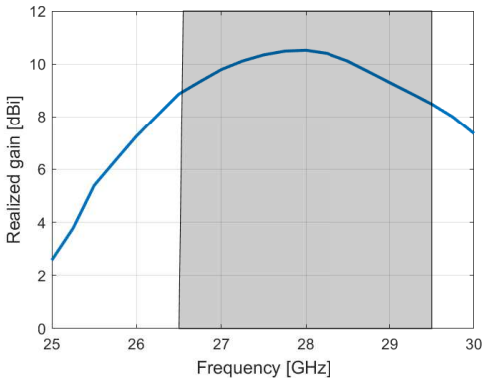

Fig. A.7: Realized gain evolution in terms of frequency in the boresight direction.

The maximum scanning angle for a realized gain higher than 7 dBi is $\theta = \pm 35°$.

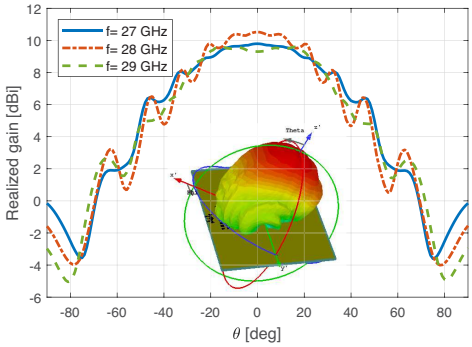

Fig. A.8: Beam-steering envelope. The coordinate system has been rotated -25° (with the y axis fixed) with respect to the one in Fig. A.2, to point at boresight.

V Conclusion

A transparent mm-wave array has been designed for Antenna-on-Display applications. Several rows of patches have been places in front of the array to reduce the surface wave propagating in the glass substrate. This makes the radiation pattern more directive and with less ripples. The array operates in the frequency range 26.4-29.3 GHz and presents a total efficiency higher than 70 % in all the bandwidth. The array is able to beam-steer $\theta = \pm 35°$, with a gain higher than 7 dBi.

Acknowledgment

This work was supported by the InnovationsFonden project of Reconfigurable Arrays for Next Generation Efficiency (RANGE).

References

[1] J. Lee, E. Tejedor, K. Ranta-aho, H. Wang, K.-T. Lee, E. Semaan, E. Mohyeldin, J. Song, C. Bergljung, and S. Jung, "Spectrum for 5G: Global status, challenges, and enabling technologies," *IEEE Communications Magazine*, vol. 56, no. 3, pp. 12–18, 2018.

[2] J. Kurvinen, H. Kähkönen, A. Lehtovuori, J. Ala-Laurinaho, and V. Viikari, "Co-designed mm-wave and LTE handset antennas," *IEEE Transactions on Antennas and Propagation*, vol. 67, no. 3, pp. 1545–1553, March 2019.

[3] R. Rodriguez-Cano, S. Zhang, K. Zhao, and G. F. Pedersen, "Reduction of main beam-blockage in an integrated 5G array with a metal-frame antenna," *IEEE Transactions on Antennas and Propagation*, vol. 67, no. 5, pp. 3161–3170, May 2019.

[4] M. M. Samadi Taheri, A. Abdipour, S. Zhang, and G. F. Pedersen, "Integrated millimeter-wave wideband end-fire 5G beam steerable array and low-frequency 4G LTE antenna in mobile terminals," *IEEE Transactions on Vehicular Technology*, vol. 68, no. 4, pp. 4042–4046, April 2019.

[5] M. S. Sharawi, M. Ikram, and A. Shamim, "A two concentric slot loop based connected array MIMO antenna system for 4G/5G terminals," *IEEE Transactions on Antennas and Propagation*, vol. 65, no. 12, pp. 6679–6686, Dec 2017.

[6] R. Rodriguez-Cano, S. Zhang, K. Zhao, and G. F. Pedersen, "Mm-wave beam-steerable endfire array embedded in slotted metal-frame LTE antenna," *IEEE Transactions on Antennas and Propagation*, 2020.

[7] J. Park, S. Y. Lee, J. Kim, D. Park, W. Choi, and W. Hong, "An optically invisible antenna-on-display concept for millimeter-wave 5G cellular devices," *IEEE Transactions on Antennas and Propagation*, vol. 67, no. 5, pp. 2942–2952, May 2019.

[8] W. Hong, S. Ko, Y. G. Kim, and S. Lim, "Invisible antennas using mesoscale conductive polymer wires embedded within OLED displays," in *2017 11th European Conference on Antennas and Propagation (EUCAP)*, March 2017, pp. 2809–2811.

[9] W. Hong, S. Lim, S. Ko, and Y. G. Kim, "Optically invisible antenna integrated within an OLED touch display panel for IoT applications," *IEEE Transactions on Antennas and Propagation*, vol. 65, no. 7, pp. 3750–3755, July 2017.

[10] J. Park, S. Y. Lee, Y. Kim, J. Lee, and W. Hong, "Hybrid antenna module concept for 28 GHz 5G beamsteering cellular devices," in *2018 IEEE MTT-S*

International Microwave Workshop Series on 5G Hardware and System Technologies (IMWS-5G), Aug 2018, pp. 1–3.

[11] G. John, R. Chatterjee, and S. Chatterjee, "Effects of environment on the surface wave characteristics of a dielectric-coated conductor-part iv," *Journal of the Indian Institute of Science*, vol. 59, no. 1, p. 51, 2013.

[12] S. Y. Lee, D. Choi, Y. Youn, and W. Hong, "Electrical characterization of highly efficient, optically transparent nanometers-thick unit cells for antenna-on-display applications," in *2018 IEEE/MTT-S International Microwave Symposium - IMS*, June 2018, pp. 1043–1045.

Paper B

Reduction of Main Beam-Blockage in an Integrated 5G Array With a Metal-Frame Antenna

Rocío Rodríguez Cano, Shuai Zhang, Kun Zhao, Gert Frølund Pedersen

The paper has been published at the
IEEE Transactions on Antennas and Propagation. Volume: 67, Issue: 5, May 2019, pp. 3161–3170.

Abstract

In this paper, a novel technique is introduced to reduce the handset metal-frame blockage to the main beam of a millimeter-wave (mm-wave) end-fire antenna array. The metal-frame blockage to mm-wave antennas with different polarizations is investigated first. It is found that the blockage is more severe for horizontal polarization than for vertical polarization. The effect of the metal bezel on a mm-wave array with horizontal polarization can significantly be decreased if two tilted layers of coupled metal strips are placed at the borders of the frame. Furthermore, these metal strips are shown not to disturb mm-wave antennas with vertical polarization. Different detailed design considerations are studied. To further demonstrate the idea, a 5G Vivaldi array (with horizontal polarization) is designed and integrated with a metal frame. The frame functions as a low-frequency antenna, operating in two frequency bands of 865-990 MHz and 1358-2786 MHz. The millimeter-wave array with four elements operates at the frequency band 24.25-27.5 GHz and can scan ±60 degrees in end-fire direction, with a realized gain higher than 7 dBi in most of the frequency range.

I Introduction

The upcoming fifth generation of mobile communications (5G) proposes more frequency bands to cope with the exponential demand of capacity and data traffic [1–4]. The millimeter-wave (mm-wave) band presents several challenges in terms of propagation. Since the propagation losses increase with frequency, higher gain antenna systems are required in mm-wave bands. As a result of the increased gain, the beamwidth becomes narrower and consequently, arrays are needed to steer the beam throughout the sphere. Electronic beam-steering is the most compact approach for mobile devices. There are two methods to steer the beam electronically; the first consists of switching the antennas [5,6] and the other involves changing the relative phases of the signals which drive each antenna element (phased arrays) [7–13]. It is also possible to combine both methods by having several sub-arrays [8–11].

5G-enabled handsets need to include antennas operating at these new frequency ranges. The current tendency in mobile terminals is to include an increasing amount of components in small spaces. Because of the decreasing volume left in the phone, a good approach is to integrate the new mm-wave antennas with the existing ones. Many antenna designs for mobile terminals at mm-wave frequencies present end-fire radiation since they have higher spherical coverage [14] and are less sensitive to user effects in mm-wave bands [12,15]. Conventional handsets with metal-frame designs have become a dominant trend

nowadays. However, none of the previous designs in [5,8,9,12–16] takes the handset metal frame into account. When a metal frame is placed in front of mm-wave end-fire antennas, severe distortion of the radiation pattern may occur due to the main beam blockage. This degradation can be translated into a shrinkage of the end-fire radiation bandwidth or a full deterioration of the pattern to broadside or other directions.

In [16], a layer of grating strips is added to obtain end-fire radiation, when a planar inverted-F antenna (PIFA) is placed in front of the high-frequency antenna. In this case, the operating mechanism is similar to the optical interferometers [17]. The distance between the grating strips and the PIFA is designed to be a quarter wavelength at a certain frequency and the end-fire radiation can be achieved within a band around that frequency. However, the bandwidth in which the antenna can remain with a stable end-fire radiation pattern would become very narrow when applying this technique for a metal-frame handset. In [7,18,19], mm-wave slot arrays have been etched on a metal frame, and the end-fire beams are not blocked by the bezel anymore. Nevertheless, in order to excite these slots, the feeding cable (or other transmission lines) has to connect the PCB ground to the metal bezel. This would change the low-frequency antenna performance if a metal bezel antenna at sub 3 GHz is applied. Moreover, introducing additional feeding structures to the metal bezel would also complicate the practical implementations. Therefore, it is necessary to propose a technique which is able to reduce the main beam blockage in an integrated end-fire 5G array with a metal-frame antenna operating at low frequencies.

In this paper, a mm-wave Vivaldi antenna array (with end-fire radiation pattern) is integrated together with a metal-frame antenna at sub 3 GHz. Two layers of coupled metal strips are introduced to overcome the directional obstruction of the metal frame to the main beam of the Vivaldi array. These metal strips do not alter the performance of the metal-frame antenna. The mm-wave antenna array is designed to operate at the 5G pioneer band in Europe, from 24.25-27.5 GHz [20]. Simulations are carried out by CST Microwave Studio 2018 and a prototype is manufactured and measured.

The manuscript is organized as follows; Section II introduces the degradation produced by the mobile phone frame in the radiation pattern of horizontally polarized antennas and the effect of the frame width. Section III describes the operating mechanism and the proposed structure to overcome this problem. Design considerations are also explained. In Section IV, the final parameters of the antenna design are listed and the performance is assessed, with measurements and simulations.

II Effect of the metal frame on mm-wave antennas

As mentioned in the introduction, the metal frame of mobile devices may block the radiation from the end-fire antennas in the mm-wave frequency range. In order to provide a clear picture of this point, the impact of the metal frame on the radiation pattern of mm-wave antennas is analyzed. First, according to the polarization and then, with a parametric study of the frame width.

A. Polarization dependence of the metal-frame blockage to the radiation pattern

In 5G mobile handsets, mm-wave antenna arrays with dual polarization are preferred. In this section, the metal-frame blockage to different polarizations is investigated. To carry out this study, two patches, one with vertical polarization (Fig. B.1 (a)) and the other with horizontal (Fig. B.1 (b)), are placed 7 mm away from a 5 mm-wide frame, which is the typical clearance in handsets. Please note that the frame width referred throughout this paper is the dimension in the z axis.

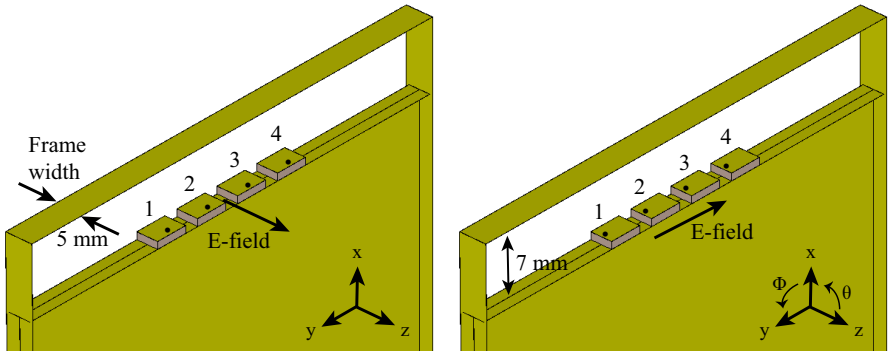

Fig. B.1: Simulated patch antennas with frame and ground plane. (a) Vertical polarization. (b) Horizontal polarization.

The effect of the frame on the radiation patterns of vertical and horizontal polarizations are shown in Fig. B.2 and Fig. B.3, respectively. The radiation patterns are obtained by exciting the third element of the array with the others terminated with 50 Ω loads. The realized gain of two perpendicular cuts is plotted in the figures. In Fig. B.2, when a metal frame is included, the

vertically-polarized patch has some energy reflected back, but the main beam still points to the end-fire direction and the radiation patterns do not vary significantly. However, as plotted in Fig. B.3, the main direction of radiation in horizontal polarization is much more sensitive to the frame than the vertical polarization. There is also a loss of more than 6 dB in the $+x$ axis ($\phi = 0°$ and $\theta = 90°$). The reason for the severe blockage to the horizontal polarization may be explained as follows: the wavelength at the center frequency of the band, 26 GHz, is over one time longer than the frame width (5 mm). For the horizontal polarization, the amplitude of the electric field varies in the y axis, which is totally blocked by the metal frame (see Fig. B.1). In the case of vertical polarization, the amplitude of electric field varies in the z axis, not in the y axis, and thus the wavefront is only partially obstructed.

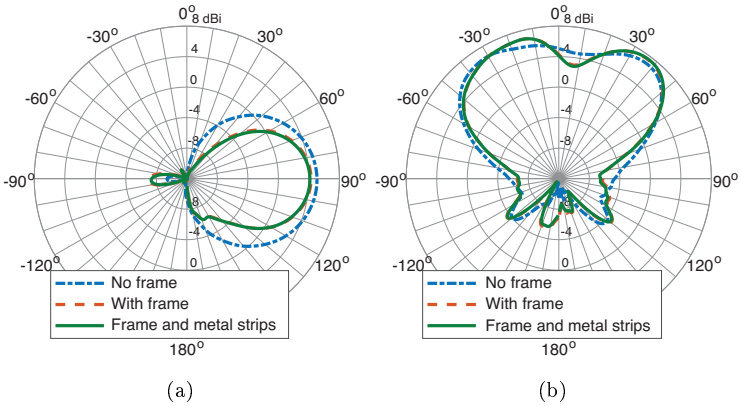

Fig. B.2: Effect of the parasitic metal strips on the realized gain radiation patterns of vertical polarization at 26 GHz. (a) $\phi = 0°$ cut. (b) $\theta = 90°$ cut.

Since the degradation of the radiation pattern when the frame is added is not significant for vertical polarization, from now on, only the case of horizontal polarization is assessed.

B. Effect of the frame width

The contribution of the frame width to the degradation of the radiation pattern is plotted in Fig. B.4. Only the gain (IEEE) radiation patterns of the central element are shown. The IEEE definition of gain equals the antenna directivity plus the antenna radiation efficiency in logarithmic scale, and thus the mismatching loss is not included. As the width increases, the energy in the end-fire direction decreases and more energy reflects in other directions. This effect is even more noticeable when the width is larger than 2 mm.

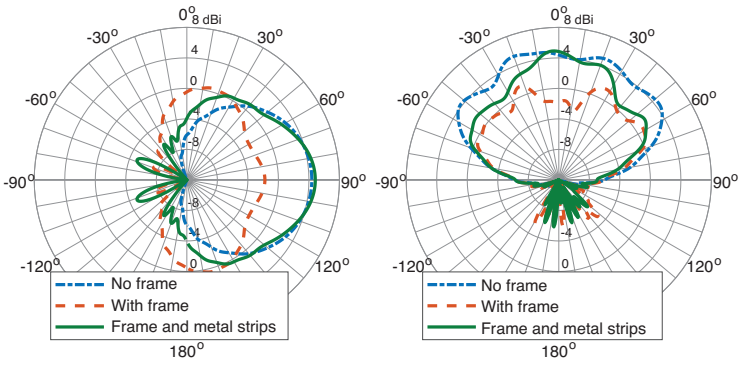

Fig. B.3: Effect of the parasitic metal strips on the realized gain radiation patterns of horizontal polarization at 26 GHz. (a) $\phi = 0°$ cut. (b) $\theta = 90°$ cut.

Therefore, it can be concluded that the blockage effect of the metal frame is more critical for the radiation pattern in the case of the horizontal polarization than the vertical. In the next section, a novel technique is introduced to overcome this blockage.

III Metal strip layers coupled to the frame

As stated in the previous section, mm-wave end-fire arrays with horizontal polarization face a degradation of the radiation pattern when the metal frame is added in a handset. To overcome this problem, coupled strip layers are introduced in this section.

To illustrate the polarization impact, a patch antenna was chosen. Nevertheless, one of the main drawbacks of patch antennas is their narrowband impedance matching. In order to cover the band n258 of the mm-wave spectrum, a wideband, high-gain antenna with robust radiation pattern is needed. The Vivaldi element is a good reference antenna to study in the presence of the frame, due to its high gain and stable radiation pattern in a wide band. For that reason, in the rest of the paper, the Vivaldi antenna is analyzed.

A. Fundamental mechanism

The concept of the coupled strip layers consists of two tilted strips placed at both sides of the frame, as shown in Fig. B.5 (a). The mm-wave antenna radiates towards the frame. A portion of the energy is reflected back, but

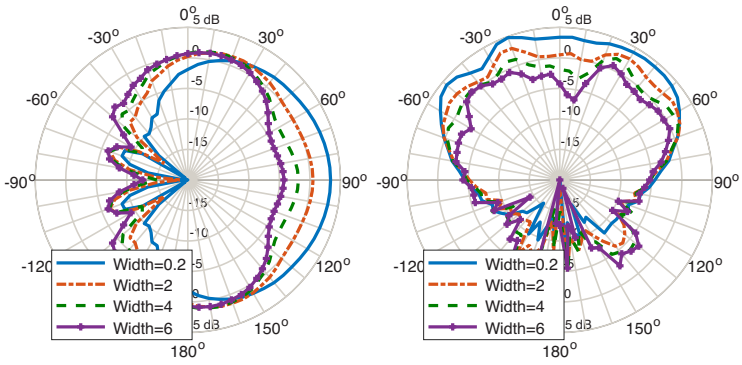

(a) (b)

Fig. B.4: Effect of the frame width in the gain (IEEE) radiation pattern at 26 GHz. (a) $\phi = 0°$ cut. (b) $\theta = 90°$ cut. See coordinates in Fig. B.1.

the larger part is coupled to the metal strip layers. The two metal strip layers work as parasitic radiators, which re-radiate the electromagnetic waves coupled from the two edges of the metal frame towards the original direction. Since the distance from the mm-wave antenna to each metal strip layer is the same, the electromagnetic waves re-radiated are added in phase, which combines into end-fire radiation pattern again in the far-field. In other words, the strips can be regarded as two radiating sources fed by the coupling of the energy from the frame. The electric field propagation is represented in Fig. B.5 (b) at a time instant for a frequency of 26 GHz. The first wavefront can be seen at the left side of the picture, originated by the sum of the coherent radiation from the parasitic strips. The strip layers are required to be close to the frame to acquire enough coupled energy. This is one of the differences with the optical interferometer, in which the distance is required to be around a quarter wavelength [17].

B. Impact of the coupled strip layers in the radiation of an antenna array

To compensate the high path losses in the mm-wave band, antenna arrays are proposed to be embedded in mobile terminals. The principle of adding strips at both sides of the frame can be extended for the array case. The purpose of the mm-wave array is steering the beam to provide a good coverage of the upper hemisphere. For that reason, each layer is composed of many strips. Fig. B.6 shows the two layers at both sides of the frame with several metal strips.

To further demonstrate this concept, the surface current of the Vivaldi array

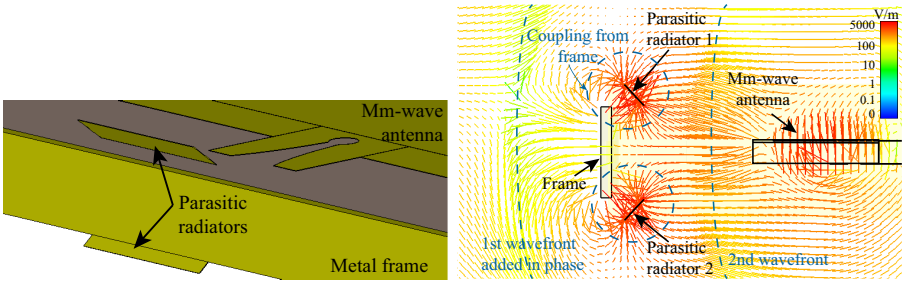

(a) (b)

Fig. B.5: (a) Mm-wave antenna with frame and metal strips. (b) E-field of the mm-wave antenna with frame and metal strip layers (side view).

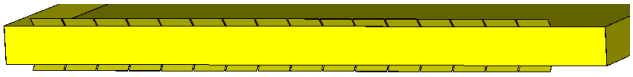

Fig. B.6: Front view of the metal strip layers for the mm-wave array.

has been plotted along the frame with and without metal strips layers in Fig. B.7. It can be seen in Fig. B.7 (a) that the currents flow as standing waves, while in Fig. B.7 (b) the currents are coupled along the edges to the metal strip layers and become weak close to the center of the frame.

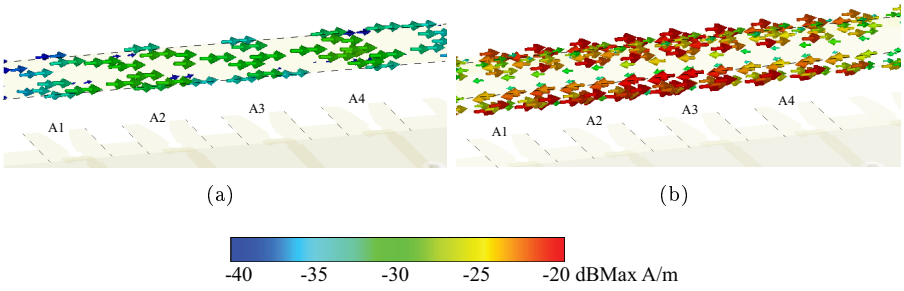

(a) (b)

Fig. B.7: Surface current comparison in dBA/m with respect to the maximum value at 26 GHz. (a) Without metal strip layers. (b) With metal strips.

The previous subsection introduced the operating principle of the strip layers. For a better comprehension of the mechanism, the effect of the number of strip layers is assessed below. Fig. B.8 (a) represents the radiation patterns of the Vivaldi array with no frame (in free-space) with all the elements excited in phase. Fig. B.8 (b) shows the effect of the frame on the radiation pattern of the array. The width of the metal frame in front of the array (top part) is set

to be 3 mm in this study. The frame decreases the gain of the array by at least 3 dBi at the two higher frequencies, and by more than 4 dBi at 24.25 GHz. If only one layer of metal strips is added close to the edge of the frame (Fig B.8 (c)), the IEEE gain in the end-fire direction ($+x$ axis) is improved at 24.25 GHz, but the sidelobes decrease the gain at the higher frequencies. Nonetheless, placing two layers of strips redirects the radiation to the $+x$ axis direction across the target bandwidth, as shown in Fig. B.8 (d). This happens due to the coupling of the electromagnetic wave from the frame to the metal strips. The metal layers radiate the coupled energy to the desired end-fire direction. Fig. B.9 shows the IEEE gain of the array at the $+x$ axis for the different number of metal strip layers placed at the edges of the frame. The IEEE gain when one layer of metal strips is added is higher than the one with only frame at the lower frequencies of the band, but when the frequency increases, the side lobes have higher value. The improvement in the gain is more significant when the two layers are placed since the two metal layers act as two elements of an array.

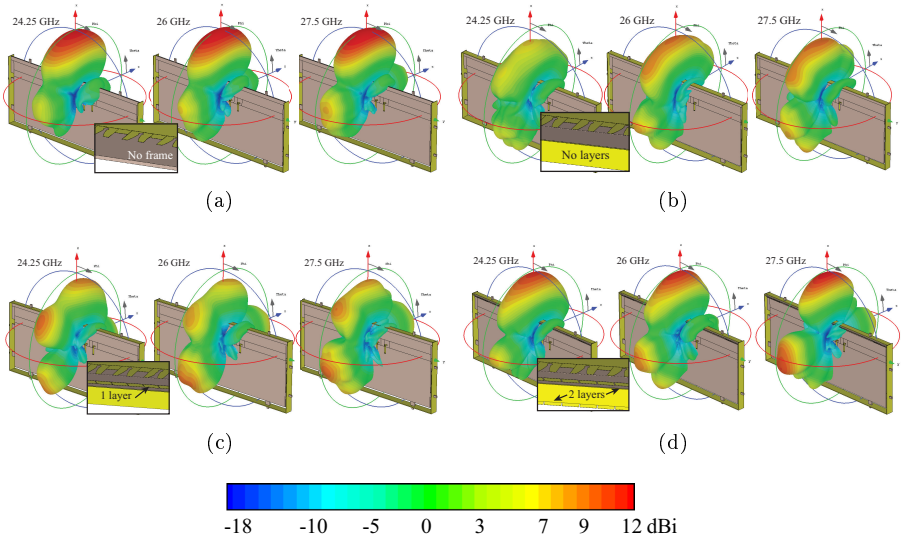

Fig. B.8: IEEE gain comparison of the in-phase Vivaldi array according to the number of layers of metal strips at different frequencies. (a) No frame. (b) No layers. (c) 1 layer. (d) 2 layers.

In order to show that the strip layers do not affect the vertical polarization, the plots of the patch antenna with strip layers have also been included in Fig. B.2 and B.3 for both polarizations. Simulations show that the realized gain, for the vertical polarization, does not vary when the two coupled metal strips layers have been placed next to the borders of the frame (Fig. B.2). This

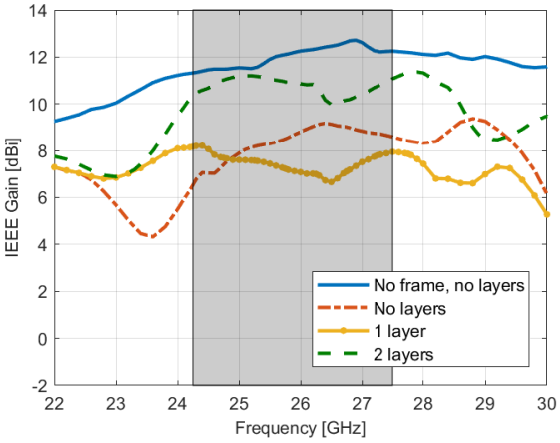

Fig. B.9: End-fire IEEE gain (in the $+x$ axis) of the array according to the number of metal strip layers as a function of the frequency.

means that the parasitic strips do not degrade the vertical polarization. The improvement of the gain is about 7 dBi in the case of horizontal polarization (Fig. B.3) compared to the structure with only the frame. The main beam points again to the original direction ($+x$ axis).

C. Design considerations for the integration of a mm-wave array and a metal frame-antenna

The principle and effectiveness of the coupled metal strip layers have been demonstrated in previous section. In this section, several considerations for the design of the integrated mm-wave array with the frame antenna are investigated, such as angle of the strip layers, gap between the strips, strip length and antenna-frame distance. The optimal configuration for the integration of a mm-wave array and a metal frame antenna can be revealed through the parametric studies. In addition, it should be noticed that, in all the sweeps, IEEE gain is used instead of realized gain. The IEEE gain is adopted to exclude the changes in the antenna impedance matching for some configurations, which provides a fair comparison. The matching is, however, better than -6 dB in the worst case.

Effect of the angle of the strip layers

The IEEE gain of the array in the $+x$ axis has been represented in Fig. B.10 for different angles of the strip layers. The rotation is made by fixing the edge

of the layer that is further away from the frame (see Fig. B.10). The gain variation is not significant in all the cases but when the layers are parallel to the frame. This means that even if the layers are not perfectly aligned forming an angle of 45°, the gain would not vary significantly. This result shows that the angle is not a critical parameter for the design. Similarly, from our studies, the strip-frame distance is not a critical parameter either. In practice, if the phone is dropped, in the worst case, the strip layers angle or the strip-frame distance would be slightly changed or shifted. This would have a very limited impact on the antenna performance.

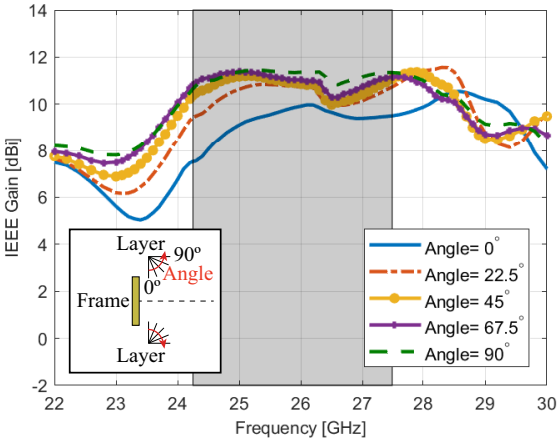

Fig. B.10: End-fire IEEE gain (in the $+x$ axis) of the array depending on the angle of inclination of the strip layers.

Effect of the gap between the strips

The spacing between the different metal strips is one of the most sensitive parameters. The inter-strip gap mainly affects the mutual coupling between strip elements, which contributes to providing a wider bandwidth with end-fire radiation pattern. It can be observed from Fig. B.11 that a stable high gain in the end-fire direction is obtained over a wide band by properly adjusting the inter-strip gap or coupling. Decreasing the gap shifts the resonant peaks down in frequency. Therefore, the width of the gap needs to achieve the maximum gain in the frequency band (shadowed area). Moreover, the gap needs to be wide enough to ensure the fabrication viability. Fig. B.11 shows that a gap of 0.15 mm provides the highest gain in all the frequency range. This gap width can be precisely obtained with the milling tools available.

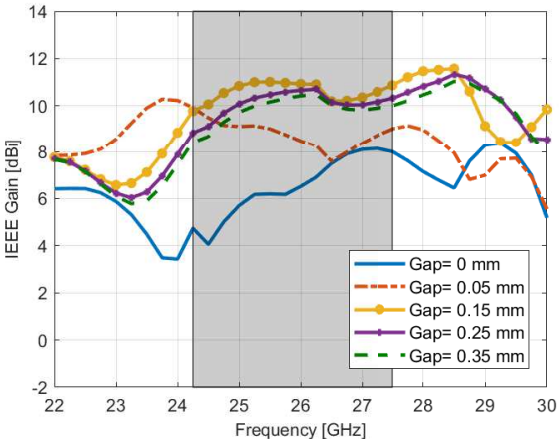

Fig. B.11: End-fire IEEE gain (in the $+x$ axis) of the array depending on the gap between the strips.

Effect of the strip length

A sweep in the metal strips length is presented in Fig. B.12 and it is also a critical design parameter.

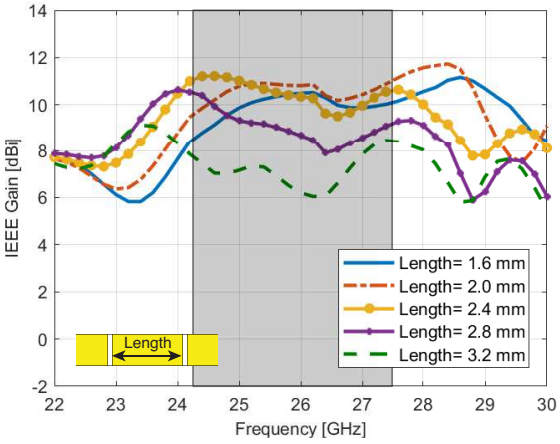

Fig. B.12: End-fire IEEE gain (in the $+x$ axis) of the array with two metal strip layers for different lengths as a function of the frequency.

The gap width is kept constant in the simulations, with a value of 0.15 mm. The tendency of the gain with the length is the opposite than with the gap. If the strip length is decreased, the gain curve in the $+x$ axis shifts to higher

frequencies. The reason for this behaviour is because the strips act as parasitic radiating elements. Thus, a higher gain in the operating band can be obtained with a shorter strip length. The length which provides the best gain in the end-fire direction ($+x$ axis), corresponds to 2.55 mm.

Effect of the frame-antenna distance

The mm-wave-antenna distance to the frame is another parameter that needs consideration. The clearance is a limitation in the design of mm-wave antennas. However, as Fig. B.13 shows, when the frame is too close to the antenna more energy is reflected and therefore, the gain is lower. If the top part of the antenna is located at 7 mm from the frame, the gain exhibits better performance in almost all the bandwidth. The metal strip layers are included in this study and all the elements are excited in phase. The proposed mechanism is valid for any clearance since the gain is higher with the strip layers than with just the frame (both at 2 and 7 mm away). Moreover, the gain enhancement increases even more with a smaller clearance (e.g. there is a 5 dB increase in a wide band with $d = 2$ mm compared with the solution without metal strips).

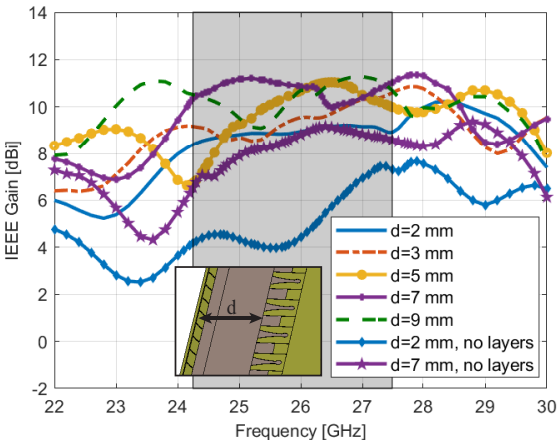

Fig. B.13: IEEE gain comparison for different distances from the mm-wave array to the frame.

To sum up, the gap width and strip length have been shown to be the most critical parameters in the design of the strip layers. The angle of the strip layers does not significantly modify the gain in the $+x$ axis. Finally, the strip layers improve the gain of the structure with respect of no layers at all, especially for smaller clearances.

IV Final design and performance

Through the parameter studies in the previous section, an optimized Vivaldi array with coupled metal strip layers is obtained. A complete design together with a low-frequency metal-frame antenna at sub-6 GHz is presented in this section. The authors would like to emphasize that the antenna-frame distance has been set to 7 mm because of design constraints of the low-frequency antenna. The proposed antenna and its prototype are shown in Fig. B.14 and Fig. B.15, respectively.

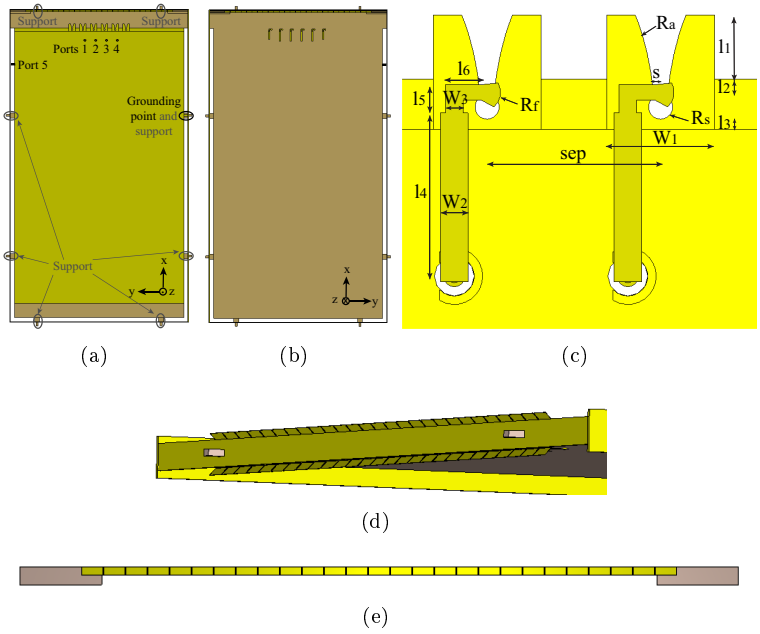

Fig. B.14: Proposed handset antenna. (a) Top view. (b) Bottom view. (c) Geometry of the Vivaldi antenna. (d) Zoomed view of the metal strip layers with their substrate hidden. (e) Coupled metal strip layer.

The proposed antenna is composed by a low-frequency metal-frame antenna and a mm-wave Vivaldi array with coupled metal strips. In order to attach the frame to the PCB in the precise location, protrusions etched in the PCB need to be inserted in the holes along the perimeter of the bezel as support spacer (see Fig. B.14 (a)). The supports are only made to facilitate the manufacturing of the prototype and it is not required in practical applications. Fig. B.15 (a) corresponds to the prototype without the coupled metal strip layers. Due to the tilted nature of the metal strips, a supporting foam is added to ensure the right

inclination (Fig. B.15 (b)) in the manual fabrication. The metal strip layers are pasted on the inner face of the foam support, as illustrated in Fig. B.15 (c), and then placed on both sides of the substrate, as Fig. B.15 (d) shows. The top part of the handset frame is slightly narrower than the rest, so the black sections at both sides of the top frame correspond to the strip layers (the strips are facing the foam). The pliability of the foam used to verify the proposed idea can be avoided in practical massive production, where the metal strips, mm-wave antennas, and low-frequency antenna would be integrated together with precision.

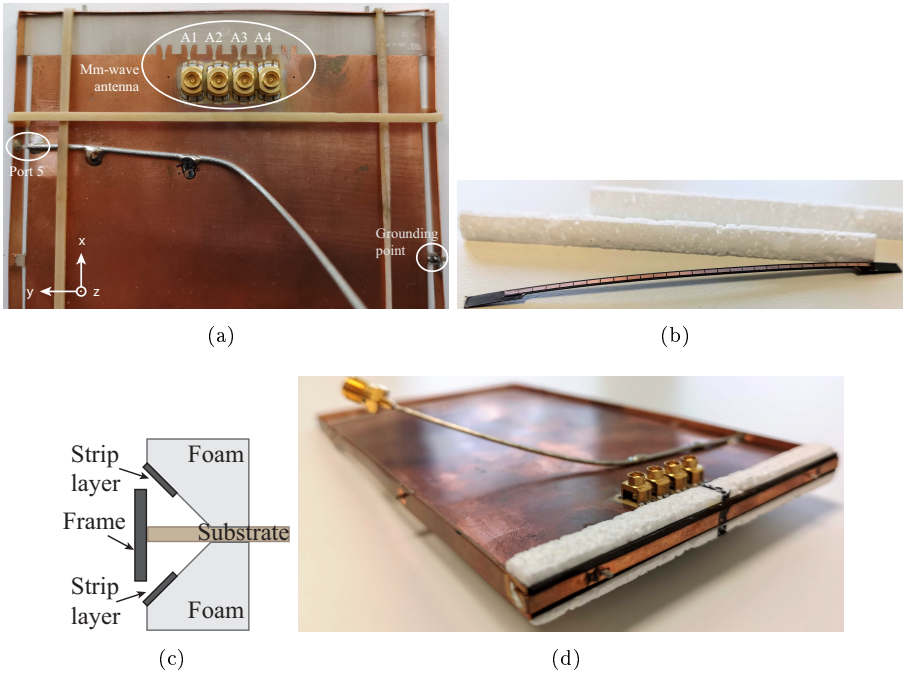

Fig. B.15: Antenna prototype. (a) Antenna without metal strip layers. (b) One of the metal strip layers and foam support structures. (c) Detailed scheme of the xz plane with the strip layers placement. (d) Final mounted structure.

A. Dual-loop metal-framed antenna

As shown in Fig. B.14 and Fig. B.15, the geometry of the low-frequency antenna is an unbroken metallic frame that covers the edges of the handset. The dual-loop antenna is formed when the ground plane of the PCB is combined with the rimmed-strip. The PCB is grounded on one of the protrusions on the right side, to form two loops. A 0.5λ mode is generated at 518 MHz and 985 MHz for the first and second loop, respectively. High-order resonant modes of

both loops are also excited, and their combination provides a wide impedance bandwidth. The design of the bezel antenna is based on the configuration in [21], but any other wideband metal-frame antennas can be employed. The width of the frame is 5 mm on the left, right and bottom sides, and 3 mm on the top side. The reason for making the top part narrower is to make sure that the highest point in the metal layers does not stand out from the 5 mm-wide frame. The thickness of the bezel is 0.3 mm. The total dimensions of the phone are 155.7 mm × 88.6 mm. The feeding (port 5) is a coaxial cable that connects the PCB with the frame (see Fig. B.15 (a)) and is located at 29 mm from the top part of the substrate.

The low-frequency antenna has been measured and the reflection coefficient is represented in Fig. B.16. The matching criterion for the low-frequency antenna is -6 dB. The measured impedance bandwidth covers the bands of 822-995 MHz, 1338-2321 MHz and 2429-2780 MHz. The bandwidth and radiation pattern of the metal frame antenna do not change when the metal strip layers are added. The simulated mutual coupling between the low-frequency antenna and the mm-wave array is below -40 dB in the low band and -32 dB in the operating mm-wave band. The total efficiency does not vary either with the coupled metal layers, and its value is 75 %, 85 % and 80 % for the respective bands. Therefore, the coupled metal strip layers do not change the performance of the low-frequency antenna.

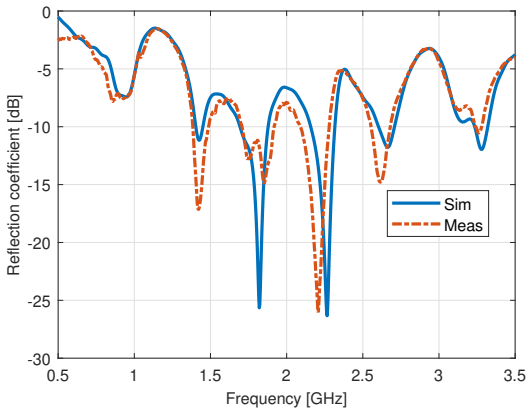

Fig. B.16: Comparison of the reflection coefficient of the low-frequency antenna.

B. Mm-wave Vivaldi array with coupled metal layers

The geometry of the mm-wave array is shown in Fig. B.14. The array is composed of 4 active Vivaldi elements and two dummy grounded elements to

ensure the similar boundary conditions for all the driven elements, and therefore match the edge elements in the array [22]. The Vivaldi element has overall dimensions of 3.31 mm × 3.61 mm, and it is implemented on Rogers RO3006 substrate with a dielectric permittivity of 6.15 and thickness of 0.64 mm. The Vivaldi antenna is fed by a microstrip line ended with a radial stub [23], but other feeding methods like SIW [24] can be employed. The coupled metal strip layers are etched on CuClad 217 substrate of $\epsilon_r = 2.17$ and thickness of 0.254 mm to facilitate the fabrication. As discussed in the previous section, the important design parameters are the gap of the metal strips (s_g) and the length (l_g). The tilting angle is fixed to (45°). The final dimensions of the antenna are listed in Table B.1. The measurements and simulated results of the integrated high-frequency array are discussed in the next paragraphs.

Table B.1: Dimensions of the Vivaldi antenna array and the coupled metal strip layers (unit: mm)

Parameter	Value	Parameter	Value
R_a	0.53	l_5	0.38
s	0.21	l_6	1.11
l_1	2.48	w_2	0.84
l_2	0.05	w_3	0.53
l_3	1.07	R_f	0.58
R_s	0.37	α_f	80°
sep	5.35	l_g	2.4
w_1	3.31	w_g	1
l_4	5.21	s_g	0.15

A comparison between simulated and measured S_{11} of the antenna without frame and metal strip layers and the complete designed structure is plotted in Fig. B.17 (a). The criterion considered for impedance matching at high frequencies is a reflection coefficient of -10 dB. Good agreement can be observed between simulations and measurements, where the measured bandwidth is only shifted 1.92 % to lower frequencies. The presence of the frame and metal strips layers reduces the impedance bandwidth around 2.69 %, but it is still wide enough to cover the 5G band n258 specified in 3GPP, as well as the n261 band [20]. Fig. B.17 (b) shows a comparison of the S-parameters of the antenna elements A1 and A2 (see Fig. B.15 (a)). The reflection coefficient of the antenna elements A3 and A4 is similar. The mutual coupling in the worst case (A2 with A3) is lower than -11 dB through the whole bandwidth.

The set-up for the radiation pattern measurement is shown in Fig. B.18. A horn is used as a probe in the measurement system. Each antenna element is measured at a time, with the rest of the elements loaded with 50 Ω. The measured antenna is located in a platform that can rotate 360°, and the mechanical

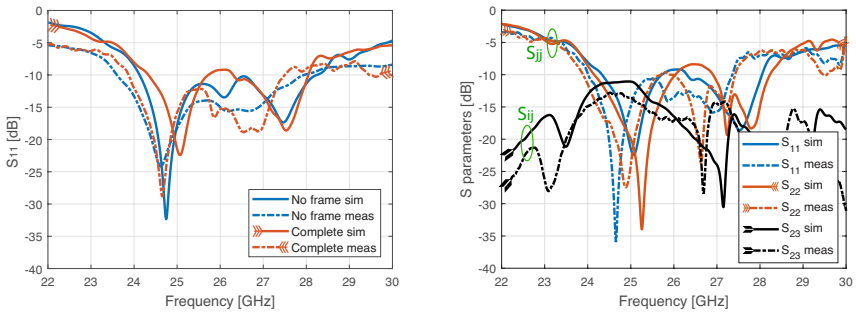

(a) (b)

Fig. B.17: S parameter comparison. (a) Reflection coefficient comparison between measurements and simulations of port 1. (b) Comparison between the S-parameters of measurements and simulations of the final design.

arm, where the horn is fixed, can move from $\theta = 0°$ to 135°. The radiation pattern in the H-plane has been plotted in Fig. B.19 for the elements A1 and A2 (antenna numbering is specified in Fig. B.15 (a)). The radiation patterns point to the $+x$ axis, which means that the antenna has end-fire radiation. The shape of the measured radiation patterns is similar to the simulations. The side lobe on the non-metal side ($\theta = -180°$) is a bit high, but it is due to the shape of the radiation pattern of the Vivaldi element, instead of the metal strip layers. The representation in the E-plane is shown in Fig. B.20. A good agreement is found between measurements and simulations. However, the main lobe direction has been slightly shifted from the $+x$ axis. Therefore, the cuts represented do not include the maximum gain value. For that reason, in the measurements, the realized gain is slightly lower than the simulated at 26 GHz.

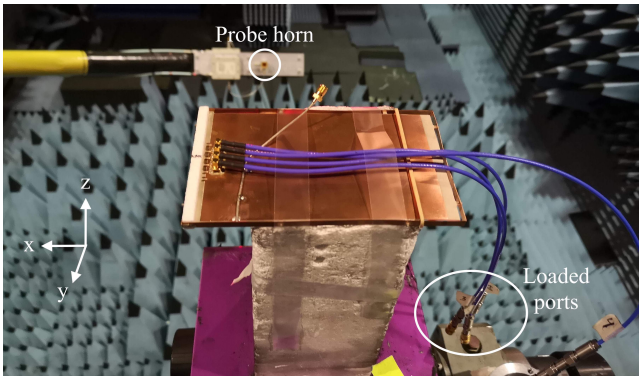

Fig. B.18: Measurement set-up in the anechoic chamber.

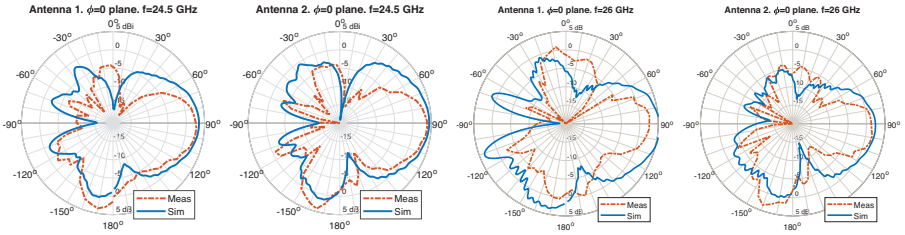

(a) (b) (c) (d)

Fig. B.19: Comparison of the radiation pattern of the elements in the H-plane at 24.5 GHz and 26 GHz.

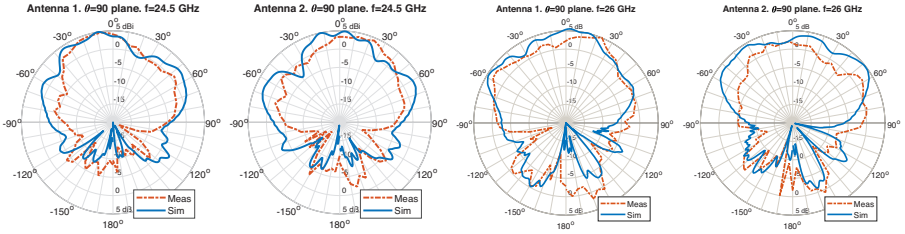

(a) (b) (c) (d)

Fig. B.20: Comparison of the radiation pattern of the elements in the E-plane at 24.5 GHz and 26 GHz.

Fig. B.21 represents the realized gain in the end-fire direction ($+x$ axis) as a function of the frequency. All the elements have been plotted individually and also the array is excited in phase. The realized gain is higher than 8 dBi in the whole the frequency range.

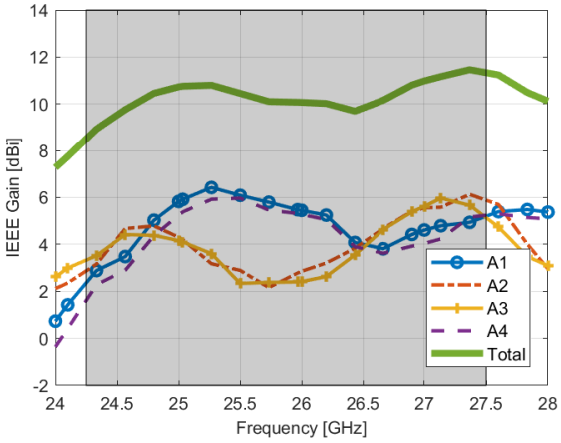

Fig. B.21: Simulated realized gain in the end-fire direction ($+x$ axis), of all the antenna elements and in-phase combination of the array, in the frequency range.

The resulting simulated beam-steering envelope is shown in Fig. B.22. In order to obtain the envelope, the maximum realized gain of 13 beams is plotted at each angle of ϕ. The progressive phase shifts generated to obtain those beams are $\pm 45°$, $\pm 60°$, $\pm 90°$, $\pm 105°$, $\pm 120°$ and $\pm 135°$. The array can scan $\pm 60°$ with an average gain higher than 7 dBi for the entire frequency range.

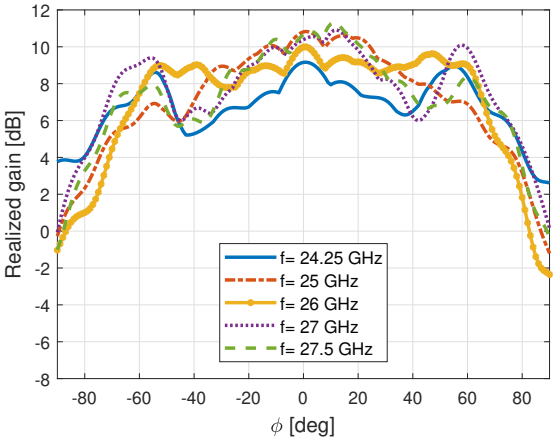

Fig. B.22: Simulated realized gain beam-steering envelope.

V Conclusion

Mm-wave horizontally-polarized end-fire antenna arrays face a degradation of the main beam when the metal frame of a phone is placed. In order to overcome this obstruction, coupled metal strip layers have been proposed to be located at both sides of the frame edge. The coupling between the frame and the tilted layers allows them to act as a relay, re-radiating the energy to the desired direction. It has been shown that these parasitic strips would not affect antennas with vertical polarization.

The effect of several parameters in the radiation pattern has also been studied, such as the angle of the strip layers, the gap between the strips, the strip length and the antenna-frame distance. The most critical parameters have been shown to be the gap and the strip length. The introduced metal strip layers have been shown to be able to cooperate with microstrip patches and Vivaldi antenna elements. For the final design, the mm-wave array is built of four Vivaldi elements since they provide a robust radiation pattern besides their broad bandwidth. The array is able to steer the beam from $\phi = \pm 60°$, with a realized gain higher than 7 dBi. The mm-wave array has been combined with a double-loop low-frequency antenna to present a complete prototype of a 5G-enabled handset. The low-frequency antenna serves as well as the metal frame of the terminal.

Measured results have verified the simulations. The resulting mm-wave array is matched between 24 and 27.5 GHz. The coupled metal strip layers successfully point the beam in the end-fire direction, as the radiation pattern from the antenna elements shows. Good agreement between the simulated and measured results is also found with the low-frequency antenna, that covers the frequency bands 822-995 MHz and 1338-2780 MHz.

Acknowledgment

The authors would like to thank the invaluable help of Ben Kryer and Peter Jensen with the antenna manufacturing, Kristian Bank and Kim Olesen for the chamber set-up, and Igor Syrytsin and Carla Di Paola for their help with the measurements.

References

[1] W. Hong, K.-H. Baek, Y. Lee, Y. Kim, and S.-T. Ko, "Study and prototyping of practically large-scale mmwave antenna systems for 5G cellular devices," *IEEE*

Communications Magazine, vol. 52, no. 9, pp. 63–69, 2014.

[2] T. S. Rappaport, S. Sun, R. Mayzus, H. Zhao, Y. Azar, K. Wang, G. N. Wong, J. K. Schulz, M. Samimi, and F. Gutierrez, "Millimeter wave mobile communications for 5G cellular: It will work!" *IEEE Access*, vol. 1, pp. 335–349, 2013.

[3] Z. Pi and F. Khan, "An introduction to millimeter-wave mobile broadband systems," *IEEE communications magazine*, vol. 49, no. 6, 2011.

[4] J. Lee, E. Tejedor, K. Ranta-aho, H. Wang, K.-T. Lee, E. Semaan, E. Mohyeldin, J. Song, C. Bergljung, and S. Jung, "Spectrum for 5G: Global status, challenges, and enabling technologies," *IEEE Communications Magazine*, vol. 56, no. 3, pp. 12–18, 2018.

[5] S. Zhang, I. Syrytsin, and G. F. Pedersen, "Compact beam-steerable antenna array with two passive parasitic elements for 5G mobile terminals at 28 ghz," *IEEE Transactions on Antennas and Propagation*, pp. 1–1, 2018.

[6] Y. Li and Z.-C. Hao, "A wideband switched beam antenna for full 360 coverage," in *2017 Sixth Asia-Pacific Conference on Antennas and Propagation (APCAP)*. IEEE, 2017, pp. 1–3.

[7] J. Bang, Y. Hong, and J. Choi, "Mm-wave phased array antenna for whole-metal-covered 5G mobile phone applications," in *Antennas and Propagation (ISAP), 2017 International Symposium on*. IEEE, 2017, pp. 1–2.

[8] Z. Ying, K. Zhao, T. Bolin, J. Helander, D. Sjöberg, S. He, A. Scannavini, L. J. Foged, and G. Nicolas, "Study of phased array in UE for 5G mm wave communication system with consideration of user body effect," in *2016 10th European Conference on Antennas and Propagation (EuCAP)*, April 2016, pp. 1–2.

[9] H. Xia, J. Lei, L. Meng, and G. Yang, "Design and analysis of a compact reconfigurable phased antenna array with 3D coverage for 5G applications in portable devices," in *2016 Progress in Electromagnetic Research Symposium (PIERS)*, Aug 2016, pp. 2459–2463.

[10] N. Ojaroudiparchin, M. Shen, S. Zhang, and G. F. Pedersen, "A switchable 3-D-coverage-phased array antenna package for 5G mobile terminals," *IEEE Antennas and Wireless Propagation Letters*, vol. 15, pp. 1747–1750, 2016.

[11] M. Stanley, Y. Huang, H. Wang, H. Zhou, A. Alieldin, and S. Joseph, "A capacitive coupled patch antenna array with high gain and wide coverage for 5G smartphone applications," *IEEE Access*, vol. 6, pp. 41 942–41 954, 2018.

[12] S. Zhang, X. Chen, I. Syrytsin, and G. F. Pedersen, "A planar switchable 3-D-coverage phased array antenna and its user effects for 28-GHz mobile terminal applications," *IEEE Transactions on Antennas and Propagation*, vol. 65, no. 12, pp. 6413–6421, 2017.

[13] I. Syrytsin, S. Zhang, G. F. Pedersen, and A. Morris, "Compact quad-mode planar phased array with wideband for 5G mobile terminals," *IEEE Transactions on Antennas and Propagation*, 2018.

[14] J. Helander, K. Zhao, Z. Ying, and D. Sjöberg, "Performance analysis of millimeter-wave phased array antennas in cellular handsets," *IEEE Antennas and wireless propagation letters*, vol. 15, pp. 504–507, 2016.

[15] I. Syrytsin, S. Zhang, G. Pedersen, K. Zhao, T. Bolin, and Z. Ying, "Statistical investigation of the user effects on mobile terminal antennas for 5G applications," *IEEE Transactions on Antennas and Propagation*, 2017.

[16] M. M. S. Taheri, A. Abdipour, S. Zhang, and G. F. Pedersen, "Integrated millimeter-wave wideband end-fire 5G phased array and low-frequency 4G LTE antenna in mobile terminals," 2019.

[17] M. Keshavarz Hedayati and M. Elbahri, "Antireflective coatings: Conventional stacking layers and ultrathin plasmonic metasurfaces, a mini-review," *Materials*, vol. 9, no. 6, p. 497, 2016.

[18] B. Yu, K. Yang, G. Yang *et al.*, "A novel 28 GHz beam steering array for 5G mobile device with metallic casing application," *IEEE Transactions on Antennas and Propagation*, vol. 66, no. 1, pp. 462–466, 2018.

[19] J. Bang and J. Choi, "A SAR reduced mm-wave beam-steerable array antenna with dual-mode operation for fully metal-covered 5g cellular handsets," *IEEE Antennas and Wireless Propagation Letters*, 2018.

[20] 3GPP, "User Equipment (UE) radio transmission and reception; Part 2: Range 2 Standalone (Release 15)," 3rd Generation Partnership Project (3GPP), Technical Specification (TS) 38.101-2, 06 2018, version 15.0.0.

[21] Y.-L. Ban, Y.-F. Qiang, Z. Chen, K. Kang, and J.-H. Guo, "A dual-loop antenna design for hepta-band WWAN/LTE metal-rimmed smartphone applications," *IEEE Transactions on Antennas and Propagation*, vol. 63, no. 1, pp. 48–58, 2015.

[22] E. Holzman, "On the use of dummy elements to match edge elements in transmit arrays," in *Phased Array Systems & Technology, 2013 IEEE International Symposium on*. IEEE, 2013, pp. 549–552.

[23] J. H. Shafieha, J. Nourinia, and C. Ghobadi, "Probing the feed line parameters in vivaldi notch antennas," *Progress In Electromagnetics Research*, vol. 1, pp. 237–252, 2008.

[24] P. Liu, X. Zhu, X. Wang, and L. Tian, "A SIW-based vivaldi array antenna for 5G wireless communication systems," in *Antennas and Propagation & USNC/URSI National Radio Science Meeting, 2017 IEEE International Symposium on*. IEEE, 2017, pp. 529–530.

Paper C

Mm-Wave Beam-Steerable Endfire Array Embedded in Slotted Metal-Frame LTE Antenna

Rocío Rodríguez-Cano, Shuai Zhang, Kun Zhao and Gert Frølund Pedersen

The paper has been published in
IEEE Transactions on Antennas and Propagation Vol. 68, Issue 5,
pp. 3685–3694, 2020.

Abstract

In this paper, a new principle to overcome the blockage of metallic frames in mobile terminals to endfire millimeter-wave (mm-wave) arrays is proposed. The obstruction is solved by etching several slots in the top part of the frame. It is shown that the slots in the handset frame can furthermore enhance the beam-steering gain of a mm-wave bow-tie array. A very small array-frame distance can also be realized without degrading much the array performance. Several considerations in the slot design are assessed first. A prototype of the PCB and frame has been built and the results show that the array is matched in the desired frequency bands of 24.25-27.5 GHz and 27.5-28.35 GHz. The mm-wave array can scan 80 degrees in the endfire direction, and the realized gain obtained is higher than 7 dBi in the operating frequency bands. At the same time, the frame performs as a sub-3 GHz dual-loop antenna. The covered bands are 760-980 MHz and 1240-2870 MHz.

I Introduction

The inclusion of the millimeter-wave (mm-wave) bands in the fifth generation of mobile communication (5G) spectrum, has prompted the appearance of higher gain antenna systems in mobile terminals [1–4]. Different antenna arrays have been proposed in the literature to cover the new frequency bands [5–11]. The increasing number of antennas in handsets provides challenges in terms of the inclusion of these new antennas.

The embedding of mm-wave antenna systems in antennas in the sub-6 GHz is a good solution for tight space constraints. Nevertheless, since the wavelength of the mm-wave array is smaller, the antennas are more sensitive to the blockage of any metallic structures placed nearby. In [12], the mm-wave array is embedded in a planar inverted F-antenna (PIFA) that covers the sub-3 GHz band. The solution proposed to prevent the obstruction from the PIFA on the mm-wave antenna is to add a layer of grating strips between the two antennas, at a distance of $\lambda/4$ from the PIFA, so that the reflections cancel out. However, this solution does not consider the metallic frame of the handsets, which is commonly used in the industry, but a planar structure. Two 4G monopoles have been embedded in a mm-wave slot array in [13], but the metallic frame is not considered in the design. In [14], a mm-wave antenna module is embedded in the metal rim of the handset, that is utilized as a LTE antenna. A 25 mm $\times$ 10 mm $\times$ 6 mm window is cut from the metal rim for the mm-wave module. Since the array is delimited by the metal frame, the beam-steering range is limited to $\pm 25°$. In [15], a mm-wave array is embedded in a metal-frame an-

tenna, which covers some of the sub-3 GHz bands. The beam can scan ±60°, with a gain higher than 10 dBi in all the frequency range. Several solutions of slot arrays etched on the handset frame are proposed in [7,16–18]. However, in these cases, the co-design of the metal-frame antenna and mm-wave array would become more complex, since the feeding networks of the mm-wave antenna have to connect the metal frame with the ground plane of the phone. This significantly changes the modes of the low-frequency antenna and thereby its performance.

In this paper, a dual-element phased array is proposed to cover the 5G bands n258 (24.25-27.5 GHz) and n261 (27.5-28.35 GHz) [19]. The proposed design presents a solution to overcome the frame blockage of horizontally-polarized endfire mm-wave antennas, that achieves high gain and large beam-steering range. The mm-wave array is embedded in a slotted-metal frame antenna, that enhances the gain of the 5G array. With higher gain, the number of driven antennas can be reduced, which decreases the complexity of the array, since fewer phase shifters and other components are needed. As the slots are fed by the electromagnetic coupling from mm-wave array to the frame, the complexity of the embedding in the low frequency antenna is significantly reduced. Simulations are carried out by CST Microwave Studio 2019. The novelty and contribution of this paper are summarized and listed as follows:

1. The co-design of the low-frequency and mm-wave antennas is simple after the embedding, which is because the slots in the frame are fed by the coupling of the mm-wave array.

2. Improvement of the mm-wave array gain after the embedding, which allows employing less active elements in the 5G mm-wave array.

3. The proposed concept is valid for very wide metal frames and small clearances. Moreover, the performance is robust to different antenna-frame distances.

The manuscript is organized as follows: the proposed design is specified in Section II. Section III describes the principle proposed to overcome the frame blockage to endfire mm-wave antennas. Design considerations are analyzed in Section IV to determine the final configuration, such as slot shape, number of slots, the separation between the slots, antenna-frame distance and number of active elements. The performance of the final design is shown in Section V. In Section VI, a comparison between the state of art and the solution proposed in this paper is presented. Finally, conclusions are given in Section 4.

II Proposed Design

The proposed design consists of a mm-wave phased array embedded in a slotted metal-frame antenna that covers the sub-3 GHz bands. The antennas are represented in Fig. C.1. The mm-wave antenna is etched on Rogers RO4350B substrate of thickness 0.254 mm, and dielectric permittivity of 3.48. The chosen geometry of the mm-wave array is a quad-element antipodal bow-tie array, with only 2 active elements, fed by coaxial cables. Bow-tie antenna elements have been selected since they present a wide impedance bandwidth [20]. The dummy elements located at both sides of the mm-wave array are grounded. Their function is to provide similar boundary conditions for the 2 active elements. They have been optimized to offer the highest endfire gain without degrading the impedance matching of the antenna. The metal frame encloses the PCB, with a thickness of 0.3 mm and overall dimensions of 128 mm $\times$ 69.6 mm $\times$ 7 mm. The design of the bezel antenna is based on [21], that provides small ground clearance as a result of the use of lumped components. The grounding point and feeding of the frame antenna are represented in Fig. C.1(b). The metallic part of the PCB is separated 2 mm from the frame on the sides, 2.78 mm on the top and 5.22 mm on the bottom. The PCB ground distance to the frame (2.78 mm) is defined by the design of the low-frequency antenna. The distance from the top part of the mm-wave antenna to the frame is obtained in Sec. D. and has a value of 0.5 mm. The slots etched on the top part of the frame are represented in Fig. C.1(c). The slots etched on the frame barely modify the performance of the low-frequency antenna. The design parameters of the bow-tie mm-wave array and the slots etched on the frame are listed in Table C.1.

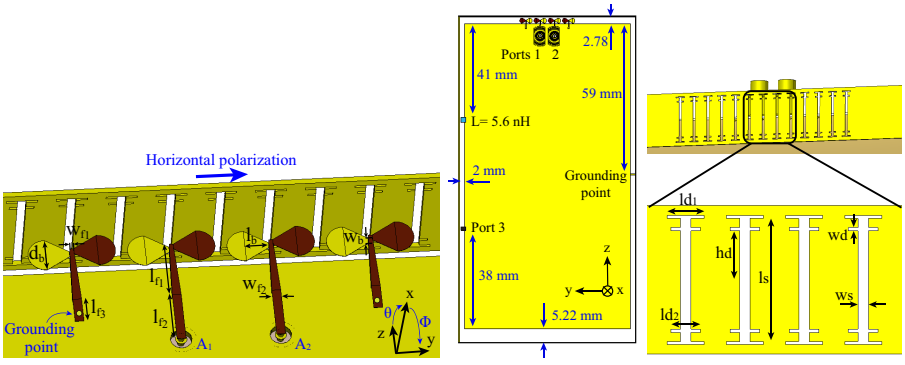

Fig. C.1: Proposed embedded design. The substrate is delimited by the frame and is hidden in the figures. (a) Mm-wave array and top part of the frame with the slots etched. (b) Handset view. (c) Front view of the frame. Details of the slotted frame.

Table C.1: Dimensions of the Bow-tie Array and the Slots Etched on the Metal Frame (Unit: mm)

Parameter	Value	Parameter	Value
l_b	1.33	l_s	5.80
w_b	0.33	w_s	0.50
d_b	2.00	h_d	2.32
l_{f1}	3.45	l_{d1}	1.75
l_{f2}	3.00	l_{d2}	1.40
l_{f3}	1.50	w_d	0.15
w_{f1}	0.22	w_{f2}	0.50

III Operating Principle

Previous studies from the authors show that the radiation patterns of endfire mm-wave arrays with vertical polarization are barely influenced by the metallic frame. On the other hand, it is critical for arrays with horizontal polarization [15]. For that reason, the focus of this paper is on the reduction of the frame blockage for endfire arrays with horizontal polarization. Please note that for convenience we refer to endfire direction as $+z$ axis, broadside as x axis, horizontal polarization with the E-field amplitude varying in the direction of the y axis and vertical polarization, in the direction of the x axis. The coordinate system can be found in Fig. C.1(a).

As detailed in Section II, the proposed mm-wave array is composed of two end-fire antipodal bow-tie elements and two grounded dummy elements on the sides [see Fig. C.1(a)]. Since the mm-wave antenna array has horizontal polarization, it excites horizontal currents on the frame, as shown in Fig. C.2(a) and the radiation pattern is degraded. The resulting radiation pattern is mainly broadside, instead of endfire [Fig. C.3]. In Fig. C.2(a) the surface currents created by the antenna on the frame are represented. Therefore, if vertical slots are etched on the frame [see Fig. C.1(c)], they would be fed by these currents and allow the mm-wave array radiate in the desired direction. The surface currents for the slotted frame are plotted in Fig. C.2(b). It can be seen that the current concentration is higher around the slots. To demonstrate that the array is radiating in the correct direction, Fig. C.3 shows the in-phase radiation pattern at the $\Phi = 0°$ cut of the array. This figure represents the impact of the frame on conventional endfire antennas with horizontal polarization. IEEE gain is plotted to exclude the mismatching loss of the different structures. It is defined as the antenna directivity plus the radiation efficiency (in logarithmic scale). When there is no frame placed in front of the antenna, the main lobe of the array points to the endfire direction, with a value of 6.5 dBi. In the

presence of the frame, the radiation pattern becomes broadside, with gain in the endfire direction of -5 dBi. For that reason, it is crucial to consider the impact of the frame in the design of horizontally polarized endfire mm-wave antennas. The radiation pattern of the solution presented in this paper also appears in Fig. C.3. The slots etched on the top part of the frame not only overcome the blockage but make the radiation pattern to be more directive, with a gain of 7.7 dBi. The reason the main beam becomes more directive can be better understood by plotting the E-field. The instantaneous E-field in a longitudinal cut is represented in Fig. C.4. When no frame is blocking the main beam of the array, the field distribution is larger around the mm-wave array. The wavefront propagates in the direction of the $+z$ axis. In the case of the unmodified frame, i.e, no slots [Fig. C.4(b)], it can be seen that the electric field is blocked by the frame and the wavefront is propagating backward ($-z$ axis). However, the slots etched on the frame re-radiate the coupled energy from the bow-tie antenna, which increases the antenna aperture and leads to higher gain. Therefore, the E-field increases in the endfire direction [see Fig. C.4(c)] and the wavefront is more directive than the case with no frame. The proposed solution can also be identified as the diffraction of curved wavefront on a metal frame with multiple slits. Since the mm-wave array is located 0.5 mm away from the frame, it corresponds to the Fresnel regime.

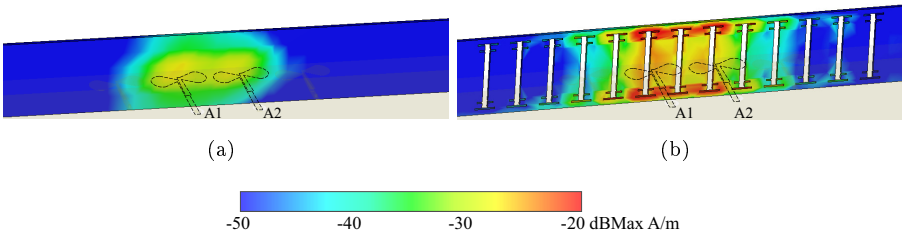

Fig. C.2: Surface current on the top frame for the in-phase combination at 26 GHz. (a) No slots. (b) With slots.

IV Design considerations

In order to reveal the critical design parameters and demonstrate the robustness of the proposed design with different design scenarios, some configurations are assessed in this section. The considered parameters are the slot shape, number of slots, separation between the slots, antenna-frame distance and number of active elements. Since some of the parameters in the studies may change the impedance matching of the array, IEEE gain is represented to exclude the mismatch losses.

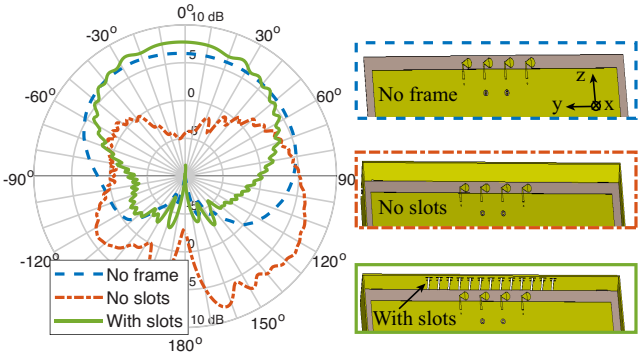

Fig. C.3: IEEE gain radiation pattern of the in-phase array combination at 26 GHz for the $\Phi = 0°$ cut.

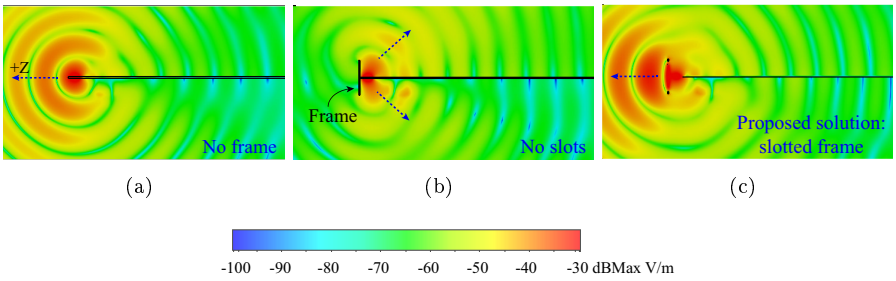

Fig. C.4: Instantaneous E-field distribution cut in the XZ plane of the in-phase combination at 26 GHz. (a) No frame. (b) No slots. (c) With slots.

A. Effect of the slot shape

As described in Section III, horizontal currents are excited on the frame by the mm-wave antenna. Therefore, in order to couple with the horizontal polarized E-field and re-radiate it, vertical slots are etched on the frame. To maximize the gain out of the mm-wave array in the frequency bands, the dimensions of the slots need to be assessed. The length of the slot determines the resonant frequency. To obtain the optimum result, the resonant frequency of the slot should be in the middle of the frequency range of the antenna array. However, the width of the frame is a constraint, in this case, a value of 7 mm is chosen to adapt it to the width of the current terminals. For that reason, the slot cannot be enlarged progressively in a straight line and a dumbbell shape has been adopted [see Fig. C.5]. As shown in the figure, the shape referred to as double dumbbell can further increase the gain of the array in the desired frequency bands and has been chosen for the final design. Fig. C.6 shows the radiation pattern comparison at 1.5 GHz between the different slot shapes and no slots

on the frame. It can be seen that the slot shape has very limited impact on the performance of the LTE antenna.

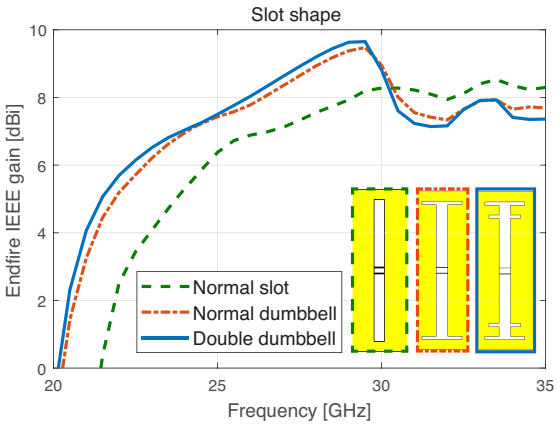

Fig. C.5: IEEE gain in the endfire direction according to the slot shape.

B. Number of slots

The number of slots etched on the frame has a strong impact on the gain in the endfire direction, as it can be seen in Fig. C.7(a). The focus in this subsection corresponds to the design with two active elements and two dummy elements. The number of slots could straightforwardly be increased if more active elements are employed. In the case of 9 slots, the aperture of the slot array is the same as the mm-wave array. The gain of the mm-wave array without frame has been plotted as a reference, and the configuration with only 5 slots can already improve that performance. The gain in the endfire direction does not differ much when the number of slots is 7 or higher, but the radiation pattern becomes broadside when no slots are etched on the frame, as shown in Fig. C.7(b). In terms of impedance mismatching, the configuration with frame with no slots is mismatched in all the operating bandwidth, since the majority of the radiation reflects back to the antenna. From 5 slots onward, the mm-wave array is matched below -10 dB from 24 to 29 GHz. In order to determine the number of slots which provides the best performance, the gain has also been plotted as a function of the beam-steering angle in Fig. C.7(c). The figure provides the beam-steering envelope of a total of 12 beams. The phase step applied to get the different beams is 30°. The number of slots is also a critical parameter to achieve high beam-steering gain owing to the fact that, if the main beam points towards a place on the frame with no slots, the radiation would reflect back. Besides, it is important to have high gain with small variations between the beams pointing to different angles to reduce the complexity of the

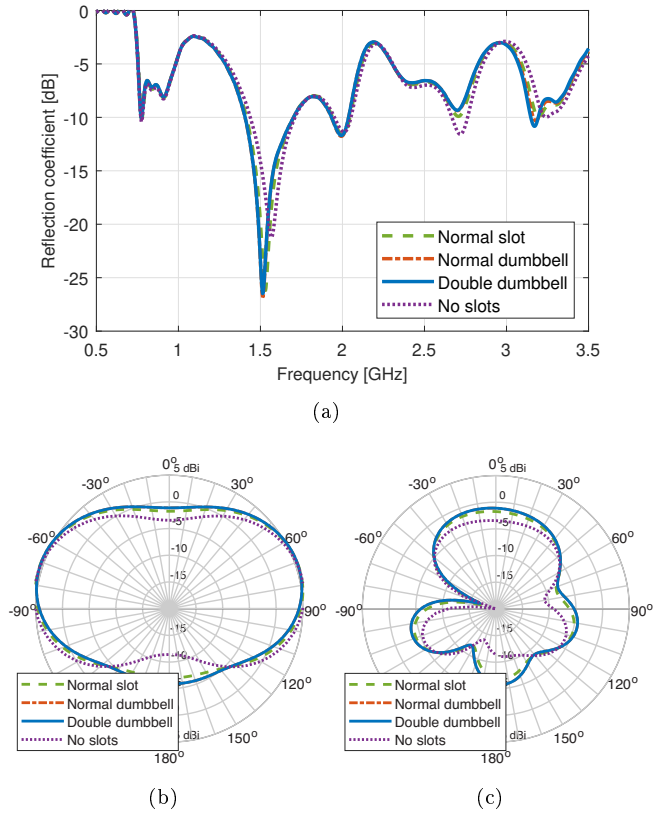

Fig. C.6: Effect of the slot shape in the S parameters and the radiation pattern of the metal-frame antenna at 1.5 GHz. (a) Reflection coefficient. (b) Radiation pattern at $\Phi = 0°$ cut. (c) Radiation pattern at $\Phi = 90°$.

system. Moreover, high gain antennas have narrow beams, which are steered to cover the upper part of the sphere. Therefore, to determine the number of etched slots, it is necessary to consider the maximum beam-steering angle. The beam-steering envelope of these configurations is represented in Fig. C.7(c) at 24.25 GHz, as the lower frequency band is the most sensitive. If only 9 slots are etched on the metal frame, the gain envelope is only higher than 7 dBi for $\theta = \pm 20°$ at 24.25 GHz. This is due to a not large enough slot aperture. When 13 slots are added, the gain envelope is flatter, with a beam-steering range of $\pm 40°$. For 15 slots, the scanning range could be enlarged, but with a gain lower than 7 dBi, which is the target. The configuration chosen for the final design is the one with 13 slots.

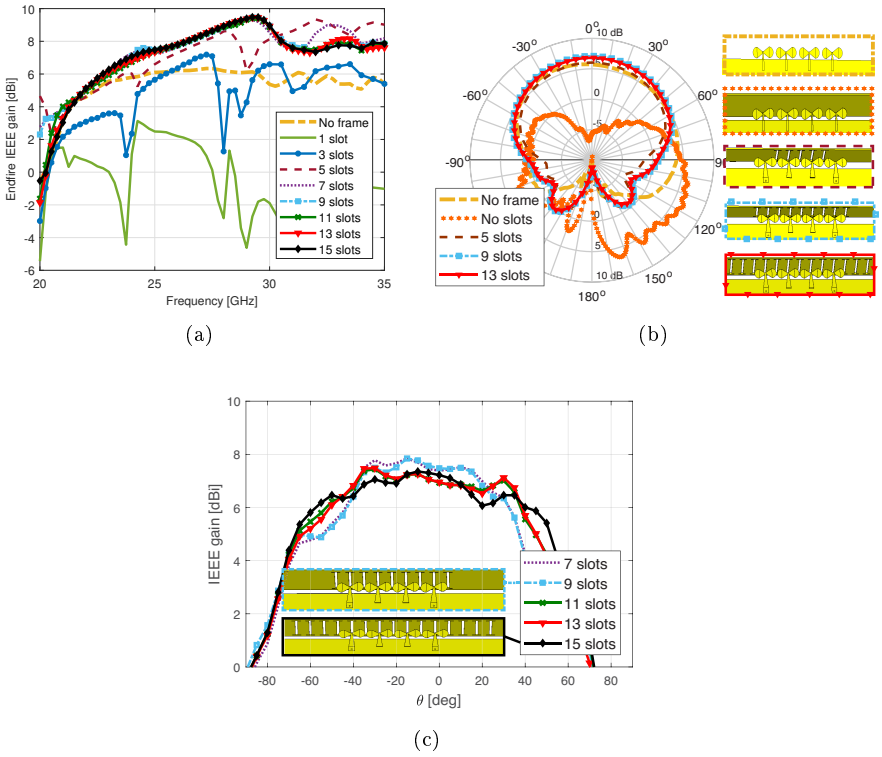

Fig. C.7: (a) IEEE gain as a function of the frequency depending on the number of slots etched on the frame. The gain of the array with no frame is also compared. (b) IEEE gain radiation pattern at 24.25 GHz for $\Phi = 0°$ cut. (c) IEEE gain beam-steering envelope at 24.25 GHz.

C. Separation between the slots

The separation between the slots is essential to maximize the radiated gain. The main beam of the antenna has endfire direction, hence the maximum value of the current excited on the frame is aligned with the center of the antenna, as shown in Fig. C.2(a). For that reason, the separation of the slots depends on the separation between antenna elements (*sep*), which corresponds to $0.486\lambda_0$. The performance of several configurations is represented in Fig. C.8. In the case of $0.375 \times sep$ ($0.182\lambda_0$) a distance of only 0.35 mm separates the slots from touching each other. The reflection coefficient shows that the antenna array is only matched when the separation between the slots is smaller than $0.5 \times sep$ ($0.243\lambda_0$). This configuration corresponds to having slots aligned with the center of every antenna and also in between the antenna elements, as shown in Fig. C.8 (a). The separation between the slots is frequency dependent. The

closer the separation between the slots, the easier higher frequencies (small wavelengths) propagate through the frame. As the separation between the slots increases, the endfire gain curve shifts to lower frequencies. In some of the larger separations, the gain can reach higher values but not throughout the whole frequency range and, besides, the impedance matching does not fulfill the expected -10 dB criterion. The value that provides an endfire gain of more than 7 dBi throughout the frequency band and a good impedance matching is $0.5 \times sep$ ($0.243\lambda_0$).

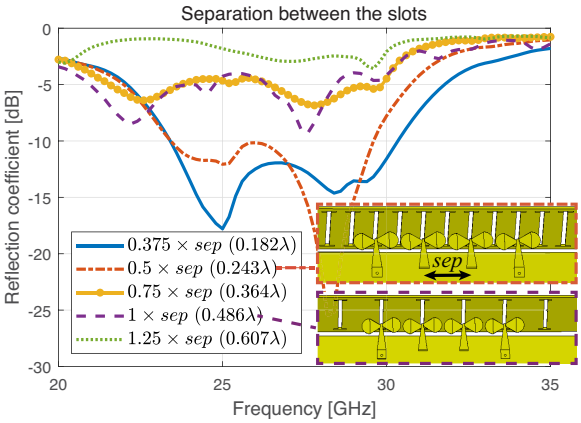

(a)

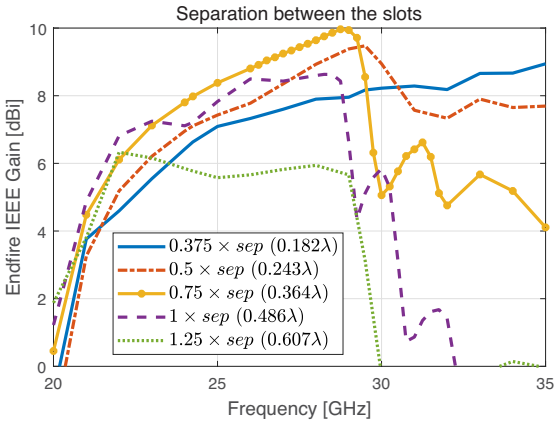

(b)

Fig. C.8: Effect of the separation between the slots. (a) Reflection coefficient. (b) IEEE gain in the endfire direction.

D. Antenna array-frame distance

In order to illuminate the slots etched on the frame, the distance from the top of the antenna to the frame needs to be small. However, the closer the antenna is located to the frame, the more radiation would be reflected. In Fig. C.9, the reflection coefficient and the IEEE gain in the endfire direction are represented. The gain maximum shifts to lower frequencies when the distance to the frame is enlarged. As the distance to the frame gets larger, the gain increases in the lower part of the frequency band but the impedance bandwidth is reduced. Due to this trade-off, a distance to the frame of 0.5 mm has been chosen for the final design. Even though there are variations in the results, the overall performance is very robust to the antenna-frame distance, which is an advantage in the fabrication process.

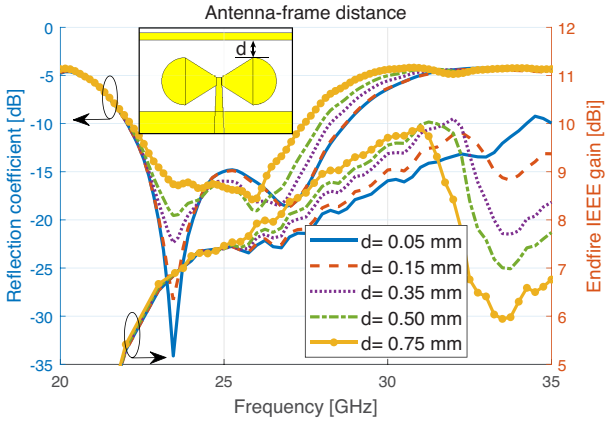

Fig. C.9: Effect of the distance of the antenna to the frame, for both reflection coefficient and IEEE gain in the endfire direction.

E. Number of active elements

At the 3GPP TR 38.817-01 specification for UE RF aspects in new radio (NR) [19], the minimum effective isotropic radiated power (EIRP) requirements for handsets (power class 3) in the mm-wave bands are based on an assumption of 4 active elements antenna arrays. This does not mean that the mm-wave arrays for terminals are required to have 4 elements, but gives an estimation of the number of antennas that are feasible to meet the minimum power required. Therefore, if an array with less active antennas can meet the requirements, it will be beneficial to reduce the size of the front-end module.

In this subsection, the advantages and disadvantages of adding two more

active elements to the design are discussed. The design presented throughout the paper corresponds to 4 elements: 2 active and 2 dummy. As the slotted frame design can improve the array gain, it provides an opportunity to reduce the number of active elements. The idea is to compare it with the design of 4 antennas: 4 active elements without frame, since the gain achieved is similar. From the array point of view, two more elements provide higher gain and wider scanning range. The beam-steering envelope at 26 GHz is plotted in Fig. C.10, with a gain increase of around 0.5 dB. From the front-end point of view, doubling the number of antennas would increase the complexity and cost of the system. On the other hand, the array gain would be further increased by double the number of elements and the power requirements of each antenna branch would be lower. If the power on the branch can be lower, the specifications of the power amplifier would be more relaxed, increasing the number of choices in the semiconductor technologies [22]. The 5G evaluation requirement for antenna arrays is defined as the EIRP spherical coverage (for the frequency range 2) [19]. The EIRP depends on two factors: the array antenna gain and the total radiated power. Even though the proposed design uses a smaller number of antenna ports, it can actually increase the antenna gain of the array after the embedding in the slotted-frame. For that reason, the overall array gain is not affected dramatically in the end, as represented in Fig. C.10. On the other hand, the total radiated power can be affected due to the smaller number of antenna ports. The reason is that one of the most common architectures in mm-wave consists of having a power amplifier (PA) connected to each antenna port. Therefore, the number of power amplifiers might be reduced with a smaller number of antenna ports. Such RF architecture allows low-power and low-cost design of PAs to be used for handsets, for example, a CMOS type of PA [23]. One way to address this issue is to use a higher output power PA when the number of antenna ports is reduced, e.g. III-V type semiconductor PA, which could offer a higher output power and leverage total radiated power. Therefore, the number of elements will depend on the design of the whole front-end, but our proposed method provides an opportunity to reduce the number of antenna elements with a certain EIRP target.

V Results and Discussions

A prototype of the designed antenna has been fabricated to verify the simulation results. The dielectric tabs, that can be seen in Fig. C.11 coming out of the frame, are made to hold the PCB in place, at the center of the frame. Their length and width are optimized to not interfere with the beam in the directions of maximum scan angle. A comparison between the measurements and simulations is assessed in the next paragraphs.

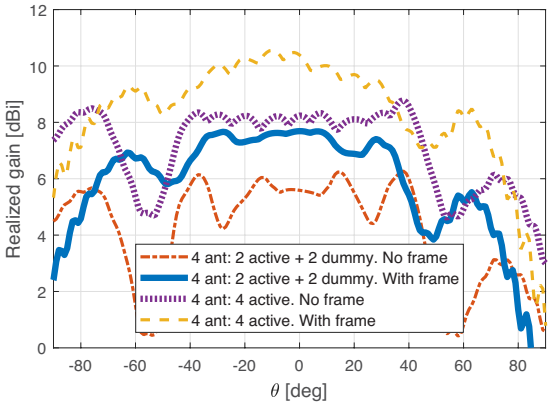

Fig. C.10: Simulated beam-steering realized gain envelope comparison of the 2- and 4-element arrays with and without slotted frame at 26 GHz.

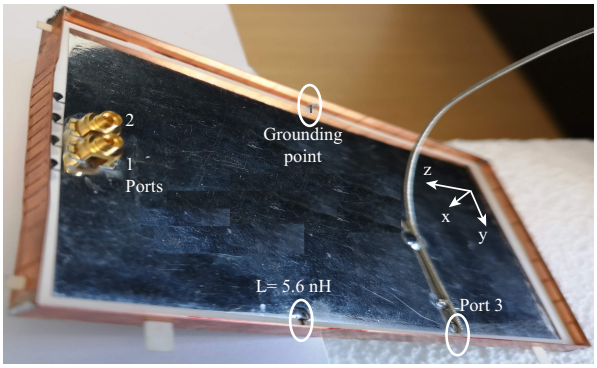

Fig. C.11: Antenna prototype.

The reflection and transmission coefficients of the simulated and measured mm-wave array are plotted in Fig. C.12(a). Good agreement can be found between measurements and simulations. The bow-tie array is matched from 22 GHz to 28.4 GHz with -10 dB specification, which is more than enough to cover the 5G bands n258 (24.25-27.5 GHz) and n261 (27.5-28.35 GHz) [19]. The transmission coefficient is below -10 dB in the whole impedance bandwidth and below -15 dB in the bands of n258 and n261. The total efficiency of the mm-wave array is 92 %. The reflection coefficient of the frame antenna is represented in Fig. C.12(b). For the sub-3 GHz antenna, the matching criterion is more relaxed and set to -6 dB. The measured antenna is matched at the frequency bands 760-980 MHz and 1240-2870 MHz. The total efficiency of the frame antenna is 77 % (760-980 MHz band), 90 % (1240-2090 MHz band) and 80 % (2355-2870 MHz band). It is important to guarantee that the low and high-

frequency antennas are not going to modify their performance when they are simultaneously operated. The simulated mutual coupling between the frame antenna and the mm-wave array is below -15 dB in the low band and below -25 dB in the operating mm-wave band, as it is shown in Fig. C.12.

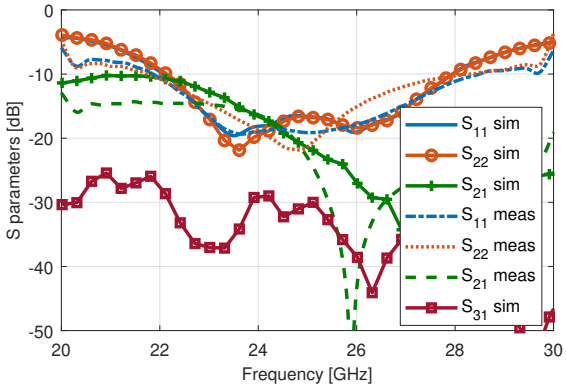

(a)

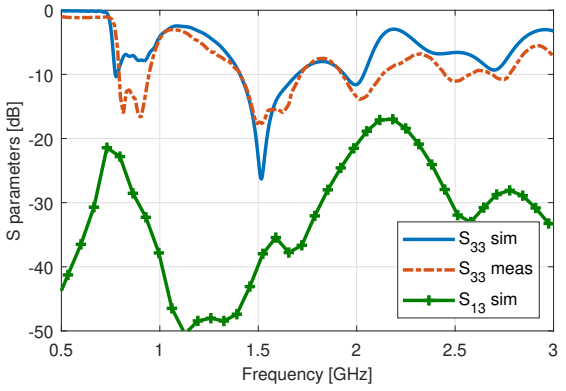

(b)

Fig. C.12: Comparison of s-parameters between measurements and simulations. (a) Mm-wave array. (b) Sub-3 GHz antenna.

The measuring set-up of the anechoic chamber for the mm-wave array is shown in Fig. C.13. Due to its configuration, θ values larger than 135° have been not plotted in the measured results [Fig. C.13(b)]. The radiation patterns of the two antennas [numbering specified in Fig. C.11] are plotted in Fig. C.14 for the $\Phi = 0°$ cut and in Fig. C.15, for the $\Phi = 90°$ cut. The simulated results are in a good agreement with the measurements at both 24 and 26

GHz. The radiation patterns point to the endfire direction and the measured gain is similar to the one obtained in the simulations, which means that the slots have successfully improved the gain of the mm-wave array.

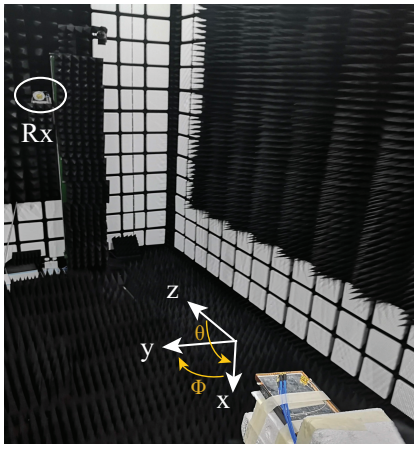

(a)

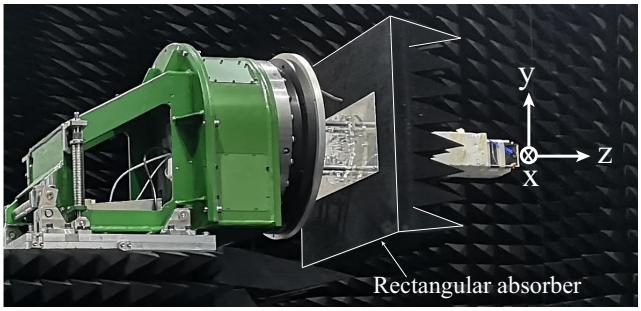

(b)

Fig. C.13: Anechoic chamber set-up. (a) Transmitter and receiver. (b) Details of the mechanic arm.

The evaluation of the realized gain in the endfire direction as a function of the frequency is represented in Fig. C.16. The combined gain, when the array is excited in phase, is higher than 7 dBi in the whole frequency range. Fig. C.17 shows the beam-steering envelope comparison of the mm-wave array without frame and with a slotted frame at 24 and 26 GHz. The slots enhance the gain radiated from the antennas around 1 dB in the endfire direction and extend the scanning angle. When the bow-tie antenna points to the maximum scanning angle, the radiation pattern presents several ripples. However, scanning with the slotted frame helps to focus the energy in a certain direction and therefore, reduce the ripples. For that reason, the beam-steering envelope is flatter and

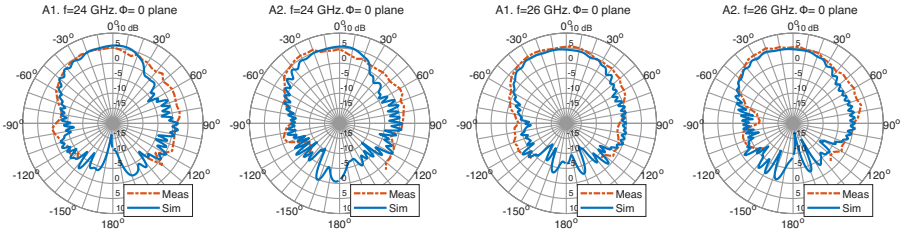

(a) (b) (c) (d)

Fig. C.14: Radiation patterns of the two active antennas at the $\Phi = 0°$ at 24 and 26 GHz.

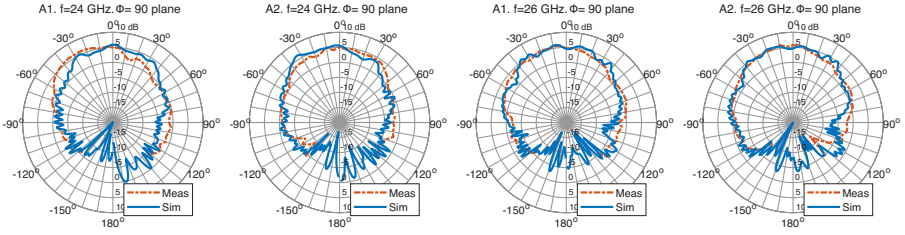

(a) (b) (c) (d)

Fig. C.15: Radiation patterns of the two active antennas in the $\Phi = 90°$ at 24 and 26 GHz.

broader when the slotted frame is placed in front of the antenna. The impact of the slotted-frame on the main beam direction has also been examined. Fig. C.18 shows the effect of the frame for three different beams. The phase shifting between the two elements is $\Delta\varphi = 90°$, $0°$ and $-90°$, respectively. It can be observed that, when the slotted-frame is added, the ripples are reduced and the beam gain is enhanced. The main beam remains towards similar directions with and without the metal frame. Therefore, the embedded array in the slotted metal-frame does not cause a significant error on beam alignment processes.

VI Comparison with the state of art

This contribution is compared with the state of art. The figures-of-merit (FoM) of all the proposed solutions are compared in Table C.2. Among the FoM, the term "embeddable" refers to the possibility of embedding the proposed mm-wave array in a sub-3 GHz frame antenna. The term "gain improvement" considers if there has been a gain enhancement in the mm-wave array after the embedding. The majority of the commercial handsets have a metallic frame. For that reason, the frame has been used as a location to place the

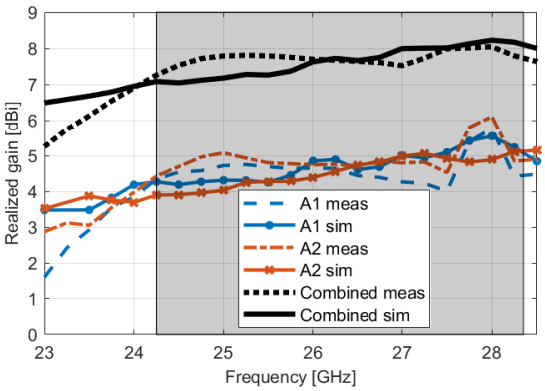

Fig. C.16: Realized gain in the endfire direction ($+z$ axis) of the antenna elements separately and the in-phase combination of them.

Table C.2: Comparison of this paper with the previous work

	Volume [mm^3]	Antenna-frame distance [mm]	Band [GHz]	Pattern	Peak gain in band [dBi]	Num. antennas	Beam-steering	Embeddable	Gain improvement
[7]	43.6 x 7.1 x 1	N.A.	27.2-28.5	Broadside	14	8 (8 active)	$0° \sim 60°$	No	N.A.
[16]	51.3 x 7 x 4	N.A.	27.5-30	Broadside	15.6	8 (8 active)	$0° \sim 60°$	No	N.A.
[17]	17.8 x 8 x 2.5	N.A.	27-28.5	Endfire	11.7	8 (8 active)	$\pm 80°$	No	N.A.
[18]	30 x 5 x 5	N.A.	27-29.5; 36.8-40.3	Broadside	11.3; 12	5 (5 active)	$-60° \sim 0°$	No	N.A.
[14]	23 x 7 x 4	N.A.	25-30	Endfire	7	4 (4 active)	$\pm 25°$	Yes	No
[15]	30 x 8.8 x 0.64	7	24-27.5	Endfire	11	6 (4 active)	$\pm 60°$	Yes	No
This work (2 active)	**21.7 x 7.75 x 0.64**	**0.5**	**22-28.4**	**Endfire**	**8**	**4 (2 active)**	**-**$40° \sim 40°$	**Yes**	**Yes**
This work (4 active)	**21.7 x 7.75 x 0.64**	**0.5**	**22-28.4**	**Endfire**	**10.7**	**4 (4 active)**	**-**$80° \sim 70°$	**Yes**	**Yes**

mm-wave arrays in [7,16,17]. These designs use 8 active elements for the array, so the peak gain obtained is, in general, higher than in the other configurations. Nevertheless, the number of phase-shifters and power amplifiers increases and the remaining space in terminals is limited. Besides, the overall performance of these arrays is similar to the solutions with fewer elements. The embedding of a mm-wave array in a sub-3 GHz frame antenna has only been published in a few papers [14,15,18] to the best of the authors' knowledge. Even though the number of active elements is bigger than 4 in [14,18], the beam-steering range of both proposals is lower than 60°, which would force the handset to have 4 mm-wave modules if the whole sphere has to be covered. The most similar solution corresponds to the previous work from the authors [15] since they both have the goal of preventing the blockage caused by the metallic frame of the phones, without removing a large section of the bezel. In that design, the reduction of the main-beam blockage in the presence of a metallic bezel is achieved with two tilted layers of metal strips located at both edges of the frame. The energy impinging on the frame is coupled to the layers of metal strips, that act as

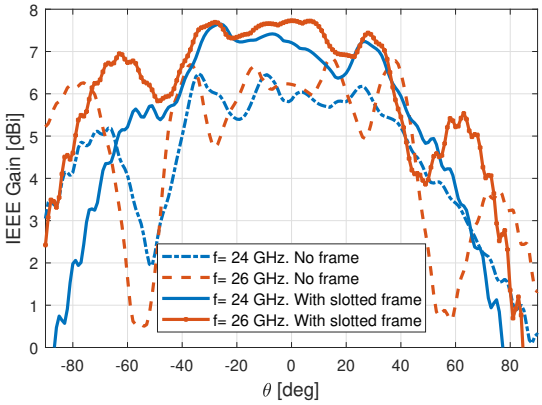

Fig. C.17: Simulated beam-steering envelope comparison of the array without frame and with the slotted frame.

parasitic radiators and the fields are added in phase in the far-field. In this paper, the horizontal currents excited on the frame by the mm-wave antenna are utilized differently. The idea is to etch slots on the frame so they can be fed by these horizontal currents. This way the array aperture is enlarged and the gain increases. The design of this paper provides the lowest number of active elements with a peak realized gain of 8 dBi. The proposals in [14,15] allow the embedding of the mm-wave array in the low-frequency metal-frame antenna, but no gain enhancement is achieved after the embedding. However, the solutions in this work are able to increase at least 1.5 dB the gain of the antenna in free-space. Comparing with [15], the distance from the top part of the mm-wave array to the bezel is considerably reduced in this paper.

VII Conclusion

The method proposed in this paper to overcome the blockage of the frame to endfire 5G arrays is to etch several slots on the side of the frame where the mm-wave array is located. The slots not only reduce the obstruction but also enhance the gain of the array. A bow-tie array is designed as endfire mm-wave array, and it is embedded in the handset frame, which is used as sub-3 GHz antenna. The co-design of the two antennas is simple, with the clearance of the bow-tie array as the only constraint, imposed by the low-frequency antenna. As shown in the results, both antennas operate independently without degrading the performance of the other.

Design considerations have been studied to obtain the best performance

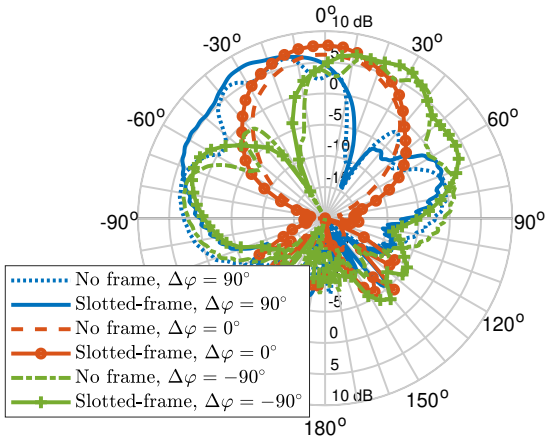

Fig. C.18: Radiation pattern comparison at the $\Phi = 90°$ cut of the array without frame and with the slotted frame for three different beams at 26 GHz.

of the array. In order to broaden the beam-steering scanning properties, the aperture of the slot array needs to be larger than the mm-wave array. The distance from the top part of the bow-tie array to the frame defines the impedance bandwidth and gain. Small distances provide wide impedance matching but with lower gain. The performance of the proposed array has been compared with its counterpart with 4 active elements and no frame. Two more active antennas can increase the gain around 0.5 dB and broaden the scanning range. The final design has been manufactured and measured. Good agreement is found between measurements and simulations. The mm-wave array is matched from 22-28.4 GHz, covering the n258 and n261 bands. Measured radiation patterns demonstrate the principle, with a gain higher than 7 dBi in the operating band. The array is able to scan in the range -40° $< \theta <$ 40°. The low-frequency antenna covers the frequency bands 760-980 MHz and 1240-2870 MHz.

Acknowledgment

The authors would like to thank Ben Krøyer for his help in the antenna manufacturing and Kim Olesen for his assistance in the chamber set-up.

References

[1] W. Hong, K.-H. Baek, Y. Lee, Y. Kim, and S.-T. Ko, "Study and prototyping of practically large-scale mmwave antenna systems for 5G cellular devices," *IEEE Commun. Mag.*, vol. 52, no. 9, pp. 63–69, 2014.

[2] Z. Pi and F. Khan, "An introduction to millimeter-wave mobile broadband systems," *IEEE Commun. Mag.*, vol. 49, no. 6, 2011.

[3] T. S. Rappaport, S. Sun, R. Mayzus, H. Zhao, Y. Azar, K. Wang, G. N. Wong, J. K. Schulz, M. Samimi, and F. Gutierrez, "Millimeter wave mobile communications for 5G cellular: It will work!" *IEEE Access*, vol. 1, pp. 335–349, 2013.

[4] W. Hong, K.-H. Baek, and S. Ko, "Millimeter-wave 5G antennas for smartphones: Overview and experimental demonstration," *IEEE Trans. Antennas Propag.*, vol. 65, no. 12, pp. 6250–6261, 2017.

[5] M. Stanley, Y. Huang, H. Wang, H. Zhou, A. Alieldin, and S. Joseph, "A novel mm-wave phased array antenna with 360° coverage for 5G smartphone applications," in *2017 10th UK-Europe-China Workshop on Millimetre Waves and Terahertz Technologies (UCMMT)*. IEEE, 2017, pp. 1–3.

[6] Y. Wang, H. Wang, and G. Yang, "Design of dipole beam-steering antenna array for 5G handset applications," in *2016 Progress in Electromagnetic Research Symposium (PIERS)*. IEEE, 2016, pp. 2450–2453.

[7] J. Bang and J. Choi, "A SAR reduced mm-wave beam-steerable array antenna with dual-mode operation for fully metal-covered 5G cellular handsets," *IEEE Antennas Wireless Propag. Lett.*, vol. 17, no. 6, pp. 1118–1122, 2018.

[8] R. Rodríguez-Cano, S. Zhang, and G. F. Pedersen, "Beam-steerable multi-band mm-wave bow-tie antenna array for mobile terminals," in *12th European Conference on Antennas and Propagation (EuCAP 2018)*, April 2018, pp. 1–4.

[9] R. A. Alhalabi and G. M. Rebeiz, "High-efficiency angled-dipole antennas for millimeter-wave phased array applications," *IEEE Trans. Antennas Propag.*, vol. 56, no. 10, pp. 3136–3142, 2008.

[10] S. Zhang, I. Syrytsin, and G. F. Pedersen, "Compact beam-steerable antenna array with two passive parasitic elements for 5G mobile terminals at 28 GHz," *IEEE Trans. Antennas Propag.*, vol. 66, no. 10, pp. 5193–5203, 2018.

[11] I. Syrytsin, S. Zhang, G. F. Pedersen, and A. S. Morris, "Compact quad-mode planar phased array with wideband for 5G mobile terminals," *IEEE Trans. Antennas Propag.*, vol. 66, no. 9, pp. 4648–4657, 2018.

[12] M. M. Samadi Taheri, A. Abdipour, S. Zhang, and G. F. Pedersen, "Integrated millimeter-wave wideband end-fire 5G beam steerable array and low-frequency 4G LTE antenna in mobile terminals," *IEEE Trans. Veh. Technol.*, vol. 68, no. 4, pp. 4042–4046, April 2019.

[13] R. Hussain, A. T. Alreshaid, S. K. Podilchak, and M. S. Sharawi, "Compact 4G MIMO antenna integrated with a 5G array for current and future mobile handsets," *IET Microw., Antennas Propag.*, vol. 11, no. 2, pp. 271–279, 2017.

[14] J. Kurvinen, H. Kähkönen, A. Lehtovuori, J. Ala-Laurinaho, and V. Viikari, "Co-designed mm-wave and LTE handset antennas," *IEEE Trans. Antennas Propag.*, vol. 67, no. 3, pp. 1545–1553, 2019.

[15] R. Rodriguez-Cano, S. Zhang, K. Zhao, and G. F. Pedersen, "Reduction of main beam-blockage in an integrated 5G array with a metal-frame antenna," *IEEE Trans. Antennas Propag.*, vol. 67, no. 5, pp. 3161–3170, May 2019.

[16] B. Yu, K. Yang, G. Yang *et al.*, "A novel 28 GHz beam steering array for 5G mobile device with metallic casing application," *IEEE Trans. Antennas Propag.*, vol. 66, no. 1, pp. 462–466, 2018.

[17] S. S. Kim, S. H. Kim, J. H. Bae, and Y. J. Yoon, "Switched folded slot phased array antenna for mm wave 5G mobile in metal bezel design," in *2018 IEEE International Symposium on Antennas and Propagation & USNC/URSI National Radio Science Meeting*. IEEE, 2018, pp. 239–240.

[18] Y. Wang, H.-C. Huang, and X. Jian, "Novel design of a dual-band 5G mm-wave antenna array integrated with a metal frame of a cellular phone," in *2018 Asia-Pacific Microwave Conference (APMC)*. IEEE, 2018, pp. 1582–1584.

[19] "General aspects for User Equipment (UE) Radio Frequency (RF) for NR (Release 15)," 3rd Generation Partnership Project (3GPP), Technical Report (TR) 38.817-1, 03 2019, version 15.3.0.

[20] K. Loi, S. Uysal, and M. Leong, "Design of a wideband microstrip bowtie patch antenna," *IEE Proceedings-Microwaves, Antennas and Propagation*, vol. 145, no. 2, pp. 137–140, 1998.

[21] C. Deng, Z. Xu, A. Ren, and S. V. Hum, "TCM-based bezel antenna design with small ground clearance for mobile terminals," *IEEE Trans. Antennas Propag.*, vol. 67, no. 2, pp. 745–754, 2019.

[22] A. Vasjanov and V. Barzdenas, "A review of advanced CMOS RF power amplifier architecture trends for low power 5G wireless networks," *Electronics*, vol. 7, no. 11, p. 271, 2018.

[23] N. Rostomyan, M. Özen, and P. Asbeck, "28 GHz doherty power amplifier in CMOS SOI with 28 percent back-off PAE," *IEEE Microw. Wirel. Compon. Lett.*, vol. 28, no. 5, pp. 446–448, 2018.

Paper D

Handset Frame Blockage Reduction of 5G mm-Wave Phased Arrays Using Hard Surface Inspired Structure

Rocío Rodríguez Cano, Kun Zhao, Shuai Zhang and Gert Frølund Pedersen

The paper has been published in
IEEE Transactions on Vehicular Technology. Volume: 69, Issue: 8, 2020, pp. 8132–8139.

Abstract

In this paper, the propagating characteristics of hard surfaces are employed to reduce the main beam blockage of the handset frame to horizontally polarized endfire millimeter-wave (mm-wave) arrays. To prove the concept, a quad-element vivaldi array is located at the top part of the handset and the frame with grooves is placed in front of it. The groove dimensions that form the hard surface inspired structure are studied to provide the best gain and reflection coefficient performance. The impedance bandwidth achieved is 25.3-27.5 GHz. The radiation pattern plots show that the main beam direction corresponds to endfire, the same as the original array without the frame. The mm-wave array provides beam-steering properties with a scanning angle of $\pm 65^{\circ}$ for a realized gain higher than 7 dBi.

I Introduction

The upcoming fifth generation of mobile communication (5G) includes new frequency bands in the millimeter-wave (mm-wave) range to cope with the saturation of the spectrum below 7 GHz [1–3]. The new frequency bands have motivated the appearance of many mm-wave antenna array designs for mobile phones. To compensate for the higher propagation losses and highly randomness in the wireless channel, antenna systems are required to have high gain and large beam-steering angle. Many of the designs in literature correspond to planar endfire arrays [4–13]. However, most of the solutions do not take into account the phone bezel. The placement of the handset metallic bezel in front of endfire mm-wave antennas can be detrimental to their radiation pattern, causing the partial or full obstruction of the main beam. Therefore, reducing the obstruction of metallic phone bezels is a critical step to implement endfire arrays in mobile handsets successfully. In previous studies from the authors, it was shown that the radiation pattern blockage is significant in the case of horizontal polarization, whilst the radiation pattern of antennas with vertical polarization remains almost unaffected [14]. For that reason, this paper only focuses on the horizontal polarization. There are some papers that consider the effect of the frame in the embedding of mm-wave arrays. In [14], two parasitic layers are added at both sides of the frame to redirect the radiation pattern to the endfire direction as a result of the energy coupling from the frame. The proposed solution in [15] consists of etching a window in the frame to place the mm-wave module. The design presented in [16] etches several vertical slots on the center of the frame to function as a second array and enhance the main beam gain. In this paper, the concept of hard surfaces is employed to reduce the frame blockage to mm-wave antennas by decreasing the edges diffraction.

The term hard surface comes from acoustics. In electromagnetism, it is used to designate an ideal conductor that is corrugated with longitudinal grooves that are filled with dielectric material [17]. This type of structure supports the wave propagation through it, with a maximum value of the E-field at the surface. If the surface is loaded with dielectric material in the z direction (according to the coordinate system in Fig. D.1), with the proper design, the corrugated structure can behave as a hard surface for both vertical and horizontal polarizations. This concept has been employed in literature to reduce the forward scattering in the case of cylindrical struts in antennas with parabolic reflectors. In [18], the struts and masts are constructed using hard surfaces, reducing the sidelobes caused by the inherent blockage.

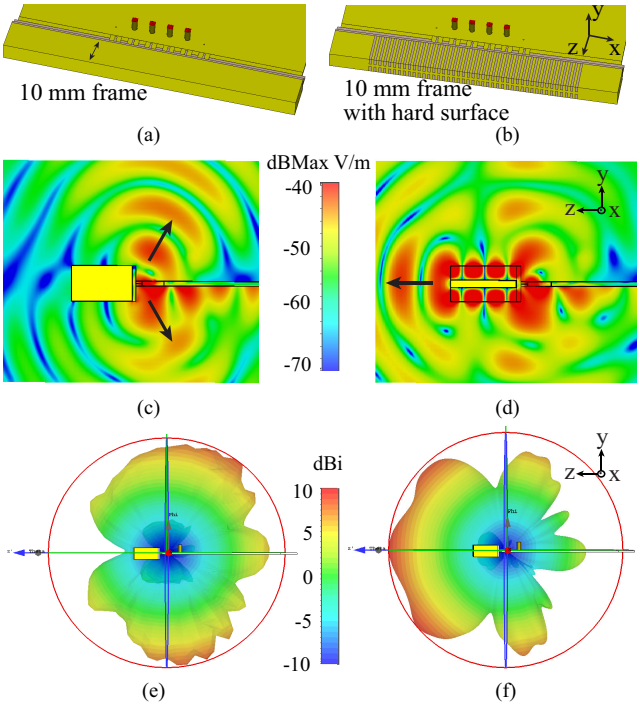

Fig. D.1: (a) Front view of the mm-wave array with a 10 mm-thickness frame. (b) Front view of mm-wave array with a hard surface. (c) YZ plane cut of the E-field of (a). (d) YZ plane cut of the E-field of (b). (e) Realized gain radiation pattern of the $\Phi = 90°$ cut of (a). (f) $\Phi = 90°$ cut of (b).

To illustrate the concept, Fig. D.1 (a) shows a mm-wave vivaldi array with a 10 mm-thick frame in front of it. The frame is a piece of metal with overall dimensions 5 mm $\times$88 mm $\times$10 mm, and it is placed 1 mm away from the top part of the mm-wave array. The vivaldi array has horizontal polarization, i.e. x axis direction, and has end-fire radiation [14]. The side view of the electric field

is represented in Fig. D.1 (c). As can be seen, the E-field is diffracted by the frame and the main beam direction changes from endfire to other directions. For that reason, mm-wave arrays for the upcoming 5th generation of mobile communication need to consider the effect of the frame in the antenna design. When the frame is incorporated, the electric field is diffracted backward and the radiation pattern becomes broadside (Fig. D.1 (e)). The principle of operation consists in supporting the wave propagation through the frame (in the z axis direction) to reduce its blockage width. Since the wave is allowed to propagate through the frame when the hard surface inspired design is employed (Fig. D.1 (b)), less energy is diffracted and the main beam points to the original direction (Fig. D.1 (f)). To provide a hard surface behaviour, two rows of grooves have been etched on the frame and then filled with dielectric material. This solution does not require any large windows or extra structures. The proposed mechanism is demonstrated with a manufactured prototype of the frame with two rows of grooves in front of a vivaldi array. Measurements and simulations show good agreement. Simulations are carried out by CST Microwave Studio 2019.

II Metal Frame with Corrugated Edges

The phone bezel is significantly thinner than 10 mm, which was the example width employed in the introduction. The same hard surface concept can be extended to commercial models to make the main beam radiate in the original direction, as shown in Fig. D.2. It can be considered as cutting a thin slice of the previous 10 mm-thick frame, as detailed in Fig. D.3. The frame is formed by a substrate of $\epsilon_r = 6$ with a metallic layer on the outer side, and it is placed 1 mm away from the mm-wave array.

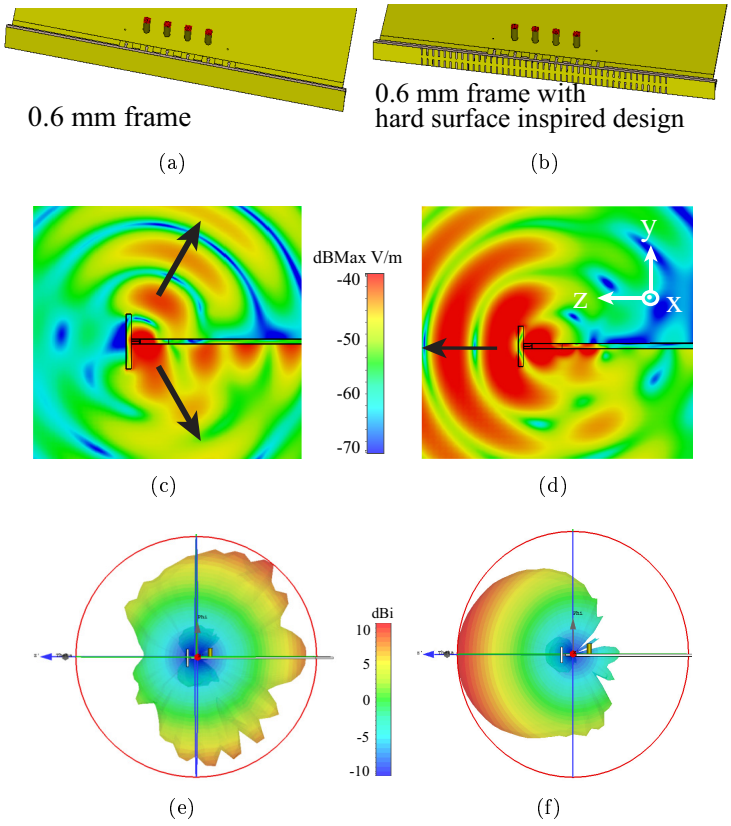

Fig. D.2: (a) Front view of the mm-wave array with a 0.6 mm-thickness frame. (b) Front view of mm-wave array with a hard surface inspired frame. (c) YZ plane cut of the E-field of (a). (d) YZ plane cut of the E-field of (b). (e) Realized gain radiation pattern of the $\Phi = 90°$ cut of (a). (f) $\Phi = 90°$ cut of (b).

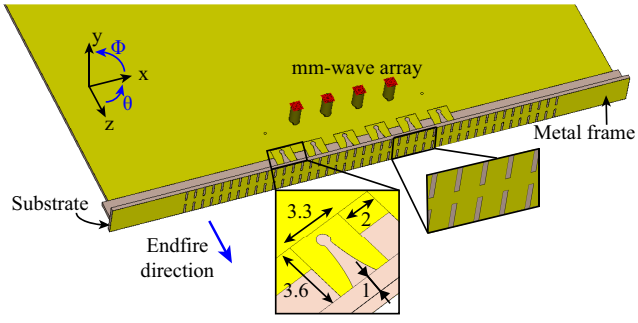

Fig. D.3: Geometry of the proposed antenna.

In order to demonstrate the effect from the corrugated edges on reducing the blockage of the metal frame, a horizontally polarized plane wave illuminates the metal frame from a normal angle of incidence, as shown in Fig. D.4. There is no air space between the frame and the open boundary condition on $+x$ and $-x$ direction to exclude the scattering on the short edge of the frame. The corresponding electrical field at 22 GHz is represented in Fig. D.5 (a), where the groove length is $l_{hs} = 2$ mm. To show the effect of the corrugated hard surface inspired design, two reference frame structures without grooves are also shown, one 1 mm wide and the other 5 mm wide. The plane wave propagation in free space has also been given. It can be observed that the E-field is guided over the metal frame through the corrugated edge, and the blockage on the E-field is considerably reduced.

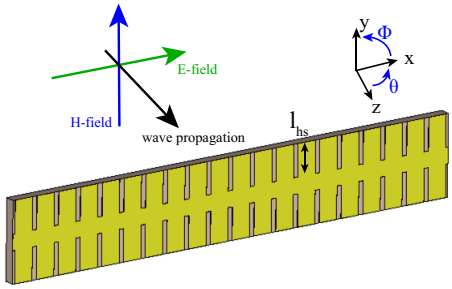

Fig. D.4: Plane wave illuminating a 30 mm-long frame. The polarization of the plane wave is marked with arrows (the electric field corresponds to the green arrow).

To further quantify the effect from the corrugated structure, the corresponding monostatic radar cross section (RCS) has also been calculated. The monostatic RCS measures the power scattered back by the metal frame, and therefore, it is preferred to have a small RCS for the metal frame to reduce the blockage effect. In Fig. D.6, the RCS of the different cases discussed has been plotted. A clear reduction in the RCS value can be observed by using the corrugated metal frame ($l_{hs} = 2$ mm), and the RCS of the metal frame can be reduced a wide band comparing to the 1 mm-wide frame. On the other hand, the operating band of the corrugated frame can be controlled by tuning the length of the slot (l_{hs}), which can make the design be fitted in different bands of interest in a practical phone design. The corrugation of the final design has a length of $l_{hs} = 2$ mm. The lengths employed for the shorter and longer corrugations are 1.75 mm and 2.25 mm, respectively.

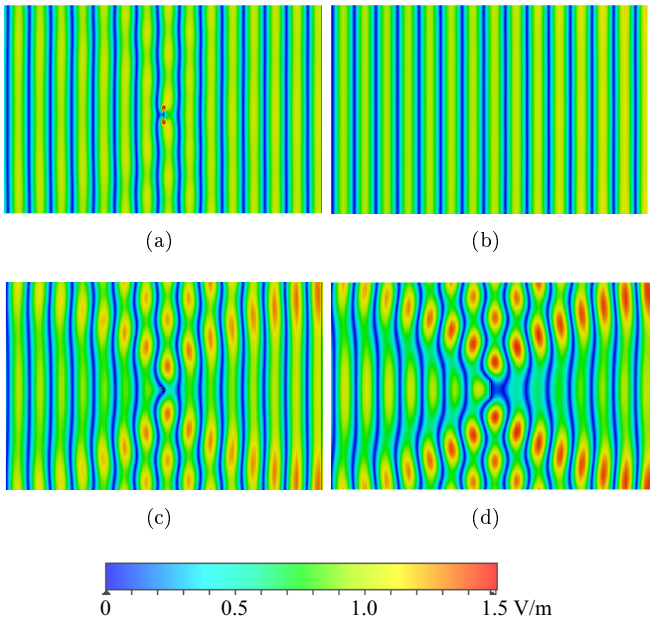

Fig. D.5: E-field at 22 GHz in the YZ plane. (a) With corrugations. (b) Free space. (c) With a 1 mm-width frame. (d) With a 5 mm-width frame.

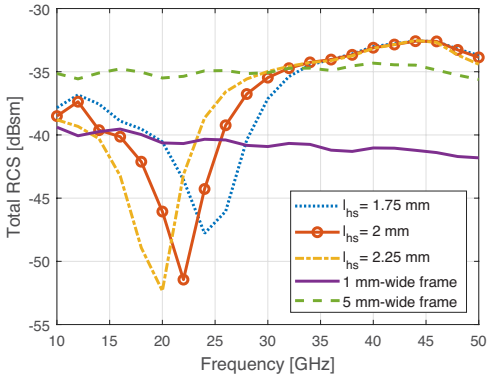

Fig. D.6: Radar cross section (RCS) of different frame configurations.

It is worth mentioning that the above analysis is based on a plane wave with normal angle of incidence. In practice, the mm-wave antennas for mobile phones will be placed very close to the phone bezel and thus, the plane wave assumption used above will not be valid. In order to verify that the proposed design can operate properly in a practical design, the analysis based on a device

with smartphone form factor will be given in the next section. In fact, in the next section the operating frequency is shifted up with the full phone model and the same groove length.

III Proposed Mechanism

In order to demonstrate that the structure performs like a hard surface and it is not due to the partial reduction of the frame width because of the grooves, four different configurations are further compared in Fig. D.7. The in-phase combination of all the array elements is plotted as a function of the frequency. IEEE gain is chosen as it does not consider the mismatching losses, that can be different according to the frame width. The gain curve of the vivaldi array without frame has been added as a reference. The following two configurations correspond to the frame without grooves of width 1 and 5 mm, respectively. The last curve represents a 5 mm-width frame with the grooves forming the hard surface inspired design. The space between the two groove rows is 1 mm. As it can be seen, the frame with corrugations is 2 dBi higher than the 1 mm-width frame and almost 10 dBi higher than the 5 mm-width metal frame. The gain improves 1 dB with respect to the array with no frame at 25 GHz.

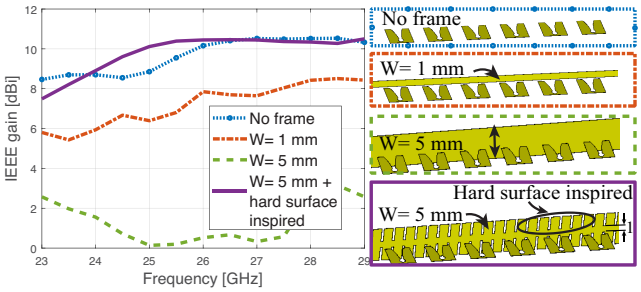

Fig. D.7: Combined endfire IEEE gain (in the $+z$ axis direction) frequency evolution according to frame width.

Mm-wave phased arrays are supposed to scan the beam in different directions and achieve high gain. The simulated beam-steering envelope of the mm-wave array with the frame with grooves is represented in Fig. D.8. The envelope is formed by the maximum gain of 12 beams, with a phase difference of 30°. The beam is able to scan ±65° with a gain higher than 7 dBi. With 7 dBi array gain, the 5G mm-wave UE can meet the 3GPP EIRP requirement [19], with a limited TRP level in the band of interest. Therefore, we define here the scanning angles according to 7 dBi. The gain in the boresight direction reaches 10 dBi, while when the phase difference between the elements is 150°, the gain is around 7 dBi. That is due to the vivaldi element radiation pattern. In Fig.

D.8(b) the realized gain envelope is represented for different frequencies. The gain drop at 25 GHz is due to the fact that the impedance matching is degraded and the realized gain takes into account the mismatching losses.

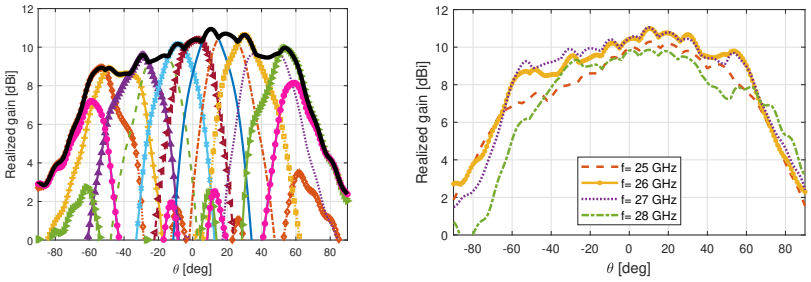

(a) (b)

Fig. D.8: $\Phi = 0°$ cut of: (a) simulated realized gain beam scanning from -65° to 65° and beam-steering envelope at 26 GHz. (b) Simulated realized gain beam-steering envelope at different frequencies.

IV Parametric Studies

The operating frequency, groove dimensions, and other design factors can be controlled to meet the demand of various phone form factors. This section comprises the most important parameters in the design of the hard surfaces. The assessed parameters are: groove length, the effect of the substrate dielectric constant, groove periodicity and groove width.

A. Groove length

The length of the grooves etched on the frame has a strong influence on the gain of the array and the reflection coefficient, as shown in Fig. D.9. For this study, a dielectric permittivity of 6 is chosen. For a length $l_{hs} = 0$ mm, i.e. full 5 mm-width frame without any grooves, the gain in the endfire direction ($+z$ axis) between 24 and 28 GHz is below to 2 dBi. Increasing the length of the groove reduces the frame blockage and allows the electric field to propagate through and for that reason, the gain increases. A value of 2 mm has been chosen to maximize the impedance bandwidth and obtain high gain. If this value is expressed in wavelength terms, $\lambda_g/4 < l_{hs} < \lambda_g/2$.

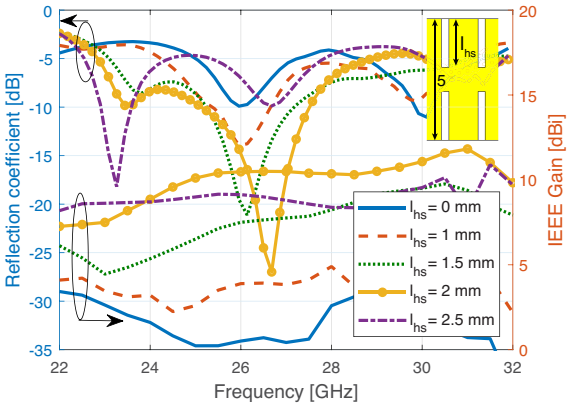

Fig. D.9: Reflection coefficient and IEEE gain in the endfire direction for different lengths of the grooves.

B. Effect of the dielectric constant

The dielectric constant of the frame substrate is another parameter to consider. Fig. D.10 shows how an increase in the permittivity provides higher gain. The value of ϵ_r that presents a broad impedance bandwidth with high gain is 6. A gain increment is observed in Fig. D.10 when the permittivity of the substrate is increased. However, this gain increment only occurs when the frame is composed of dielectric and the modified metal. When only dielectric is placed in front of the array, an increase in the substrate permittivity does not translate into an increase of gain, but a shift of the curve towards lower frequencies. As mentioned in the previous subsection, the groove length can be expressed in wavelength terms. The guided wavelength (λ_g) is defined as the free-space wavelength divided by the square root of the dielectric constant. It is important to consider that these results are obtained without tuning the mm-wave array or the groove dimensions. If there is the possibility of modifying and matching the array, a frame substrate with a higher dielectric constant can be chosen, resulting in grooves with a shorter length. This could make the hard surface solution less noticeable to the frame design and increase the mechanical robustness. The results for an optimized $\epsilon_r = 10$ have also been included in Fig. D.10. Only the groove length has been modified to $l_{hs} = 1.5$ mm. The impedance bandwidth is smaller than the one obtained with the chosen permittivity, but the gain increases 0.8 dBi. It can also be observed that the gain performance in the band of interest is similar with the optimized designs for different substrate permittivities, which also verifies that the gain enhancement is not related to the increment in the permittivity.

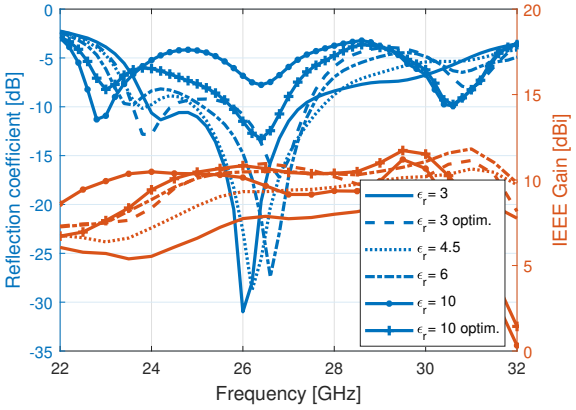

Fig. D.10: Reflection coefficient and IEEE gain in the endfire direction for different dielectric constants.

C. Groove periodicity

The groove periodicity is another critical parameter and it is represented in Fig. D.11. Broader separations provide in general higher gain, but narrower impedance bandwidth. A periodicity of 1.5 mm is chosen for the design not to limit considerably the impedance bandwidth. The periodicity has to be smaller than $\lambda/2$.

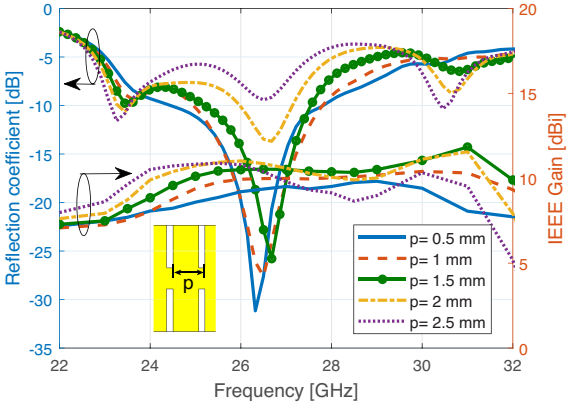

Fig. D.11: Reflection coefficient and IEEE gain in the endfire direction for different periodicity.

D. Groove width

The effect of the grooves width is represented in Fig. D.12. The width is not as critical as the length, but there is a trade-off between gain and impedance bandwidth. For a fixed periodicity of the grooves etched, the narrower the groove is, the wider the strip would be. Therefore, the gain is higher at lower frequencies. The impedance bandwidth is, however, narrower when the width of the groove is reduced. Due to this compromise, a width of $W_{hs} = 0.3$ mm is chosen for the design.

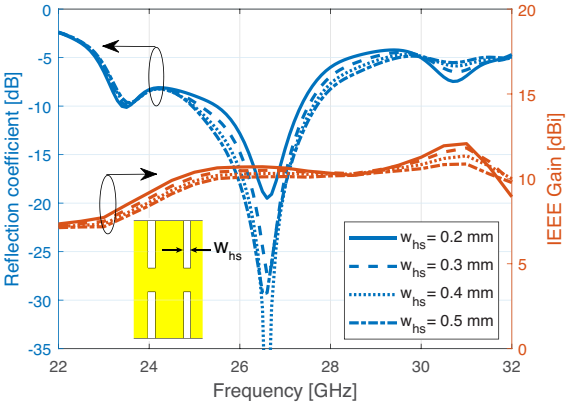

Fig. D.12: Reflection coefficient and IEEE gain in the endfire direction for different widths of the grooves.

To sum up, the groove length is the most critical parameter. In addition, the dielectric permittivity of the frame substrate and periodicity of the grooves have also a strong influence on the gain and impedance curves. By properly tuning these parameters, the proposed method can be implemented for different operating frequencies and phone form factors.

V Final Design and Results

The parametric studies from Section IV have provided the optimum design parameters for the frame inspired in hard surfaces. The final design corresponds with the model of Fig. D.3, and the final parameter values are listed in Table D.1. The parameter w_{frame}, corresponds to the frame width and t_{subs} is the thickness of the frame substrate. The mm-wave array is located at the top part of the PCB and is formed by 4 active vivaldi elements and 2 grounded elements at the opposite ends to provide similar boundary conditions. The metallic frame with grooves is placed 1 mm away from the array. The frame is

also made of the same kind of PCB of $\epsilon_r = 6$, and only one metalized side. A prototype has been fabricated and it is represented in Fig. D.13. As mentioned in Section IV, the aim of this publication is to design the frame to reduce the blockage. The mm-wave vivaldi array used to prove the principle is carried out in [14]. Throughout this section, the performance of the prototype is evaluated.

Table D.1: Final design parameters

l_{hs}	w_{hs}	p	$Ant.\text{-}frame$ $distance$	w_{frame}	ϵ_r	t_{subs}
2 mm	0.3 mm	1.5 mm	1 mm	5 mm	6	0.635 mm

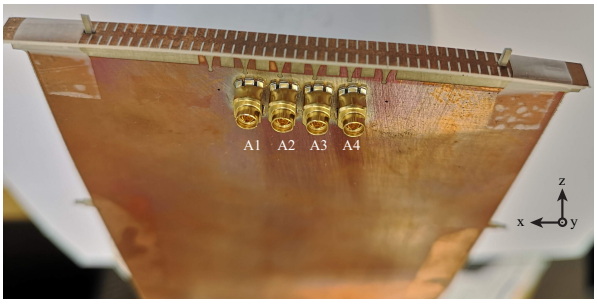

Fig. D.13: Fabricated prototype. Only the top part of the PCB is shown.

The scattering parameters are plotted in Fig. D.14. The antenna is matched below -10 dB from 23.6 to 27.5 GHz. The coupling between the central elements of the array is lower than -15 dB in all the impedance bandwidth. The total efficiency of the array is higher than 90 % in the operating bandwidth, reaching a maximum value of 94 % at 26.5 GHz.

Fig. D.15 shows the measurement set-up for the radiation pattern measurements. Due to the absorber placed behind the antenna, the angle θ is only displayed until 150°. The measurement procedure is described next. The phase center of the measurement system is located first. Afterwards, the center of the array is placed at the phase center of the measurement system. Each antenna element is measured without changing the position of the array. The combined gain can be computed as the sum over all the elements of the measured gain pattern of the antenna element multiplied by the phase shift at the feed of the element.

The combined radiation pattern of all the elements in phase is depicted in Fig. D.16 for the $\Phi = 0°$ and $\Phi = 90°$ cuts. The main beam points to the endfire direction and the sidelobe level is -11.9 dB (Fig. D.16 (a)). The fact that the array is broad in θ is favourable to achieve a 360° beam-

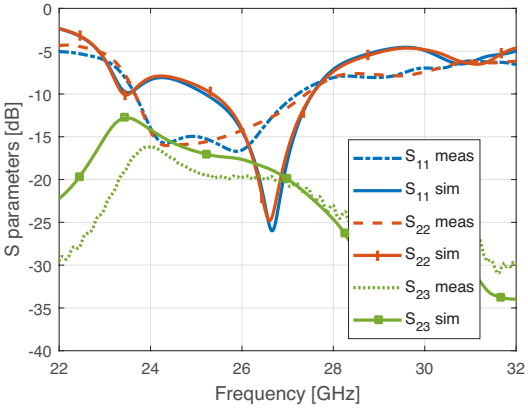

Fig. D.14: S parameters comparison between measurements and simulations.

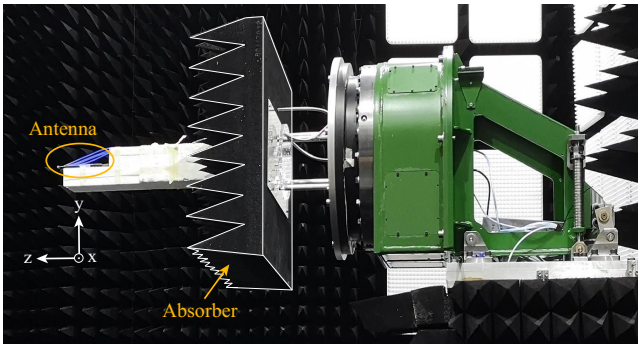

Fig. D.15: Measurements set-up of the chamber.

steering coverage. A maximum realized gain of 10.2 dBi is obtained in the endfire direction. The combined radiation pattern has also been plotted in Fig. D.17 for different phase shifts among the elements ($\Delta\phi = 0°, 90°, 150°$) and for different frequencies. Good agreement is found between measurements and simulations. The evolution of the endfire realized gain as a function of the frequency is shown in Fig. D.18. The combined gain is higher than 7 dBi in all the operating band of 25.3-27.5 GHz, with a value of approximately 10 dBi from 25-26.5 GHz. Similar gain behaviour is found between the symmetric elements both in the measurements and simulations. Due to the detuning of the antenna, the gain is lower at the higher frequencies.

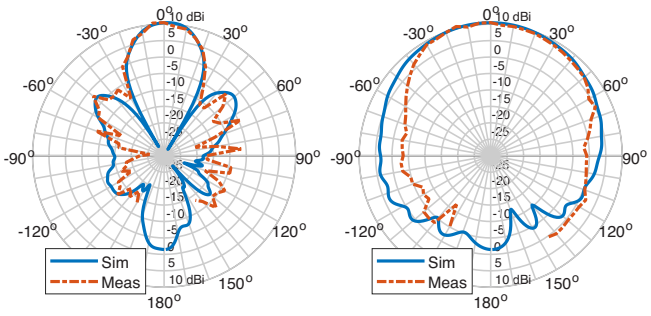

(a) (b)

Fig. D.16: Combined realized gain in-phase radiation pattern at 26 GHz. (a) $\Phi = 0°$ cut. (b) $\Phi = 90°$ cut.

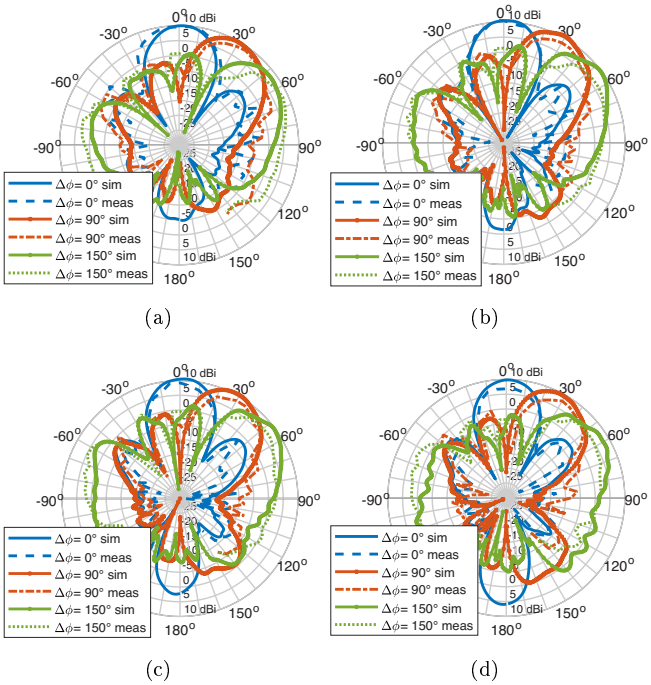

(a) (b)

(c) (d)

Fig. D.17: Combined realized gain radiation pattern for different phase shifts ($\Delta\phi = 0°, 90°, 150°$) in the $\Phi = 0°$ cut. (a) 25 GHz. (b) 26 GHz. (c) 27 GHz. (d) 28 GHz.

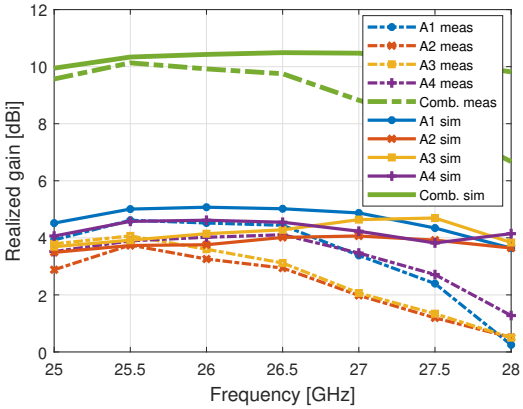

Fig. D.18: Endfire realized gain of each antenna as a function of the frequency. The combined in-phase gain is also represented.

VI Conclusion

This paper presents a new method to decrease the blockage of metal frames to endfire mm-wave arrays with horizontal polarization by using a hard surface inspired design on the frame. The grooves can reduce the diffraction on the edges. The electric field is permitted to propagate through the frame and the energy diffracted is significantly reduced. A vivaldi mm-wave array has been used to test the performance and the results show good agreement with the simulations. The beam-steering scanning range is $\pm 65°$ with a gain higher than 7 dBi.

Acknowledgment

The authors would like to thank Ben Kryer and Kim Olesen for their help with the manufacturing and measurement, respectively.

References

[1] S. Sun, T. S. Rappaport, M. Shafi, P. Tang, J. Zhang, and P. J. Smith, "Propagation models and performance evaluation for 5G millimeter-wave bands," *IEEE Trans. Veh. Technol.*, vol. 67, no. 9, pp. 8422–8439, Sep. 2018.

[2] J. Lota, S. Sun, T. S. Rappaport, and A. Demosthenous, "5G uniform linear arrays with beamforming and spatial multiplexing at 28, 37, 64, and 71 GHz for

outdoor urban communication: A two-level approach," *IEEE Transactions on Vehicular Technology*, vol. 66, no. 11, pp. 9972–9985, Nov 2017.

[3] S. Zhang, X. Chen, and G. F. Pedersen, "Mutual coupling suppression with decoupling ground for massive MIMO antenna arrays," *IEEE Transactions on Vehicular Technology*, vol. 68, no. 8, pp. 7273–7282, Aug 2019.

[4] I. Hwang, B. Ahn, S. Chae, J. Yu, and W. Lee, "Quasi-yagi antenna array with modified folded dipole driver for mmwave 5G cellular devices," *IEEE Antennas Wireless Propag. Lett.*, vol. 18, no. 5, pp. 971–975, May 2019.

[5] M. M. Samadi Taheri, A. Abdipour, S. Zhang, and G. F. Pedersen, "Integrated millimeter-wave wideband end-fire 5G beam steerable array and low-frequency 4G LTE antenna in mobile terminals," *IEEE Trans. Veh. Technol.*, vol. 68, no. 4, pp. 4042–4046, April 2019.

[6] H. Ozpinar, S. Aksimsek, and N. Turker Tokan, "A novel compact, broadband, high gain millimeter-wave antenna for 5G beam steering applications," *Accepted in IEEE Trans. Veh. Technol.*, 2019.

[7] C. Di Paola, S. Zhang, K. Zhao, Y. Zhinong, T. Bolin, and G. F. Pedersen, "Wideband beam-switchable 28 GHz quasi-yagi array for mobile devices," *IEEE Trans. Antennas Propag.*, pp. 1–1, 2019.

[8] Y. Hsu, T. Huang, H. Lin, and Y. Lin, "Dual-polarized quasi yagi–uda antennas with endfire radiation for millimeter-wave MIMO terminals," *IEEE Trans. Antennas Propag.*, vol. 65, no. 12, pp. 6282–6289, Dec 2017.

[9] J. Zhang, K. Zhao, L. Wang, S. Zhang, and G. F. Pedersen, "Dual-polarized phased array with endfire radiation for 5G handset applications," *IEEE Trans. Antennas Propag.*, pp. 1–1, 2019.

[10] R. A. Alhalabi and G. M. Rebeiz, "Differentially-fed millimeter-wave yagi-uda antennas with folded dipole feed," *IEEE Trans. Antennas Propag.*, vol. 58, no. 3, pp. 966–969, March 2010.

[11] C. Di Paola, K. Zhao, S. Zhang, and G. F. Pedersen, "Siw multibeam antenna array at 30 GHz for 5G mobile devices," *IEEE Access*, vol. 7, pp. 73 157–73 164, 2019.

[12] B. Xu, Z. Ying, L. Scialacqua, A. Scannavini, L. J. Foged, T. Bolin, K. Zhao, S. He, and M. Gustafsson, "Radiation performance analysis of 28 GHz antennas integrated in 5G mobile terminal housing," *IEEE Access*, vol. 6, pp. 48 088–48 101, 2018.

[13] Y. Luo, J. Xu, Y. Chen, Y. Sun, B. Xu, S. Xu, and G. Yang, "A zero-mode induced mmwave patch antenna with low-profile, wide-bandwidth and large-angle scanning for 5G mobile terminals," *IEEE Access*, vol. 7, pp. 177 607–177 615, 2019.

[14] R. Rodriguez-Cano, S. Zhang, K. Zhao, and G. F. Pedersen, "Reduction of main beam-blockage in an integrated 5G array with a metal-frame antenna," *IEEE Trans. Antennas Propag.*, vol. 67, no. 5, pp. 3161–3170, May 2019.

[15] J. Kurvinen, H. Kähkönen, A. Lehtovuori, J. Ala-Laurinaho, and V. Viikari, "Co-designed mm-wave and LTE handset antennas," *IEEE Trans. Antennas Propag.*, vol. 67, no. 3, pp. 1545–1553, March 2019.

[16] R. Rodriguez-Cano, S. Zhang, K. Zhao, and G. F. Pedersen, "Mm-wave beam-steerable endfire array embedded in slotted metal-frame LTE antenna," *Accepted in IEEE Trans. Antennas Propag.*, December 2019.

[17] P. Kildal, "Artificially soft and hard surfaces in electromagnetics," *IEEE Trans. Antennas Propag.*, vol. 38, no. 10, pp. 1537–1544, Oct 1990.

[18] P. Kildal, A. A. Kishk, and A. Tengs, "Reduction of forward scattering from cylindrical objects using hard surfaces," *IEEE Trans. Antennas Propag.*, vol. 44, no. 11, pp. 1509–1520, Nov 1996.

[19] "General aspects for User Equipment (UE) Radio Frequency (RF) for NR (Release 15)," 3rd Generation Partnership Project (3GPP), Technical Report (TR) 38.817-1, 03 2019, version 15.3.0.

ISSN (online): 2246-1302
ISBN (online): 978-87-7210-835-3

AALBORG UNIVERSITY PRESS